DETERMINATION OF THE POWER LOSSES ON A TYRE-MOUNTED ORE-GRINDING MILL.

by

L. TYABASHE

1998

Submitted to the University of Cape Town
in partial fulfilment of the requirements for
the degree of Master of Science.

DECLARATION

I, Loyiso Tyabashe, declare that this thesis is essentially my own work and has not been submitted in this or in a similar form for a Degree at any other University.

ABSTRACT

The objective of this study was to determine the power losses occurring on a tyre-mounted ore-grinding mill designed by Dorbyl Heavy Engineering for Mintek. In order to understand the type of losses occurring on this mill it was decided that a scaled model be built and tested. Such a model mill was designed through the dimensional analysis and similitude technique. This technique enables the reduction of the number of variables to be tested by grouping them into a set of dimensionless parameters, and also allows the results obtained by means of experimentation with the scaled models to be related to the full-scale prototypes.

The model mill was constructed in the Mechanical Engineering Workshop at the University of Cape Town. The overall dimensions of the model are 1400 mm long, 1070 mm wide and 892.5 mm high. Its drive-train comprises an electric motor, the wedge and timing belts with the appropriate pulleys, a differential gearset, the tyres, a shell and a disc brake sub-assembly. The tyres used to drive the shell can either be of the pneumatic or solid rubber types. The model mill was designed such that the tyre parameters required in the theoretical solution for power losses, which utilises the Light Vehicle Dynamics Simulation tyre model, could also be measured.

The model mill can be tested in two different modes, namely, the planar and the 3D models. In the planar model the charge centre of mass is exactly midway between the left- and right-hand tyres, and the differential gearset is operated as locked. For the 3D case the centre of mass of the charge is offset longitudinally from that of the shell, resulting in the unequal left- and right-hand tyre normal forces, and the differential gearset is operated as an open differential gearset.

During the planar model analysis the tyre parameters for use in the theoretical study were evaluated for both the pneumatic and solid rubber tyres. It was also established that the pneumatic tyres always generate a higher peak tractive force compared to solid rubber tyres under the same loading conditions. This was shown in the plotted friction coefficient versus longitudinal slip curves where the pneumatic tyres produced higher peak friction coefficients for all the values of the tyre normal force tested. The rolling resistance power losses of the solid rubber tyres were found to be less than those of the pneumatic tyres. Contrary to the solid rubber tyres which showed a steady

decline in the torque capability, the pneumatic tyres showed a very sensitive decrease in the torque capability as the charge mass increased. For a further increase in the values of the charge mass it was observed that the solid rubber tyres could have better torque capabilities than their pneumatic counterparts.

Power losses of the mill drive system depend on the charge mass. Expressed as a percentage of the input power, the %-losses varied from 100% (for zero charge mass) to a minimum of about 10%. This minimum occurs at a tyre longitudinal slip of about 5%. Hence, for a given shell size and mass, the optimum drive tyre size would be such that the tyres operate at about 5% longitudinal slip.

The testing of the 3D model was not as comprehensive as that of the planar model. For the solid rubber tyres the percentage power losses increased with an increasing difference in the left and right hand tyre normal forces. The mill inefficiency also increased with a decreasing overall shell normal force. The exact trends for the pneumatic tyres could not be established. It was recommended that more 3D tests for both tyre types be carried out.

Relationships for evaluating the prototype mill performance during its operation were formulated. The developed relationships are for determining the charge mass, the tyre tractive force, the tyre rolling resistance and the power losses of the mill. In order to determine the above parameters some data signals have to be monitored directly on the mill during operation. Most of the required signals may be measured with relative ease, except for the differential gearset efficiency. This efficiency is required in determining the torque on the drive differential's output shafts. It was recommended that the axle which encloses the two output shafts should be cut at appropriate positions where the strain gauges and slip-rings could be inserted to measure the required torque directly from the shafts. It was also recommended that a thorough theoretical parametric study which could be compared with the operational measurements be carried out for the prototype mill.

ACKNOWLEDGEMENTS

My sincere gratitude goes to Dr. C. Redelinghuys for his dedicated contribution throughout my studies. I would also like to thank Prof. G. Nurick and Assoc. Prof. R. Tait from the University of Cape Town for their respective roles in the development of this project. Thanks to the sponsors of this project, Mintek, for funding my studies. The Mechanical Engineering Workshop personnel, especially Mr. H. Emrich and Mr. H. Tomlinson, was very helpful during the model construction. My special thanks go to Ms. N. Ndonga for the hours she spent with me during the experimental model mill testing phase. Thanks also to both Ms. N. Magazi and Ms. M. Ndonga for their positive contributions. Last, but not least, my family will always be in my heart for they have made it possible for me to carry on even under extreme inconceivable stressful situations.

TABLE OF CONTENTS

LIST OF ILLUSTRATIONS

Tables

NOMENCLATURE

MILLING

A	variable dependent on mill filling.
B	variable dependent on mill filling.
D	mill diameter.
E	variable dependent on the fraction of theoretical critical speed.
F	variable dependent on the fraction of theoretical critical speed.
GP	gross power draw of the mill
k	lumped parameter factor that allows for heat losses due to internal friction and energy consumed, plus the inaccuracies associated with measurements of charge shape and motion.
L_e	effective grinding length.
m_c	charge mass.
m_s	mass of the shell.
N_r	rotational rate of a charge particle inside the mill.
P_{cm}	charge-motion power.
P_c	power draw by the mill with conical ends.
P_d	power supplied to the differential gearset in the mill se-tup.
P_{ds}	power transferred by the tyre to the shell.
P_f	differential gearset power losses.
P_{lds}	total drive power losses occurring on a mill.
P_{ls}	tyre slippage power loss.
P_{net}	net power draw of the mill.
P_{nl}	no-load power.
P_R	power loss due to rolling resistance.
P_{tot}	total power draw by the mill.
r	radial position of a charge particle inside the mill
V_r	tangential velocity of a particle inside the mill.
X_c	offset of charge centre of mass from the longitudinal axis of the shell.
Y_c	longitudinal offset of charge centre of mass from the shell's centre of mass

Greek symbols

ϕ	fraction of theoretical critical speed.
ϕ_c	experimentally determined fraction of theoretical speed at which centrifuging is fully established.
θ_T	toe angle
θ_s	shoulder angle.
$\mathcal{J}$	mill filling.
ρ_c	charge density.

TYRES AND THE DIFFERENTIAL GEARSET

A, B, C, D, E	variables dependent on tyre radii.
A	also area of the of the gear-case (for a differential gearset)
C_H	coefficient of heat dissipation.
C_p	specific heat.
C'_η, F_1, F_2	functions of i_{dp} and μ_P.
C_η	slope of the friction coefficient versus longitudinal slip curve at i=0.
$F_{Ndl,r}$	left or right hand drive tyre normal force.
$F_{Nil,r}$	left or right hand idle tyre normal force.
f_r	rolling resistance coefficient.
F_R	rolling resistance.
f_{surf}	friction adjustment factor for surface type.
$F_{Xl,r}$	left- or right-hand overall tyre tractive force.
F_{X0}	tyre tractive force with the shell unloaded.
F_{Xd}	tyre tractive force required to overcome the mill charge.
h	distance between centre line of differential gearset output shafts and centre line of the motor cantilever.
H_i	input power to the differential gearset.

H_l	power lost inside the differential gearset.
i	longitudinal slip.
i_{dp}	longitudinal slip at peak friction coefficient.
K_b	brake cantilever stiffness.
K_m	motor cantilever stiffness.
$K_{zdl,r}$	left or right hand drive tyre stiffness.
$K_{zil,r}$	left or right hand idle tyre stiffness.
k_{zd}	compressibility of the driver four tyres.
k_{zi}	compressibility of the four idler tyres.
l_{tot}	total length of the brake cantilever.
m_c	charge mass.
m_s	mass of the shell.
m_g	mass of gearset components.
N_f	differential gearset overall speed ratio (>1).
P_d	power supplied to the differential gearset in the mill se-tup.
P_{ds}	power transferred by the tyre to the shell.
P_f	differential gearset power losses.
P_{lds}	total drive power losses occurring on a mill.
P_{ls}	tyre slippage power loss.
Pr	tyre inflation pressure.
P_R	power loss due to rolling resistance.
P_t	power input to the tyre.
$P_0,P_1,P_2,R_0,R_1,S_0,S_1,S_2$	tyre constants for the LVDS tyre model.
Q,R,S,U,V,W	variables dependent on tyre radii, tyre normal forces and drive tyre tractive forces.
$r_{d,i}$	drive or idle tyre loaded radius.
$r_{d,i0}$	unloaded radius of the drive or idle tyre.
$r_{el,r}$	left or right hand tyre effective rolling radius.
r_s	shell radius.
R_1, R_2	successive temperature rises measured during equally spaced time intervals.
t	time.
T_1,T_2,T_3	temperature measured during equally spaced time intervals.

T_a	ambient temperature.
$t_{d,i}$	drive or idle tyre normal force offset from tyre's rolling axis.
t_0	time constant.
$T_{d,i}$	drive or idle load cell tracks.
T_e	final equilibrium temperature.
u	longitudinal velocity of a tyre
V	volume of charge mass.
W	vertical load acting on a tyre.

Greek symbols

ε_{m0}	micro-strain measured from cantilever J whilst disk brakes are disengaged.
ε_{m00}	micro-strain measured from cantilever J whilst the motor is stationary.
$\Delta\varepsilon_b$	difference in strain readings taken from the brake cantilever when disc brakes are engaged and disengaged.
$\Delta F_{Nd,i}$	drive or idle tyre normal force offsets.
η	differential gearset efficiency.
ΔT	measured temperature rise in time t.
ΔT_e	difference between equilibrium and ambient temperatures.
$\phi_{l,r}$	angles made by lines connecting shell's and tyres' longitudinal axes for the driver or idler tyres.
τ	torque.
μ_X	tyre-shell friction coefficient.
μ_P	tyre peak friction coefficient.
μ_s	tyre sliding friction coefficient.
ω	angular velocity.
γ_N	normal force rating coefficient.

CHAPTER 1. INTRODUCTION

Mining engineering has evolved over many centuries world-wide. In all mining operations, the sole purpose of engaging in this activity is to free the valuable minerals embedded in an ore body. It is assumed that the ore body has been mined using explosives and delivered to the processing plant in the "**run of mine**" form, i.e. in the form as it was when mined. As this ore body contains valuable minerals, the main challenge that faces engineers or processing plant operators is the reduction of the material to a size which permits recovery of the minerals, with the most economical usage of power.

The size of the "run of mine" material has got a wide range. In most cases this material is first crushed through the ore crushers. This is usually the first size reduction stage. Crushers operate by applying a sufficient force to exceed the compressive strength of the material to be reduced. During this phase the material size is reduced to about a third of its initial size [1]. However, this size of the material is, usually, still not good enough for setting free the materials being seeked.

The next reduction stage is the milling of the ore body. Some mills, however, do not require the crushing stage. The first continuously fed mill was developed in 1885 by a German engineer, Jenisch [2]. Due to the cost benefits that this mill offered, an estimated amount of about 2000 such mills were in use by 1898. The design of the Jenisch mill plunged the grinding industry, especially the cement industry where the demand for finely ground cement was increasing steadily, into a new direction of further reducing the size of the material bodies. In the past decades mill designers have sought methods to increase the mill efficiency. This challenge has, inter alia, been a way of reducing the power losses during the milling operation. Another major challenge has been the design of mills

which could run for longer periods without any call for repairs, i.e. the extension of trouble free operation.

The motion of a tumbling mill moves the charge that it contains, and in so doing consumes energy. Several mathematical and empirical models have been developed to predict the power losses associated with the mill operation [3]. The existing mathematical models require a full description of the charge motion be made in order to determine the rate at which the energy is consumed. Most of these models agree that power draw of the mill is a function of several interrelated parameters, such as the mill diameter, effective mill grinding length, mill speed, specific gravity of the ore and grinding media, and mill filling. Mill drive mechanisms also contribute to the overall power draw of a mill. This is attributed to the frictional characteristics of the mechanical components.

The introduction of large diameter mills has expanded rapidly and has become a major feature of all recent high throughput plants. These newly designed large mills present some challenges during their operation, with the major one being the selection of the type of the drive system that is required to drive the mill effectively and efficiently. Most mills are driven through the pinion-girth gear mechanisms. The limiting factors in these drive mechanisms is the required pinion tooth face-width due to the fact that the main consideration in the gear design is the determination of a tooth pitch and a face-width for adequate strength and durability, and the resulting problem of maintaining an even load distribution across the tooth face [1]. This has led to the design of twin-pinion drive systems, which also have not solved the gear design problems.

Several South African companies have designed and developed grinding mills for both the local and the international markets. The design of these mills has provided the mill designers with

valuable experience which has been applied to engineer mills eminently suited for local ores and grinding conditions. The trend towards adopting locally designed mills has got an added advantage in that the expenses associated with running a particular milling plant can be predicted more accurately as the labour and other costs are known.

Dorbyl Heavy Engineering, DHE, has developed an ore grinding mill mounted on pneumatic tyres for the Council for Mineral Technology, Mintek. The mill's drive train comprises a motor, a fluid coupling, pulleys and belts, a drive-shaft, the driver and the idler differential gearsets, the driver and the idler wheel sub-assemblies. DHE has introduced the differential gearset and wheel drive tyres in their design so as to avoid the pinion-girth gear size limiting effect highlighted earlier, and also to enable the variation of the mill length during operation. However, this concept has brought along its inherent problems such as the power losses in the differential gearset and the tyres and also the limits on the drive torque due to friction force limits. Figures 1.1 and 1.2 show two different views of this prototype mill.

When operating a differential gearset from stand-still, the oil inside the casing tends to heat up until it reaches a steady-state temperature. Tyres also show a similar effect of heating up when run from stand-still, until a steady-state temperature is reached [4, 5]. The fact that the tyres and oil inside the differential gear-set maintain a steady-state temperature which is higher than the ambient temperature implies that energy is lost as heat. The aim of this project is, thus, to quantify the power losses in the differential gearset and tyres during steady-state operation.

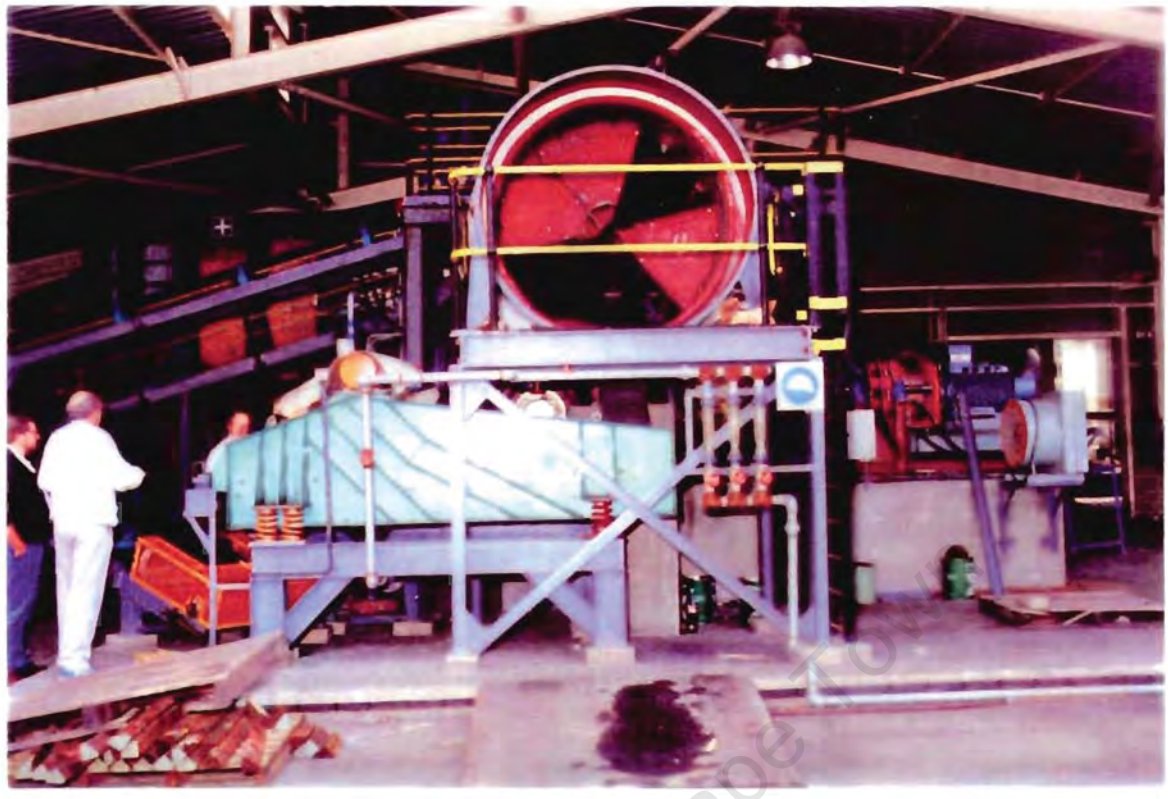

Figure 1.1 The prototype tyre-mounted grinding mill.

Figure 1.2 View of the prototype mill showing the drive train.

Though this project is about an ore-grinding mill power analysis, the main focus is on the mill drive-train power losses. A general introduction on the operation of tumbling mills is given in chapter 2. This chapter also discusses the different mill types that dominate the milling industry. A theoretical analysis for predicting the grinding power losses on mills is also presented in this chapter. Chapter 3 discusses the general behaviour of some important parameters associated with pneumatic tyres. In 1995 the mill was analysed in three different projects. These studies are reviewed in chapter 4. Chapter 5 discusses the experimental model mill. Both the model mill concept and the mathematical representations of mill models are discussed in this chapter.

Calibration of several measuring devices on the experimental model mill is presented in chapter 6. Experimentation with the model mill, and analysis of results are presented in chapters 7 and 8. Chapter 9 presents a guideline for calibrating the prototype. This guideline will enable the mill operators to determine the power losses occurring on the prototype by taking appropriate measurements during the mill operation. Concluding remarks follow in chapter 10. Chapter 11 discusses proposals for further courses of action.

CHAPTER 2. TUMBLING MILLS

The present investigation is concerned with the performance of a tumbling mill. A general overview on such mills would provide a broader understanding with regard to their operation. Some studies pertaining to quantification of the losses associated with the ore grinding mills are discussed in this chapter.

2.1 GENERAL OPERATION OF TUMBLING MILLS

Comminution, by definition, relates to all stages of size reduction of an ore-body to a form suitable for mineral separation. Thus, grinding belongs to this comminution family. The general term tumbling mill includes rod, ball, pebble, autogenous and tube mills. A tumbling mill is of a cylindrical or cylindro-conical shape, and rotates about its horizontal axis.

The transfer of energy from the mill shell to the charge is influenced by frictional forces acting on the concentric layers of the charge [3]. For grinding to be effected the mill must be operated below the critical speed. The critical speed of a tumbling mill is defined as that speed which causes the charge to stick to the shell during the rotation of the mill, i.e. the mill charge does not separate and grind at this speed. Generally, all tumbling mills show an increasing throughput, an increasing power consumption and an increasing wear up to a maximum as the speed rises, and then a reduction as the critical speed is approached [1].

During the tumbling action the mill shell speed is selected to ensure that the cascading charge impacts on the "toe" of the charge rather than on the mill-shell itself. This results in reduced wear of the mill liners. Figure 2.1 presents a diagram of the mill showing the "shoulder" and the "toe" of the charge. The breakage of the ore is accomplished by compression. Compression may be due to a rapid impact resulting from fall or roll of the ore. When subjected to this compression a rock deforms. If the compressive force exceeds a certain critical value, an incipient cracks develops in the most fragile zones of weakness. When the first crack-tip forms the compressive stresses immediately surrounding it flow to it, and this concentration of forces extends the crack and, finally, splits the rock [6].

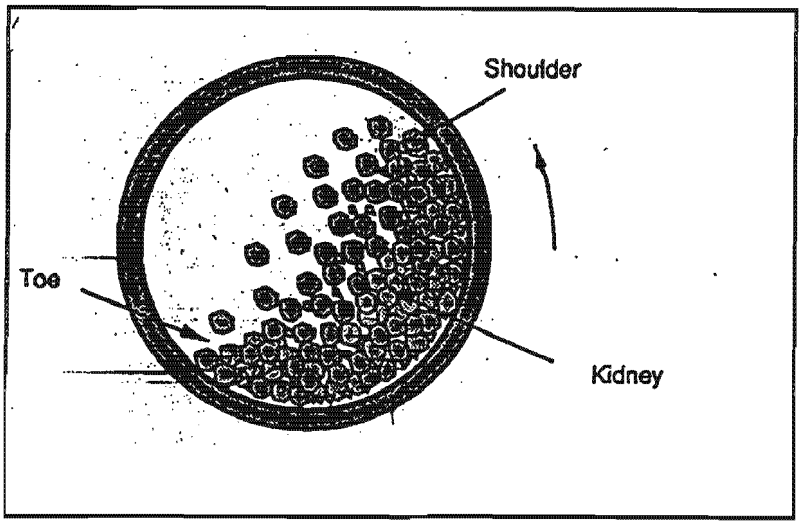

Figure 2.1 Diagram showing the "shoulder" and the "toe" of the mill charge.

The nature of brittle ores is such that breaking them consists, essentially, of the work input required to compress them to the point at which the first crack-tip forms. Thus, no appreciable additional energy input beyond that required for deformation is required since the stress energy already imparted to the rock flows to the crack-tip and extends it to breakage .

Ore can be ground dry or in a slurry. Dry grinding nominally refers to less than 1% moisture by weight. The capital costs for wet grinding are, generally, lower than those for dry grinding. For the case when thickening and filtering of the wet-ground product are required, dry grinding may have an advantage over wet grinding, in terms of capital costs [6].

The grinding circuit may either be open or closed. With the open-circuit grinding the mill discharge passes directly to the next processing phase without being screened or classified, and no fraction is returned to the mill. However, in the closed grinding circuit the mill discharge is removed using either a screen or a classifier, with the oversize material being returned to the mill

for additional size reduction. The oversize material that is returned to the mill for further size reduction is referred to as the *circulating load.*

Open circuit grinding requires more power than closed circuit grinding for products containing similar amounts of top-size material. This follows from the fact that the less the amount of oversize material allowed in the product, the longer the ore must remain in the mill for the case of open-circuit grinding. The two major aims of using closed-circuit grinding are to control the amount of top-size desired in the output, and to limit the production of excess fines.

Sections 2.2 through 2.4 discuss the ball mills, the rod mills and autogenous mills, respectively. The other grinding machines in operation are pebble mills, roller mills, fluid energy mills, impact machines, attrition machines and vibrating ball mills. These machines are, however, used in very specialised grinding operations and will not be discussed further in this document.

2.2 BALL MILLS [6]

Modern ball mills use steel or iron *spherical balls* to grind ores to the specified product size. Ball mills are adopted to grind ores, especially the more abrasive ones, to finer sizes than can be produced economically in the other size reduction machines such as roll crushers and impactors. The bulk volume of these steel or iron balls is approximately 35 % of the total shell volume.

The power drawn by a mill is function of parameters such as the slump factor (ball diameter-mill diameter ratio), the ball diameter-mill length ratio, the liners, the mill speed, the bulk density of

ball charge, the amount of charge, the feed rate and ore grindability. A cutaway view of a Hardinge Tricone ball-mill is shown Figure 2.2.

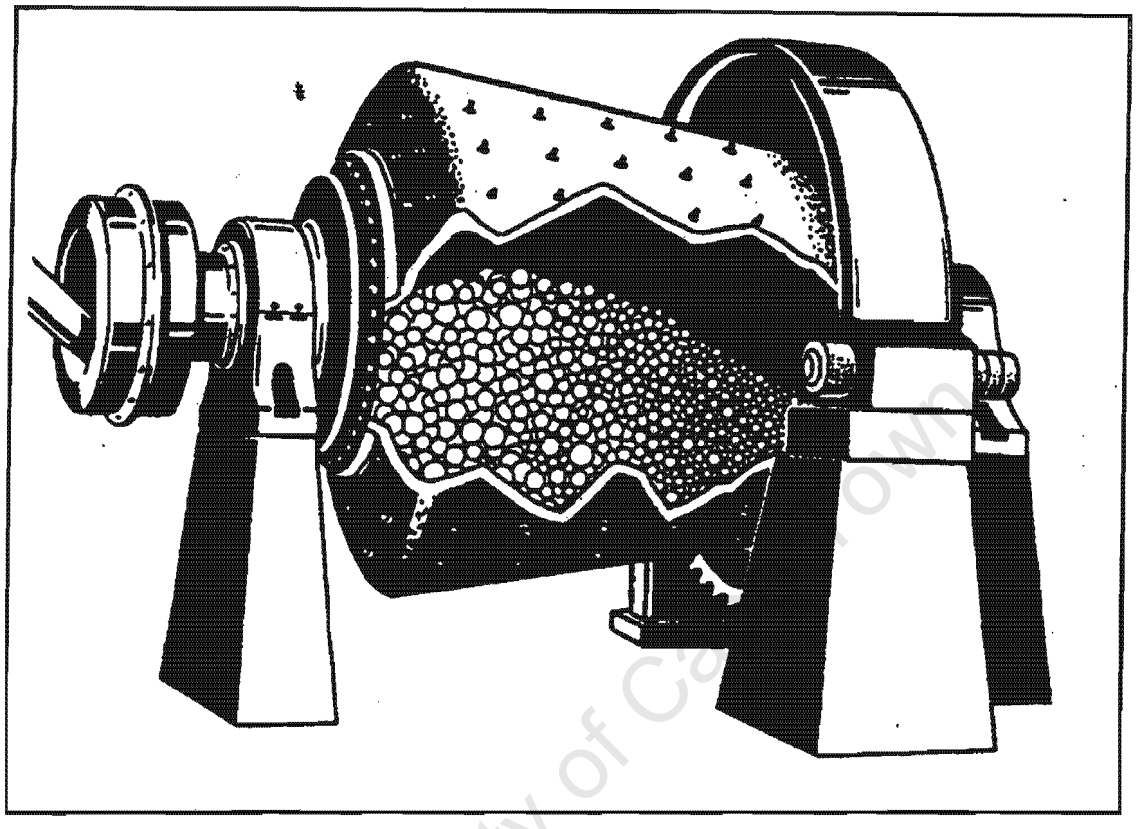

Figure 2.2 A cutaway view of a Hardinge Tricone ball-mill.

2.3 ROD MILLS [6]

Rod-mills are horizontal, rotating, tumbling mills in which *steel rods*, that are shorter than the length of the grinding chamber, are used as the grinding media. A cutaway view of a rod-mill is shown in Figure 2.3. Rod-mills were used because of their ability, in open circuit grinding, to produce a uniformly sized product, to give a greater continuous availability, and to give lower maintenance costs.

These mills are predominantly used in grinding gravel or aggregates to the size required for making the concrete sand, in preparing the feed for ball or pebble mills, in preparing the coarse agitator feed for leaching operations, and for primary grinding circuits particularly in industrial mineral applications. For rod milling operations, wet grinding is the most frequently used. However, dry grinding is used in a few special cases.

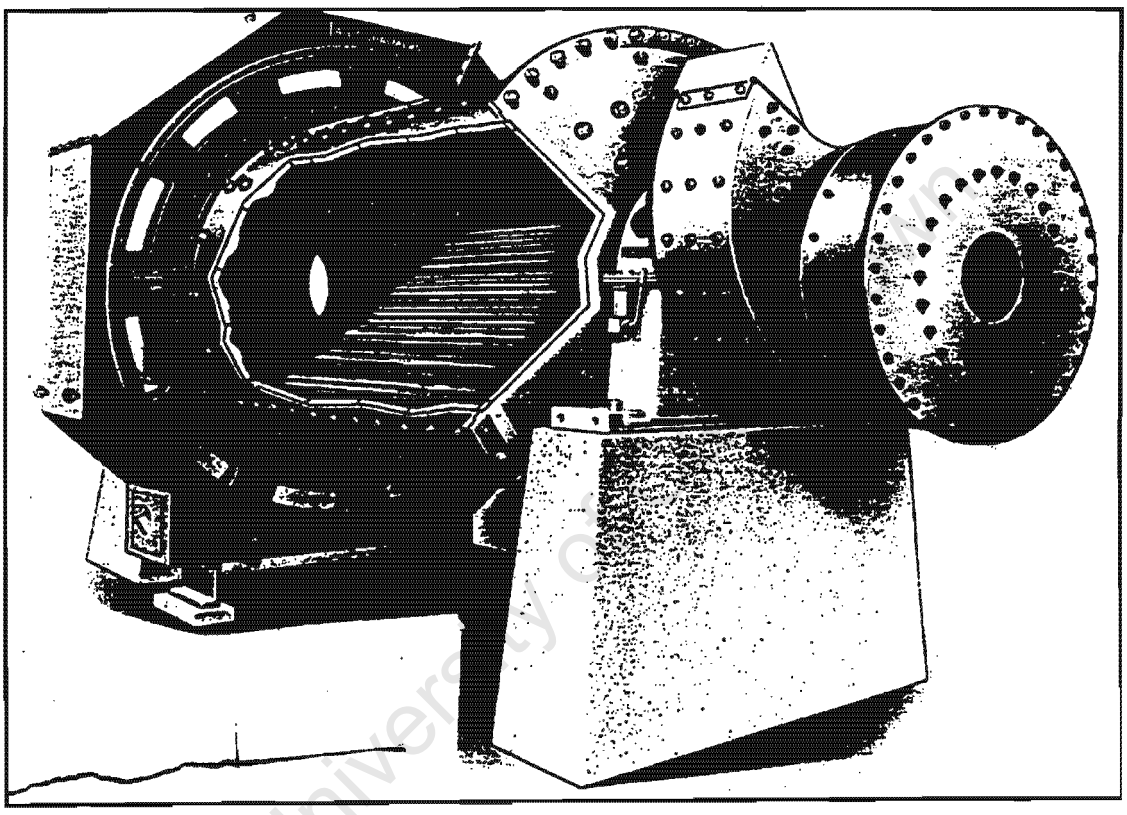

Figure 2.3 A cutaway view of a rod mill.

The rod mill feed is normally produced in the cone crushers, or in impactors or hammer mills in case of wet, sticky and non-abrasive materials. There is a wide variation in the size of the rod mill feed without any best specific size for both open- and closed-circuit grinding. The most satisfactory feed to a rod mill is consistent in particle size distribution with a top size that will not

cause spreading of the rods to the extent that it causes excessive wear and tapering at the feed end of the rods, or blocking of the feed trunion so as to restrict the flow of the feed into the mill.

The rod length and diameter play a very crucial role in determining the mill capacity. The rated capacity is a direct function of the power required to grind the feed to a desired product size and the power drawn by the mill. Generally, these mills are most efficient just before they become plugged. This is due to the fact that when the rod mill capacity reaches a point where it pushes the rods apart, the product size control is lost and the overall performance becomes poor. Under these conditions efficiency is reduced.

2.4 AUTOGENOUS MILLS [6]

Autogenous grinding is defined as grinding of the ore by itself rather than by special metallic or non-metallic grinding bodies distinct from the ore being ground. This type of grinding has been in use for ages in the mineral processing industry. Autogenous grinding is also called ***rock-on-rock*** grinding. These mills receive broken ore that has been passed through a primary crusher, or ore directly as mined.

Autogenous grinding has two main advantages. The metal wear is reduced drastically since there are no metal to metal impacts. The second advantage is that the number of grinding and crushing stages is also reduced compared to the conventional size-reduction operations. When combined together, these two advantages lead to large savings in capital and operating costs. However, autogenous milling is practical for only a limited number of ore types.

The first requirement in autogenous grinding is the continuous availability of large pieces of hard rock to serve as the effective grinding media. Another requirement is that it should be easier to break the ore in finer sizes than in the coarse ones, i.e. the finer particles should be broken easily by the coarse ones. There is a critical particle size in autogenous grinding. This is the size which is too small to serve as an effective grinding medium, and yet is too large to be readily broken by the larger particles. Ores of high specific gravity, such as the iron ores, grind well autogenously. However, before a decision is made in favour of autogenous grinding, extensive pilot-plant process tests are advisable.

The two major requirements highlighted in the preceding paragraph usually compel mill designers to modify autogenous mills by adding large diameter steel balls to the charge, making them semi-autogenous mills. Semi-autogenous grinding refers to those milling operations where spherical steel balls or other grinding media different from the ore being ground are used in conjunction with the ore itself for grinding. The bulk volume of the steel balls is usually less than 12 % of the mill shell volume.

Semi-autogenous mills with a sufficient ball charge have no trouble with the material of critical size. This conversion from autogenous to semi-autogenous mills sometimes presents serious problems. Semi-autogenous mills have a disadvantage of the higher cost of balls used and an increased liner wear and breakage. While semi-autogenous grinding relies upon the quantity of the steel balls as the grinding media supplement, the presence or absence of competent natural rock media affects the grinding performance considerably. Nonetheless, the modern trend is towards adopting semi-autogenous milling.

2.5 GRINDING POWER PREDICTION

Morrell [7] developed two models for predicting grinding power draw of tumbling mills. These are the continuum and the empirical models, henceforth referred to as the "C" and "E" models, respectively. Both models are equally applicable to ball, semi-autogenous and autogenous mills. Other power draw models based on the motion of the charge, the mill-shell liners and the grinding media shape have also been developed by other authors. One should note that the **power losses due to mechanical driving components** in Morrell's models have been **estimated** by inserting some parameters in the power equations presented below.

2.5.1 THE C-MODEL[1]

In this model the charge is treated as a continuum. The rotation of a tumbling mill moves the charge longitudinally, and in so doing consumes energy. Thus, the key to determining the rate at which the energy is being consumed (power draw) lies in being able to describe the motion of the charge. The approach adopted is to estimate the rate at which the mill shell provides the potential and kinetic energies to the charge, i.e. power draw due to charge motion, from a description of the shape and motion of the charge. The following relationship describes the gross power of the mill,

$$GP = P_{nl} + k \cdot P_{cm} \tag{2.1}$$

where GP is the gross power or power input to the motor.

[1] Sections 2.5.1 and 2.5.2 are based on the publication by S. Morrell, "Power draw of wet tumbling mills and its relationship to charge dynamics". Section 2.5.1 is based on Part I of this document whilst 2.5.2 is based on Part II.

P_{nl} is the no-load power or power input to the motor when the mill is empty.

P_{cm} is charge-motion power or power associated with charge motion.

k is the lumped parameter that allows for heat losses due to internal friction and energy consumed plus inaccuracies associated with measurements of charge shape and motion.

The no-load power *estimates* the drive-train and motor inefficiencies, and is modelled using an empirical relationship that is based on the data from industrial mills. The parameter k was obtained by comparing the no-load and the charge motion power with the gross power draws which were recorded during detailed surveys carried out on the full-scale mills. The power associated with the charge motion is estimated by employing a mathematical description of the shape and position of the charge, and the velocities of particles within it.

Photographs of the mill charge show that during the tumbling action the charge inside the mill forms a kidney shape, see Figure 2.4. Figures 2.5(a) and 2.5(b) approximate the charge shapes in both grate- and overflow-discharge mills, respectively. The only visible difference between the grate- and overflow-discharge configurations is the presence of a slurry pool in the latter. Toe and shoulder angles, θ_T and θ_S, in radians, are modelled as shown in equations (2.2) and (2.3), respectively.

$$\theta_T = A \cdot [1 - e^{-B(\phi_c - \phi)}] + \frac{\pi}{2} \qquad (2.2)$$

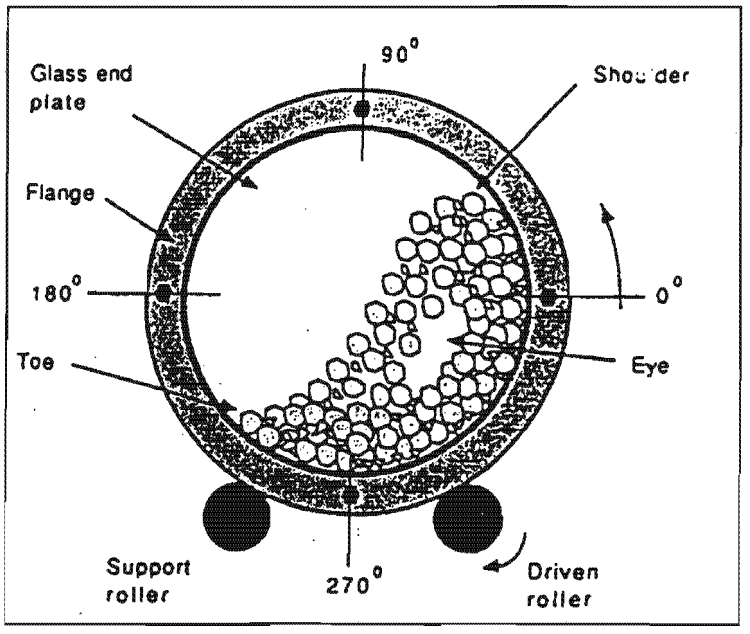

Figure 2.4 Charge inside the mill.

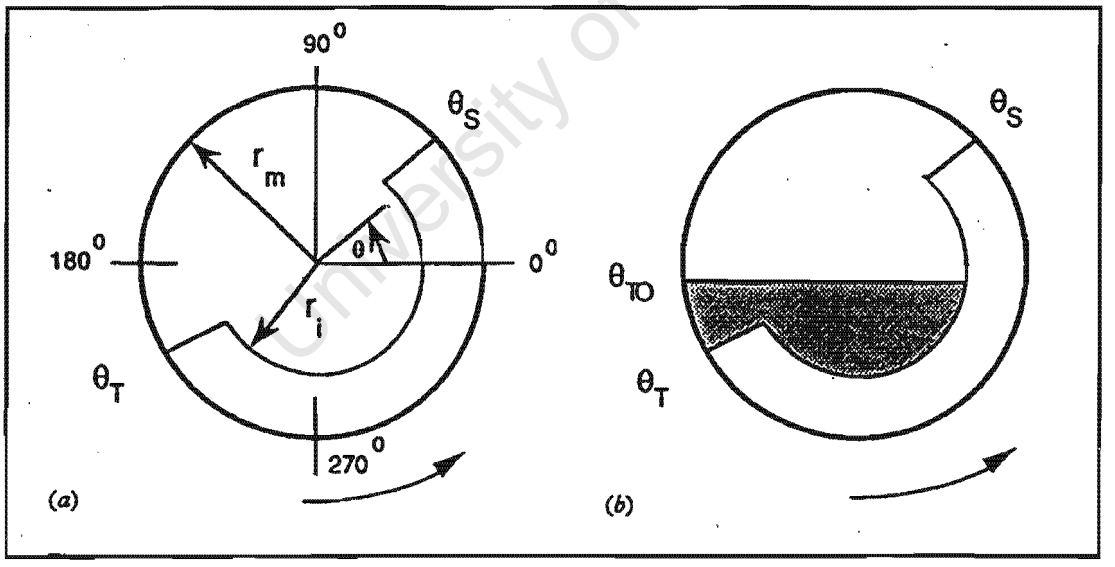

Figure 2.5 Approximate shapes of charge in both grate- and overflow-discharge mills, respectively.

$$\theta_S = \frac{\pi}{2} - (\theta_T - \frac{\pi}{2}) \cdot (E + F \cdot \Im_t) \tag{2.3}$$

where

A and B are functions of mill filling, $\Im_t$.

ϕ is the fraction of the theoretical critical speed at which the mill is run.

ϕ_c is the experimentally determined fraction of the theoretical critical speed at which centrifuging is fully established.

E and F are functions of ϕ.

The tangential velocity, V_r, of a charge particle inside the mill at a radial position, r, is expressed in terms of a rotational rate, N_r, by the following equation,

$$N_r = \frac{V_r}{2 \cdot \pi \cdot r} \tag{2.4}$$

With reference to Figure 2.6 , consider an element within the surface ABCD of length L and width dr. The area and mass flow-rate in this element are given by Ldr and $V_r \rho_c Ldr$, respectively. The parameter ρ_c is defined as the density of particles in this surface. The sum of the rates at which the potential and kinetic energies are generated for all particles passing through the surface ABCD, P_{tot}, is given by,

$$P_{tot} = \int_{r_i}^{r_m} [V_r \cdot L \cdot \rho_c \cdot r \cdot g \cdot (\sin\theta_S - \sin\theta_T) + \frac{L \cdot \rho_c \cdot V_r^3}{2}] \cdot dr \tag{2.5}$$

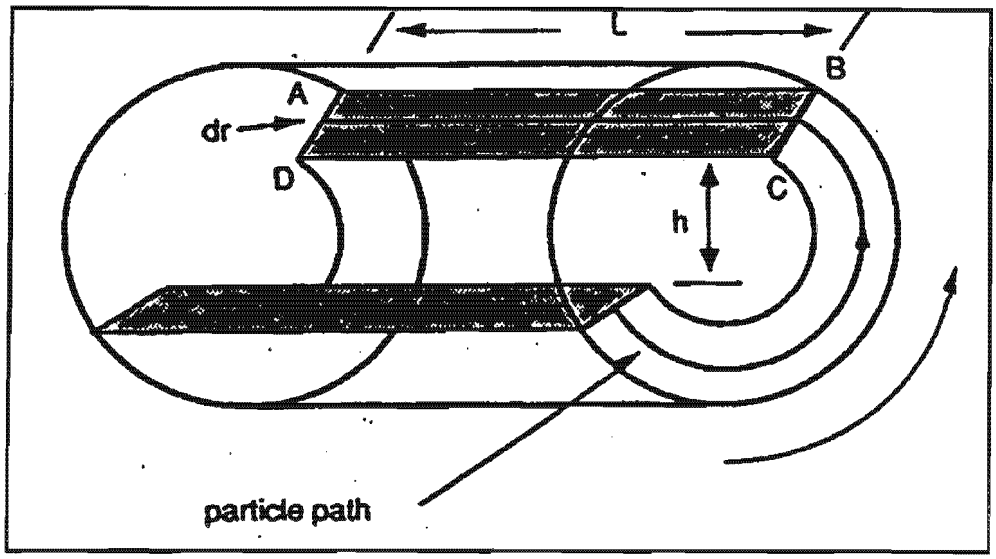

Figure 2.6 Schematic diagram of the mill charge used for C-model

Therefore,

$$P_{tot} = \frac{\pi \cdot g \cdot L \cdot N_m \cdot r_m}{3 \cdot (r_m - z \cdot r_i)} \cdot [2r_m^3 - 3z \cdot r_m^2 \cdot r_i +$$

$$r_i^3 \cdot (3z - 2)] \cdot [\rho_c \cdot (\sin\theta_S - \sin\theta_T) + \rho_p \cdot (\sin\theta_T - \sin\theta_{T0})] + \qquad (2.6)$$

$$L \cdot \rho_c \cdot [\frac{N_m \cdot r_m \cdot \pi}{r_m - z \cdot r_i}]^3 \cdot [(r_m - z \cdot r_i)^4 - r_i^4 \cdot (z - 1)^4]$$

where

θ_{T0} is the angle of slurry pool (for grate discharge mill $\theta_{T0} = \theta_T$)

Equation (2.6) gives a relation for predicting the power drawn by a mill. For a mill with conical ends the following equation for power draw was developed,

$$P_c = \frac{\pi \cdot g \cdot L_d \cdot N_m}{3 \cdot (r_m - r_i)} \cdot [r_m^4 - 4 \cdot r_m \cdot r_i^3 + 3 \cdot r_i] \cdot [\rho_c \cdot (\sin\theta_S - \sin\theta_T) + \rho_p \cdot (\sin\theta_T - \sin\theta_{T0})] + \frac{2 \cdot \pi^3 \cdot N_m^3 \cdot L_d \cdot \rho_c}{5 \cdot (r_m - r_i)} \cdot (r_m^5 - 5r \cdot r_i^4 + 4 \cdot r_i^5) \quad (2.7)$$

The above relationships were used, and results in the 95% confidence interval were obtained.

2.5.2 THE E-MODEL

This is a simpler empirical model based on the C-model. As its name implies this model relies on some experimentally evaluated mill parameters. These parameters are the mill diameter (inside liners), the length (inside liners), the rotational speed, ball filling, the total filling (balls plus charge), the discharge mechanism (grate or overflow), and the specific gravity of the ore. From the analysis of the factors affecting the power draw that had been considered, the following were listed as having a marked influence : mill diameter, D; effective grinding length, L_e; speed (fraction of critical), ϕ; charge density, ρ_c; and mill filling, J_t.

The gross power draw of a mill,GP, is given by the following relationship,

$$GP = P_{nl} + P_{net} \tag{2.8}$$

where P_{nl} is the no-load power.

P_{net} is the net power draw to the mill.

The no-load power of the E-model was obtained through calibration. The resulting relationship is as follows,

$$P_{nl} = 1.68 \cdot D^{2.05} \cdot [\phi \cdot (0.667 \cdot L_d + L)] \tag{2.9}$$

From the analysis of the C-model equations the underlying relationships between the variables with a marked influence on the mill power draw and power draw can be expressed in the following form,

$$P_{net} = k \cdot D^{2.5} \cdot L_e \cdot \rho_c \cdot \alpha \cdot \delta \tag{2.10}$$

The rotational speed and mill filling are related in a complex form to the power draw, owing to their influence on positions of the toe and the shoulder of the charge. The parameters ϕ, α, δ, L_e and ρ_c were then obtained empirically. In addition, the effective grinding length of the mill was defined to take into account the effect of any cone ends.

With the above relations one can determine the gross power to the mill by obtaining both the net and the no-load power draws. The performance of this model was found to be only marginally less

accurate than that of the C-model. It was then concluded by Morrell that these two models, together with the detailed data that was used to validate them, overcame the shortcomings of the previous attempts to predict the power draw of the mills accurately.

CHAPTER 3. WHEEL-TYPE FRICTION DRIVE SYSTEMS

This chapter deals with the general behaviour of the tyres. Since pneumatic tyres are mainly used in automotive designs most of the discussions will lean on tyres in automotive applications. As the mill shell rests on and is driven by pneumatic tyres, knowledge of the general behaviour of pneumatic tyres is necessary for understanding the mill drive-train performance under the different loading conditions.

3.1 PNEUMATIC TYRES IN AUTOMOTIVE APPLICATIONS

From its inception the pneumatic tyre has evolved, firstly, to satisfy the needs of bicycle comfort and , later, to meet the more stringent requirements of the automotive and aircraft industries [8]. People tend to think of a pneumatic tyre as a doughnut-shaped piece of black rubber with air in it. However, a tyre is more complicated than that. Modern tyres consist of at least twenty-five structural parts containing as many as ten different rubber compounds [9]. Figure 3.1 shows some of these components.

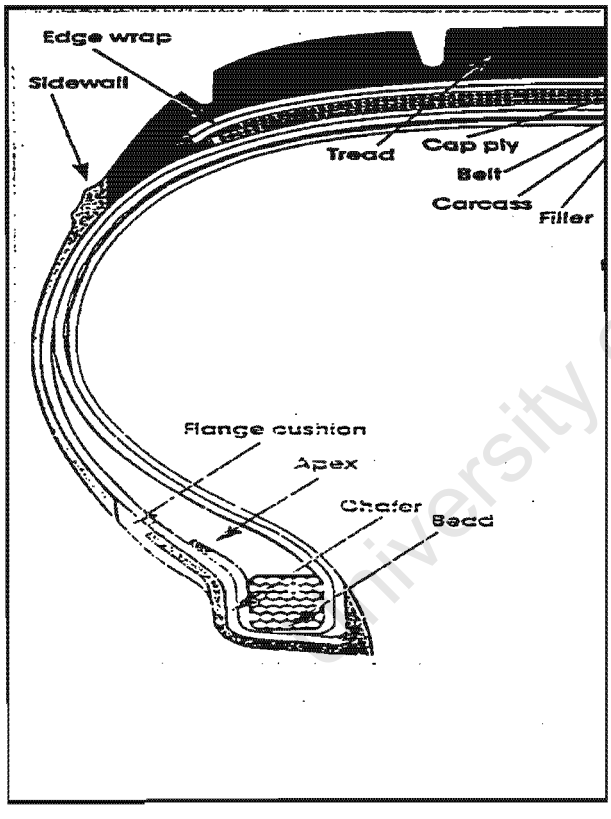

Figure 3.1 Structural parts that make up a modern tyre.

Tyres are designed for specific purposes, hence there are specially designed tyres for the different classes of vehicles, e.g. light trucks, trailers, caravans and minibuses [8]. The qualities a good tyre should have usually oppose each other. Thus, no tyre can have all such good qualities, e.g. a hard tyre cannot grip like a soft tyre, the tread type that prevents aquaplaning is noisy on dry roads and has an increased rolling resistance [10]. Tyre designers are left with no option but to reach a compromise on several of these qualities during the tyre design process.

In ordinary road vehicles all the primary control and disturbance forces applied to the vehicle are generated in the tyre-road contact patch. This, however, excludes the aerodynamic forces which can normally be considered to be of secondary importance. As the different types of tyres generate different tyre-road interaction forces, the choice of a tyre type for a particular purpose is thus crucial. For automotive designs the tyre mainly performs the following functions [4] :

- It supports the vertical load.
- It develops the longitudinal forces, be it accelerating or retarding forces, or forces overcoming resistance to motion.
- It develops the lateral forces for cornering.

In the case of a tyre-mounted mill only the first and second functions are applicable.

It is accepted that a tyre will wear, but it is the rate of wear that concerns both the manufacturers and users. This is due to the fact that the friction between the tyre and road is unavoidable as it is the prime mechanism for providing relative motion between the tyre and the road. The force generation characteristics and the other inherent tyre losses are presented in the subsequent subsections.

3.2 FORCE GENERATION CHARACTERISTICS OF PNEUMATIC TYRES [4]

When a tyre comes to contact with the road surface the normal and longitudinal forces on a tyre do not act at a point, they act over the whole *contact patch.* A contact patch is defined as an area of a tyre in contact with the road surface. When stationary, the pressure distribution in the contact patch is symmetric about the tyre spin axis. However, when the tyre moves, the pressure distribution varies along the road surface plane. The pressure distribution is generally not symmetric about the lateral axis to the tyre motion when a tyre rolls, but tends to be higher in the forward region of the contact patch. This phenomenon is shown in Figure 3.2.

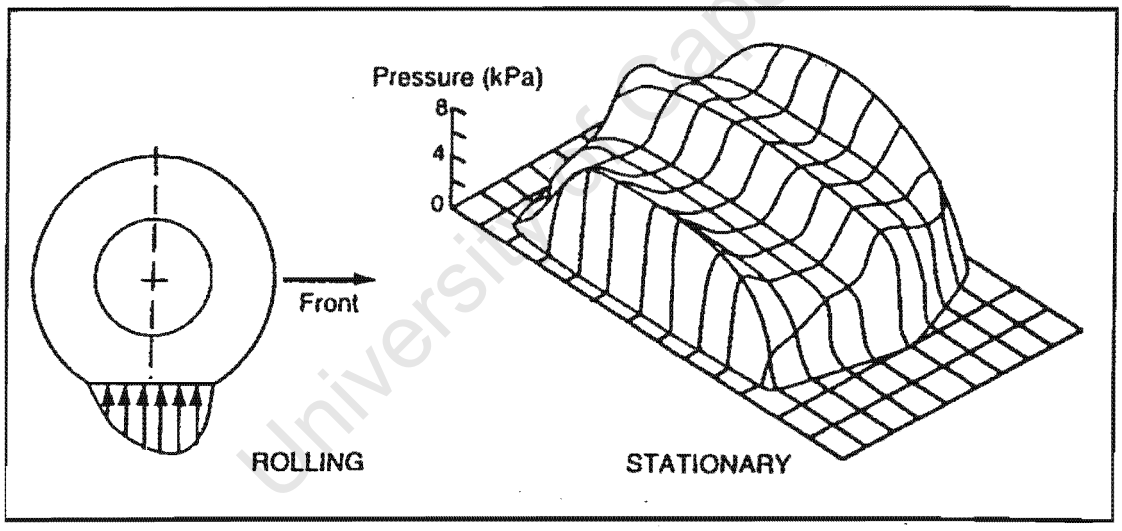

Figure 3.2. Pressure distribution under a rolling tyre.

Due to its visco-elasticity, the deformation in the tyre's leading edge of the contact patch causes the centroid of the vertical pressure to be shifted forward. As the centroid of the vertical force does not pass through the spin axis of the tyre, this results in the rolling resistance. The rolling

resistance is discussed in section 3.3. The shearing action between the road aggregate and the tyre rubber is the mechanism for generating tyre forces. Each element of the tyre tread passing through the contact patch exerts a shear stress. Integrated over the contact area this gives the tractive and/or lateral forces developed by the tyre.

When tread elements first enter the contact patch they must bend in order to develop a tractive force. Bending of these elements can only occur if the wheel is rotating faster than the circumference of the treads. As a tread element proceeds through the contact patch, its deflection builds up concurrently with the vertical load. This tread element develops an even more frictional force. Approaching the rear of the contact patch the load diminishes and there comes a point where the element begins to slip noticeably on the surface. The consequence is the production of slip in the contact patch. The concept of slip can, thus, be easily understood as follows : " no tyre can transmit torque without its treads in the contact patch showing a shearing or bending effect." This is analogous to the analysis of static structures where "no structure can sustain a force without deformation."

Slip in the longitudinal direction is defined non-dimensionally as follows,

$$i(\%) = \left(\frac{u}{r_e \cdot \omega} - 1\right) \cdot 100 \qquad (3.1)$$

where u is the longitudinal velocity of the tyre.

r_e is the tyre's effective rolling radius.

ω is the tyre's angular velocity.

Note that $i > 0$ for braking.

Typical slip curves are shown in Figure 3.3. This diagram shows an almost linear relationship between the friction force and the slip. This is then followed by a reduction in slope of the curve until a maximum force occurs at approximately 20 % of slip. This curve ultimately falls to a lower equilibrium level at which the tyre begins to slide.

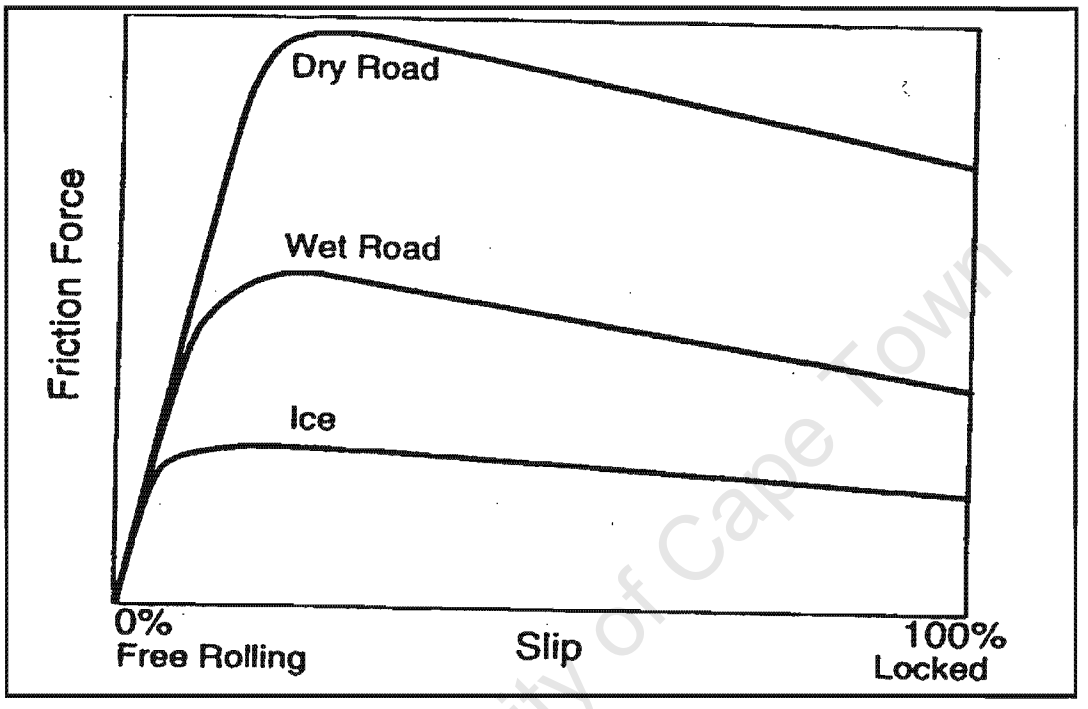

Figure 3.3. Typical slip curves.

The tyre friction coefficient depends on a number of variables, namely, the vertical load, the inflation pressure, the surface roughness and the speed. Increasing the vertical load reduces the peak friction coefficient under both dry and wet conditions. Tyre manufacturers supply tyres with recommended inflation pressures for different situations. Operating a tyre above or below this recommended value usually leads to rapid wear or failure of the tyre.

A tyre alone does not have a friction coefficient. It is the tyre-road pair that results in a particular friction coefficient. Thus, the surface on which the tyre runs has got a direct influence on the amount of friction coefficient that can be produced by a particular tyre. On dry road surfaces the friction coefficient decreases with an increasing speed. However, on wet surfaces the tyre's frictional coefficient shows a more drastic sensitivity to an increase in speed. This is due to the difficulty experienced by the tyre in displacing the water in the contact patch at higher speeds. An extreme situation which happens in wet weather conditions is known as *aqua-planing*. This phenomenon occurs when the tyre speed and water film are sufficient to lift the tyre off the road, i.e. the tractive or braking forces are generated through this water film which is in-between the tyre and the road surface.

3.3 ROLLING RESISTANCE

One of the major resistance forces on the level ground is the rolling resistance of the tyres. As the name implies, it is a resistance to motion. The rolling resistance force always opposes the tyre motion. Contrary to the aerodynamic drag, which strongly depends on the vehicle speed, the rolling resistance is mildly affected by the speed. The aerodynamic drag becomes equal to the rolling resistance as speeds of about 80 - 100 km/h are approached [4]. However, for off-highway, level ground operation, the rolling resistance is the only significant retardation force.

Rolling resistance is present from the instant the tyre begins to run. Thus, for any forward motion in the level ground to be effected, the tractive force must overcome the resultant of resisting forces. These forces include rolling resistance. Rolling resistance, F_R, is defined mathematically as follows:

$$F_R = f_r \cdot W \tag{3.2}$$

where

f_r is the non-dimensional coefficient which expresses the effects of complicated and interdependent physical properties of the tyre and road surface.

W is the vertical load that acts on a tyre.

The value of f_r proves quite useful as the establishment of standardised conditions for measurement of the tyre-road properties proves extremely difficult, if not impossible. In a nutshell, the engineering effort is towards construction of very low rolling resistance tyres. This will in turn yield tyres with higher speed ratings and reduced fuel consumption. Tyre designers are faced with several factors during the whole tyre design process. The stringent requirements that the tyre must meet are that it must have good grip in both wet and dry conditions, and it must also have good wear characteristics. With these requirements the tyre must not be costly [11].

3.4 TYRE MODELS

There exists a number of indoor and outdoor devices used to test tyres. These tests are usually carried out so as to obtain the traction, cornering and braking performances of tyres. Data acquisition in both instances is through sophisticated digital micro-computers. Most of the empirical data that have been obtained and analysed through these tests have been compared with the different theoretical tyre models that have been developed world-wide.

Pacejka [12] has developed a model that can determine the side force, the self-aligning torque and the brake force acting on a tyre. This model, like other models, requires some tyre empirical information before it can be utilised with success. Another model is the Light Vehicle Dynamics Simulation (LVDS) tyre model [13]. In this model the tyre forces and moments generated are non-linear functions of the actual normal load, longitudinal slip, slip angle, camber angle, and tyre-roadway frictional characteristics.

The LVDS model utilises a third order polynomial to approximate the coefficient of friction, μ_X, as a function of the longitudinal slip, i_d. In the friction-slip curve shown in Figure 3.4 the following approximation to the curve is made,

$$\mu_X = F_1 \cdot abs(i_d^3) + F_2 \cdot (i_d^2) + C'_\eta \cdot abs(i_d) \tag{3.3}$$

where

C_η is the slope of curve at i_d=0

$$F_1 = \frac{C'_\eta \cdot i_{dp} - 2 \cdot \mu_p}{i_{dp}^3} \tag{3.4}$$

$$F_2 = \frac{3 \cdot \mu_p - 2 \cdot C'_\eta \cdot i_{dp}}{i_{dp}^2} \tag{3.5}$$

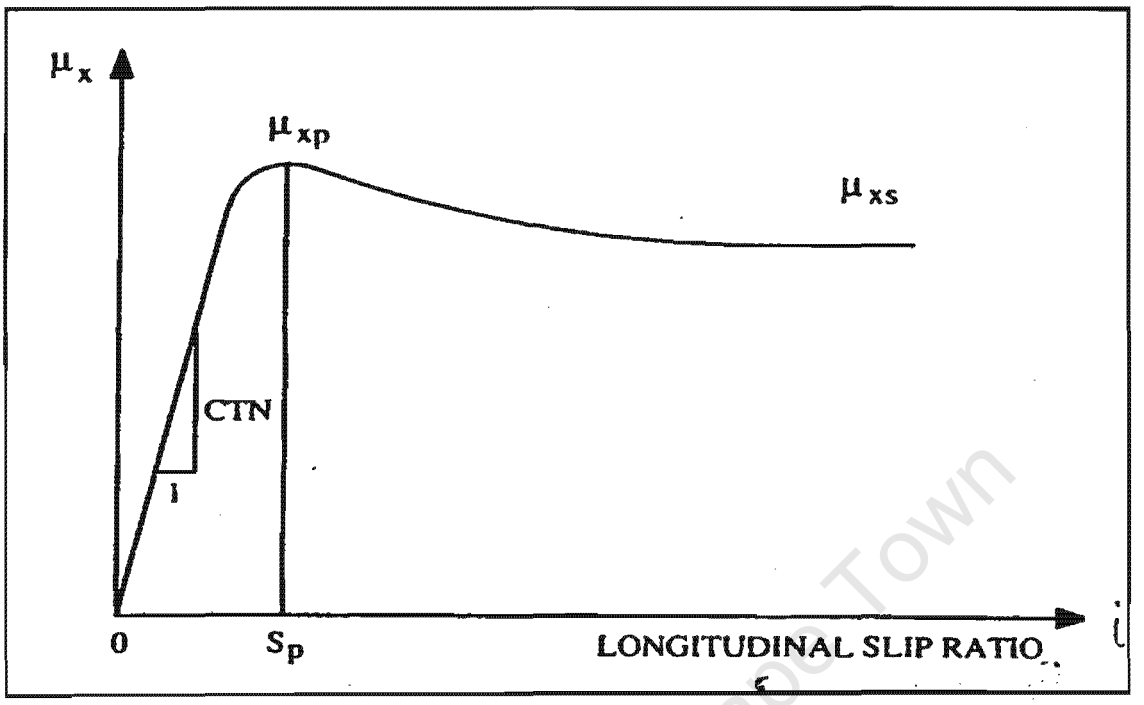

Figure 3.4 Friction coefficient versus slip coefficient for use in the LVDS model.

$$\mu_p = [P_0 + P_1 \cdot F_{Nd} + P_2 \cdot F_{Nd}^2] \cdot f_{surf} \qquad (3.6)$$

$$i_{dp} = R_0 + R_1 \cdot F_{Nd} \qquad (3.7)$$

$$\mu_s = [S_0 + S_1 \cdot F_{Nd} + S_2 \cdot F_{Nd}^2] \cdot f_{surf} \qquad (3.8)$$

$$C'_\eta = C_\eta \cdot f_{surf} \qquad (3.9)$$

$$\mu_X = \frac{F_X}{F_{Nd}} \tag{3.10}$$

f_{surf} is the friction adjustment factor for the surface type

The parameters P_o , P_1 , P_2 , R_o, R_1, S_o, S_1 and S_2 are all empirical constants. The data input to the LDVS model is designed to automatically accept the Calspan tyre coefficients. However, if this Calspan data is unavailable, the required tyre characteristics must be found through experimentation.

CHAPTER 4. PREVIOUS STUDIES OF THE TYRE-MOUNTED MILL CONDUCTED AT THE UNIVERSITY OF CAPE TOWN

The first document which contains a thorough analysis of the Dorbyl tyre-mounted mill was compiled for Mintek in January 1995. In this report a theoretical basis for the in-operation measurement of the drive power losses on this tyre mounted ore grinding mill is presented. It takes into cognisance the presence of a differential gearset and both the idler and driver tyres. This analysis is pertinent to this project as most articles published on mill performance deal specifically with the mill grinding power without giving proper attention to the losses in the drive system. A review of this document is presented in section 4.1.

The other two projects that followed entailed the design, testing and analysis of a model mill and a differential gearset. The two projects are presented in sections 4.2 and 4.3, respectively. These were both the final year projects done for the Mechanical Engineering Department of the University of Cape Town in 1995. The quality of the results obtained in these investigations was, however, limited by the little amount of time and funding available.

4.1 THEORETICAL BASIS FOR IN-OPERATION MEASUREMENT OF DRIVE LOSSES [14]

The formulation of a theoretical basis for the in-operation measurement of the drive-train losses is derived in reference 14. The analysis contains a description of the two models for quantifying the drive power dissipation on a tyre-mounted grinding mill. It also gives an indication of the types of loads that the system is subjected to during operation. The planar model, the first and simpler model to be analysed, assumes that the charge mass is uniformly spread longitudinally inside the mill shell. This implies that all the tyres on ***an*** **axle** experience equal loads. The second model, called the 3D model, assumes that the centre of mass of the charge is off-set from that of the shell longitudinally by a distance Y_c. This has an overall effect of imposing unequal left- and right-hand tyre forces on each axle. The planar and the 3D models are discussed further in sections 4.1.1 and 4.1.2, respectively.

4.1.1 THE PLANAR MODEL

Forces acting on a mill shell are presented in Figure 4.1. Appendix A presents a detailed theoretical solution for this model, as derived in reference 14. This solution provides a force, torque and power analyses. Equations (A1) through (A4), from Appendix A, give a torque balance of the shell about its longitudinal axis. This resultant relationship for the overall tyre tractive force, F_X, is,

$$F_X = \frac{m_c \cdot g \cdot X_c}{r_s} + F_{Nd} \cdot t_d \cdot \left(\frac{1}{r_d} + \frac{1}{r_s}\right) + F_{Ni} \cdot t_i \cdot \left(\frac{1}{r_i} + \frac{1}{r_s}\right) \qquad (4.1)$$

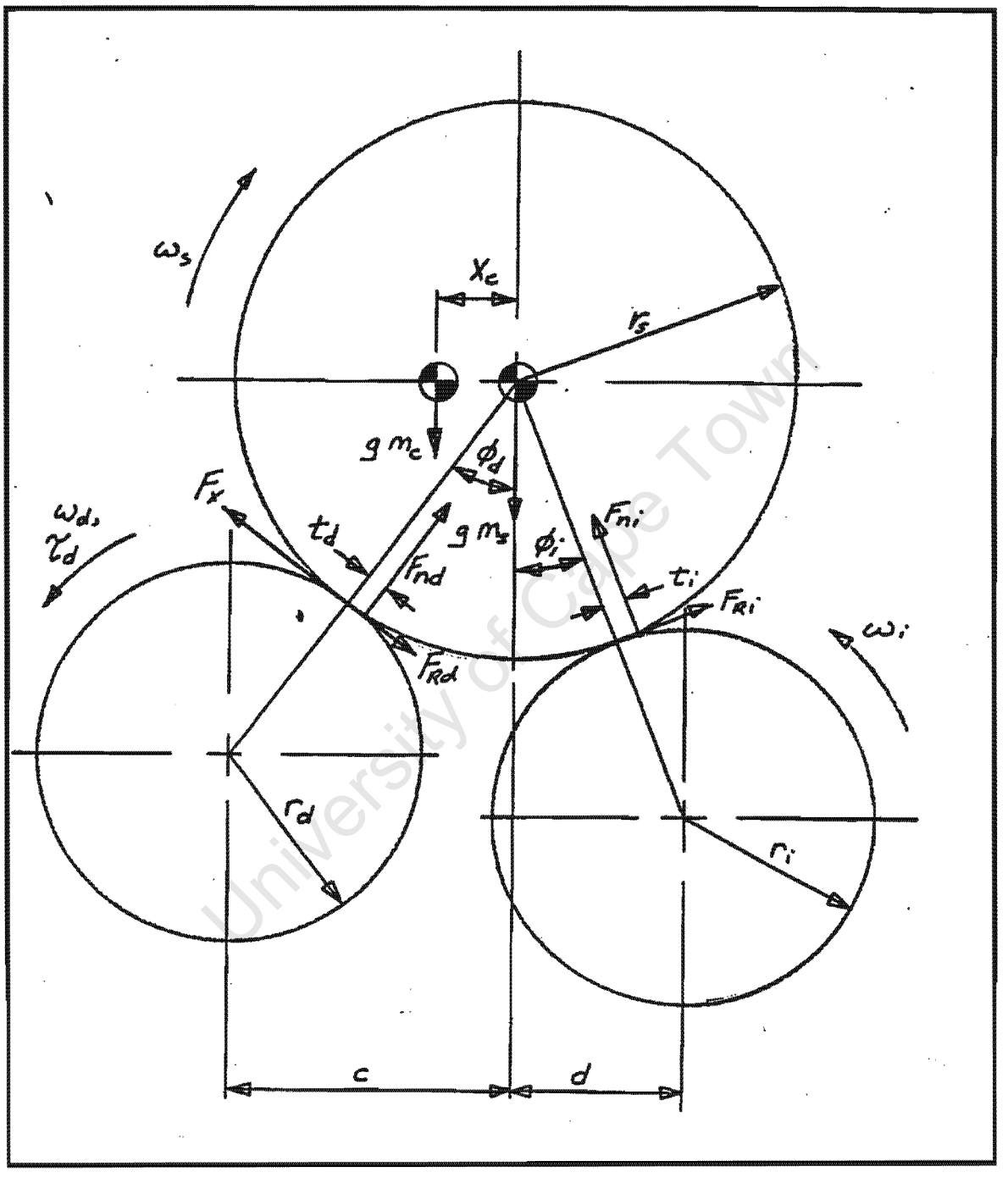

Figure 4.1 Forces acting on a mill shell.

where

m_c is the charge mass.

X_c is the offset of the charge centre of mass from the shell's longitudinal axis.

$F_{Nd,i}$ is the driver or the idler tyre normal force.

$r_{d,i}$ is the driver or idler tyre loaded radius.

$t_{d,i}$ is the driver or pneumatic trail. The pneumatic trail is defined as the length between the normal force of a tyre and the tyre's rolling axis.

r_s is the shell radius.

Horizontal and vertical force balances result in two simultaneous equations in terms of the normal components of the driver and the idler interaction forces, refer to equations (A6) and (A11). These relations are,

$$A \cdot F_{Nd} + B \cdot F_{Ni} = E \tag{4.2}$$

$$C \cdot F_{Nd} + D \cdot F_{Ni} = F \tag{4.3}$$

The parameters A, B, C, D, E and F are the variables dependent on parameters such as the tyre radii. This means that these two simultaneous equations cannot be solved in a straight forward manner as the tyre radii are *not* constant. Solutions for both F_{Nd} and F_{Ni} can be obtained if the tyre radii are modelled as follows,

$$r_d = r_{d0} - F_{Nd} \cdot k_{zd} \tag{4.4}$$

$$r_i = r_{i0} - F_{Ni} \cdot k_{zi} \tag{4.5}$$

where

r_{d0} and r_{i0} are un-deflected radii for both drive and idle tyres.

$k_{zd,i}$ is the drive or idle tyre compressibility [m/N].

The final solution for F_{Nd} and F_{Ni} is obtained by solving simultaneous equations (4.2) and (4.3) in an iterative manner. At this stage the frictional coefficient , μ_X, existing between the tyres and the shell can be obtained. It is defined as the ratio of the tyre tractive force and the normal force,

$$\mu_X = \frac{F_X}{F_{Nd}} \tag{4.6}$$

The LDVS tyre model was utilised in determining the longitudinal slip, i_d. With μ_X known, the longitudinal slip i_d was numerically solved for by means of equation (3.3). To estimate the drive power dissipation on this mill, an energy conservation analysis was performed. As shown in Appendix A, the total drive-train power losses are defined as the sum of tyre drive power losses due to tyre slip, the differential power losses and the driver and the idler rolling resistance. This is shown in the following relation,

$$P_{lds} = P_{ls} + P_f + P_{Rd} + P_{Ri} \tag{4.7}$$

or

$$P_{lds} = -P_d \cdot \eta \cdot i_d + P_d \cdot (1-\eta) + F_{Nd} \cdot t_d \cdot (\frac{1}{r_d} + \frac{1}{r_s}) \cdot r_s \cdot \omega_s + F_{Ni} \cdot t_i \cdot (\frac{1}{r_i} + \frac{1}{r_s}) \cdot r_s \cdot \omega_s \quad (4.8)$$

where

P_{lds} is the total drive-train power losses.

P_{ls} is the power lost due to tyre slippage.

P_{Rd} and P_{Ri} are rolling resistance power losses due to driver and idler tyres.

After deriving the above equations, a tentative parametric study was performed. Hypothetical values for the model input parameters were used. The charge mass was varied from 0 to 15 tons in 3-ton steps. The shell's angular velocity was held constant at 22 rpm. Figure 4.2 presents power losses plotted against charge mass. Noticeable features in these curves are that,

- P_{Rd} and P_{Ri} increase linearly with charge mass
- P_{ls} increases non-linearly with charge mass
- P_f increases non-linearly with charge mass too.

Figures A1 and A2, Appendix A, show the graphs of the tyre interaction forces (F_X, F_{Nd} and F_{Ni}) and the speeds of tyres and shell, respectively, plotted against charge mass. The interaction forces show a linear increase with an increasing charge mass, with F_{Nd} showing a very steep slope compared to the others. The idler tyre angular speed increases linearly with an increasing charge mass due to compression of the tyre, whilst the driver tyre speed increases non-linearly. At the time this parametric study was carried out, specific empirical data for the tyre-shell friction coefficient was not available.

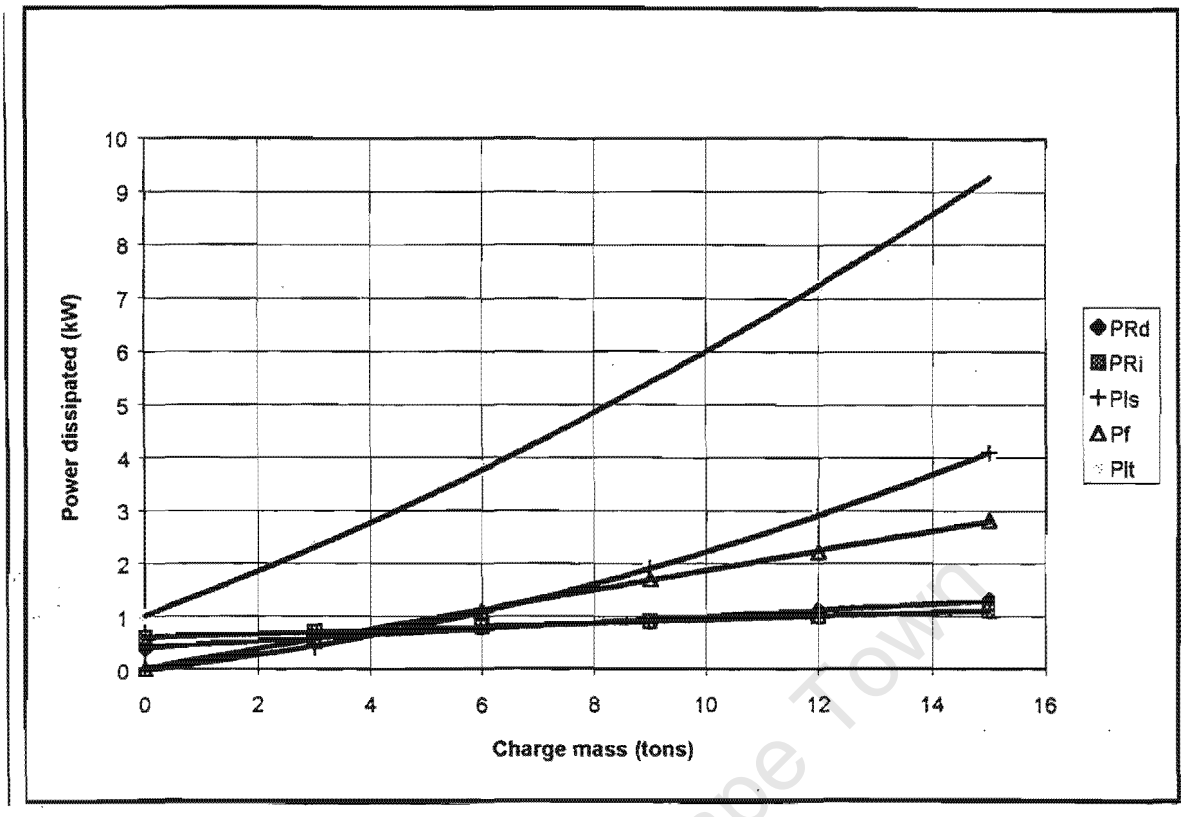

Figure 4.2 Power losses versus charge mass for the planar model.

However, this study showed that for large charge masses a reduction in the tyre friction leads to a drastic increase in power dissipation.

4.1.2 THE THREE DIMENSIONAL (3D) MODEL

This is the case for which the charge centre of mass is allowed to move longitudinally a distance Y_c from the shell's centre of gravity. Figure 4.3 shows this shift of the charge centre of mass away from that of the mill shell. This longitudinal shift means that the left- and the right-hand tyres on ***an*** axle will be loaded differently. These different loads experienced by the tyres will, tacitly, result in different deflections, for the same tyre inflation pressures.

In the analysis carried out in section 4.1.1 only three conditions had to be satisfied. These are the vertical force, the horizontal force and the rolling moment balances. For the 3D case, in addition to planar conditions still having to be met, pitching (rear view) and yawing (top view) moments have to be considered. These conditions demand a difference in the left- and right-hand tyre supporting force components.

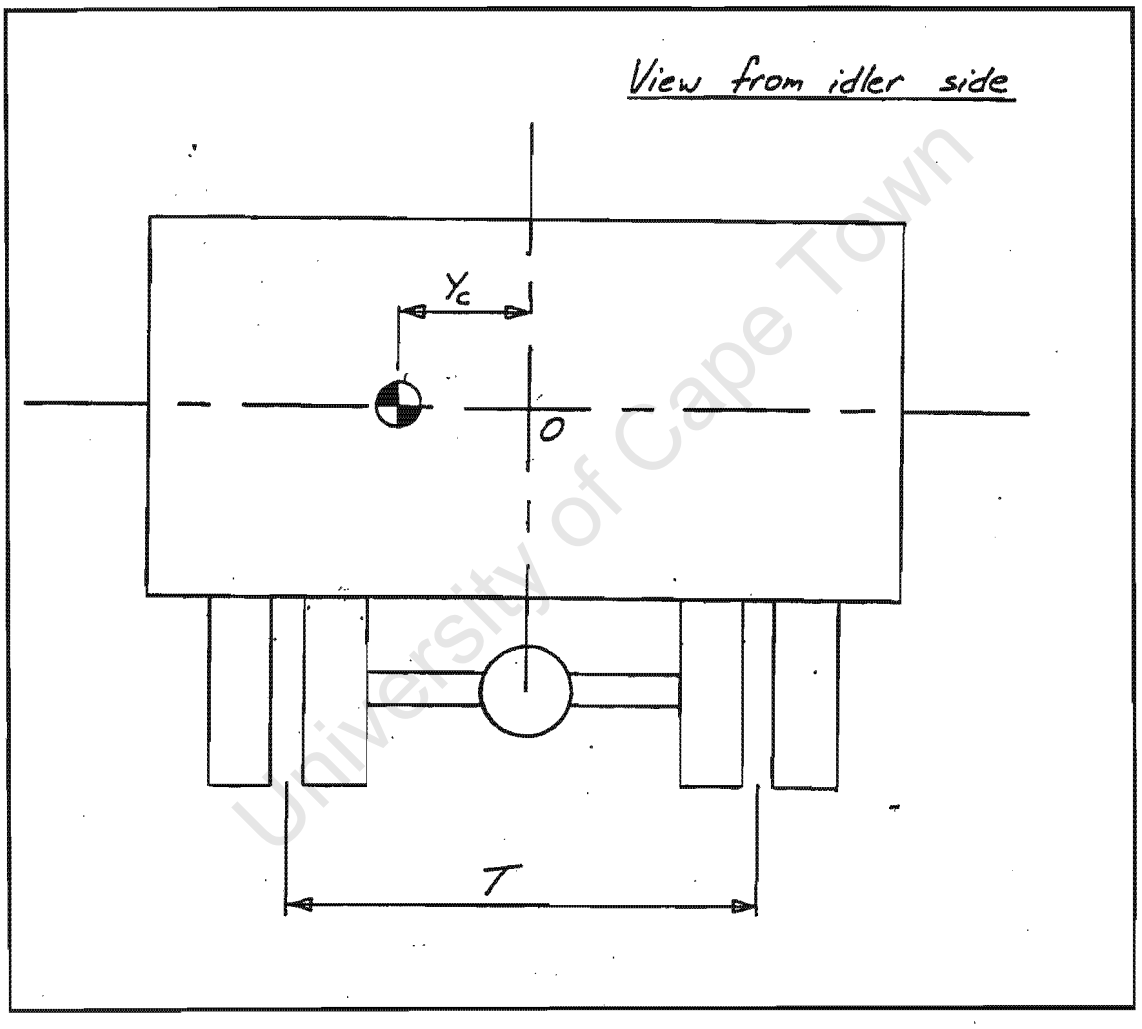

Figure 4.3 Longitudinal movement of charge centre of mass.

Before any analysis on the 3D model can be done, the type of a differential to be used has to be specified. Two types of differentials, i.e. an "open" and a "locked" differential, were considered. In the latter case the axes of planetary gears of the differential are firmly clamped, resulting in equal rotational speeds of the two half-shafts. An "open" differential is similar to a standard differential normally found in rear wheel driven cars. Planetary gears of the differential are allowed to rotate freely about their own axes, resulting in the same torque being imparted to the two half-shafts.

Appendix B presents a detailed force, moment and power analyses of this model, as derived in reference 14. Suppose the planar solution produced solutions for F_{Nd} and F_{Ni}, it is then assumed that the corresponding solutions will be as follows for the 3D case :

$$F_{Ndl,r} = \frac{F_{Nd}}{2} \pm \Delta F_{Nd} \tag{4.9}$$

$$F_{Nil,r} = \frac{F_{Ni}}{2} \pm \Delta F_{Ni} \tag{4.10}$$

with ΔF_{Nd} and ΔF_{Ni} being unknowns to be solved for.

The tyre radii are modelled similarly to the planar model, as follows,

$$r_{dl,r} = r_{d0} - 2 \cdot F_{Ndl,r} \cdot k_{zd} \tag{4.11}$$

$$r_{il,r} = r_{i0} - 2 \cdot F_{Nil,r} \cdot k_{zi} \tag{4.12}$$

Equations (B9) and (B14) show that the pitching and yawing moment balances are given as :

$$Q \cdot \Delta F_{Nd} + R \cdot \Delta F_{Ni} = V \tag{4.13}$$

$$S \cdot \Delta F_{Nd} + U \cdot \Delta F_{Ni} = W \tag{4.14}$$

where Q, R, S, U, V and W are variables dependent on the parameters such as tyre radii, tyre normal forces and drive tyre tractive forces.

The above equations are, clearly, simultaneous equations in unknowns ΔF_{Nd} and ΔF_{Ni} . They, however, **cannot** be solved in a straight forward manner due to the dependence of variables Q, R, S, U, V and W on the compressibility of the tyres. The solution procedure employed in evaluating ΔF_{Nd} and ΔF_{Ni} entails the determination of the planar solution. Then, F_X, F_{Nd} and F_{Ni} will be known. This planar solution has to be slightly perturbed to obtain the 3D solution. Improving the solution iteratively, ΔF_{Nd} and ΔF_{Ni} can be obtained.

The overall equation for predicting power losses in the 3D case has the same form as the one derived for the planar solution :

$$P_{lds} = P_{ls} + P_f + P_{Rd} + P_{Ri} \tag{4.15}$$

or, for an open differential :

$$P_{lds} = -P_d \cdot (\frac{\eta}{2} \cdot (i_{dl} + i_{dr}) - (1-\eta)) + F_{Ndl} \cdot t_{dl} \cdot (\frac{1}{r_{dl}} + \frac{1}{r_s}) \cdot r_s \cdot \omega_s +$$

$$F_{Ndr} \cdot t_{dr} \cdot (\frac{1}{r_{dr}} + \frac{1}{r_s}) \cdot r_s \cdot \omega_s + F_{Nil} \cdot t_{il} \cdot (\frac{1}{r_{il}} + \frac{1}{r_s}) \cdot r_s \cdot \omega_s + \quad (4.16)$$

$$F_{Nir} \cdot t_{ir} \cdot (\frac{1}{r_{ir}} + \frac{1}{r_s}) \cdot r_s \cdot \omega_s$$

In carrying out a parametric study, the mill drive power was calculated for various combinations of Y_c, m_c and f_{surf}. Charge mass values for which the study was carried out are 3, 9 and 15 tons. Figure 4.4 presents the results obtained. This study shows a strong increase of power dissipation for both a decreasing tyre-shell friction coefficient and an increasing value of Y_c.

4.2 DESIGN AND TESTING OF A MODEL MILL [15]

A project dealing with the design and testing of a model mill was allocated to a final year student in 1995 in the University of Cape Town Mechanical Engineering Department. The main purpose of this project was to determine power losses due to tyres in a tyre mounted ore grinding mill. The three dimensional diagram in Figure C1, Appendix C, presents the model mill concept. In this diagram the tyre drive shaft is nearest to the reader, and the shell rests on top of the tyres. The shell is represented by two steel disks connected by a shaft. The input power to the system is fed through the shaft indicated "From motor". The system drive power can either be supplied to the mill shell directly ***or*** through the tyre drive shaft by timing belts 2 or 1, respectively. The former

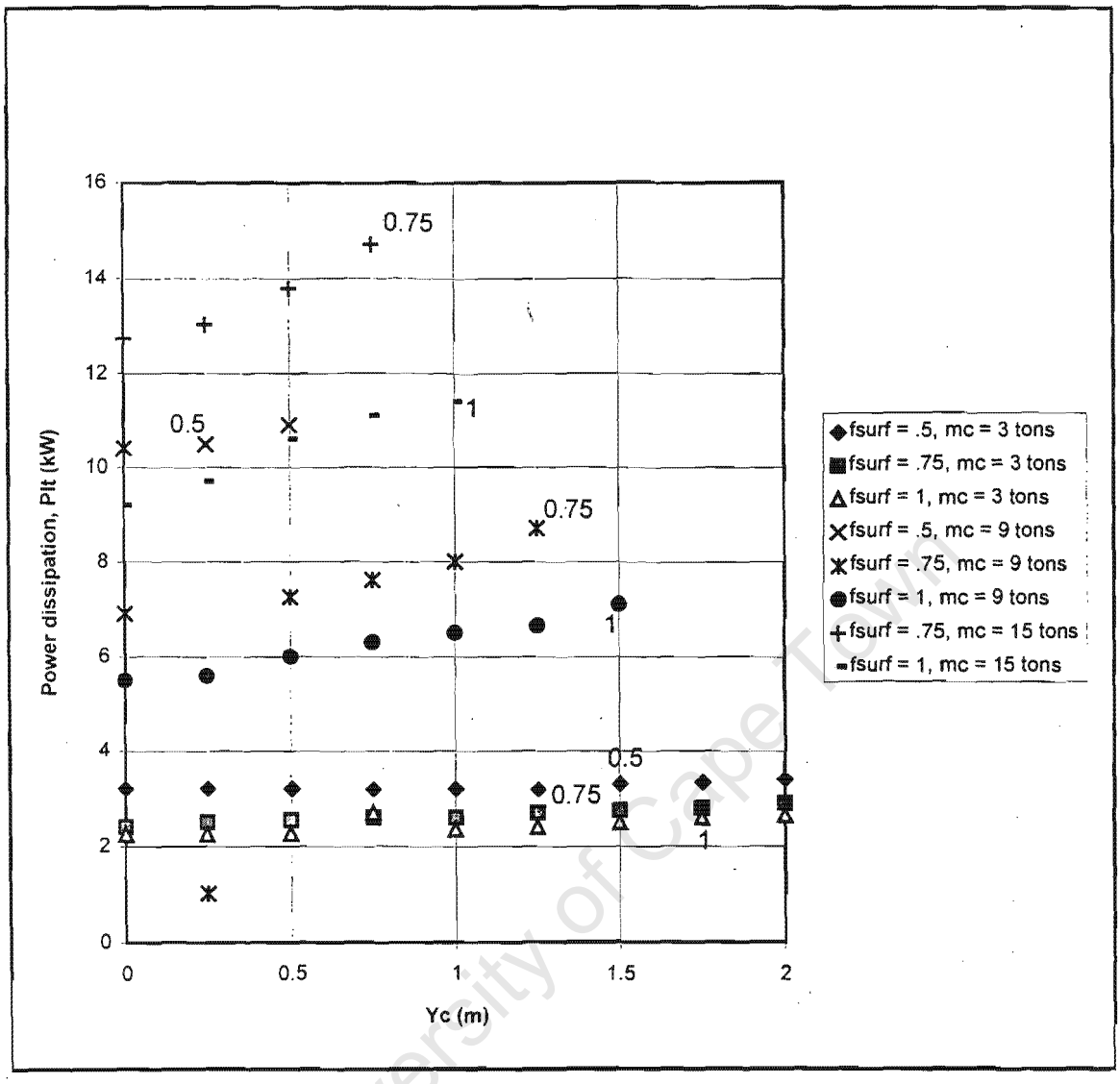

Figure 4.4 Power dissipation for the 3D model; i.e. using an "open" differential gearset.

arrangement aims at by-passing power losses due to tyres, whilst in the latter set-up these losses are encountered. This means that timing belts 1 and 2 cannot be engaged simultaneously.

Engaging timing belt 1 leads to the rotation of the drive tyre assembly. The torque is then imparted to the shell through the tyres. This in turn sets the idler tyre assembly in motion.

However, in engaging timing belt 2 the power goes directly to the shell. In this configuration the shell has to be lifted off the driver and idler tyre sub-assemblies, and must be mounted on bearings, i.e. the protrusions of the shell shaft have been made to allow for this feature. Tyre losses are, thus, eliminated when timing belt 2 is utilised in driving the shell. The difference in the power consumption between these two arrangements gives an indication of the power losses due to the tyres.

The output of the spur gear assembly goes to the generator. The generator acts as a brake to the shell, i.e. it resembles the charge mass. The radii of the spur gears and the spur gear assembly location have been chosen such that the resultant gear force acts vertically down at a reasonable offset from the shell's centre line. Due to the complex nature of the project, testing of the apparatus could not be refined nor completed in the prescribed time limits.

4.3 DESIGN AND TESTING OF A MODEL DIFFERENTIAL GEARSET[16]

Differential gearsets are utilised extensively in road vehicles. The differential's main purpose is to enable the vehicle to corner without the inner wheels scrubbing, and to act as the final speed reduction component. A differential gearset has been incorporated in the tyre mounted grinding mill with the main aim of enabling left- and right-hand tyres to rotate at different speeds. The aim of this study was to design, test and analyse a model of a differential gearset with the aim of obtaining its efficiency.

Figure 4.5 shows the top view of the assembled model differential gearset. The input torque is supplied through a spur pinion. A speed reduction ratio of 1:4 takes place at the pinion-crown wheel pair as the crown-wheel pitch diameter is approximately four times that of the pinion. The bevel gear arrangement is for imparting the rotation to the two half-shafts. Solution specifications for this design are shown in Table 4.1.

During the testing phase, the main aim was to determine the differential efficiency. Merritt [17] utilises the following equation to obtain the gearset efficiency, η :

$$\eta(\%) = 100 \cdot \frac{H_i - H_l}{H_i} \tag{4.17}$$

where H_i is the input power to the differential gearset.

H_l is the power lost by the differential gearset

As the gearset is started from rest its temperature rises from the ambient temperature, T_a, to a final equilibrium temperature, T_e, where T_e is reached only after a very long time, see Figure 4.6). As H_l is to correspond to the equilibrium temperature, a method is sought which avoids extremely long tests. Such a method is summarised by Merritt [17] and it entails the measurement of three temperatures, T_1, T_2 and T_3, at times t_1, t_2 and t_3, respectively, such that the intervals $(t_3 - t_2)$ and $(t_2 - t_1)$ are equal.

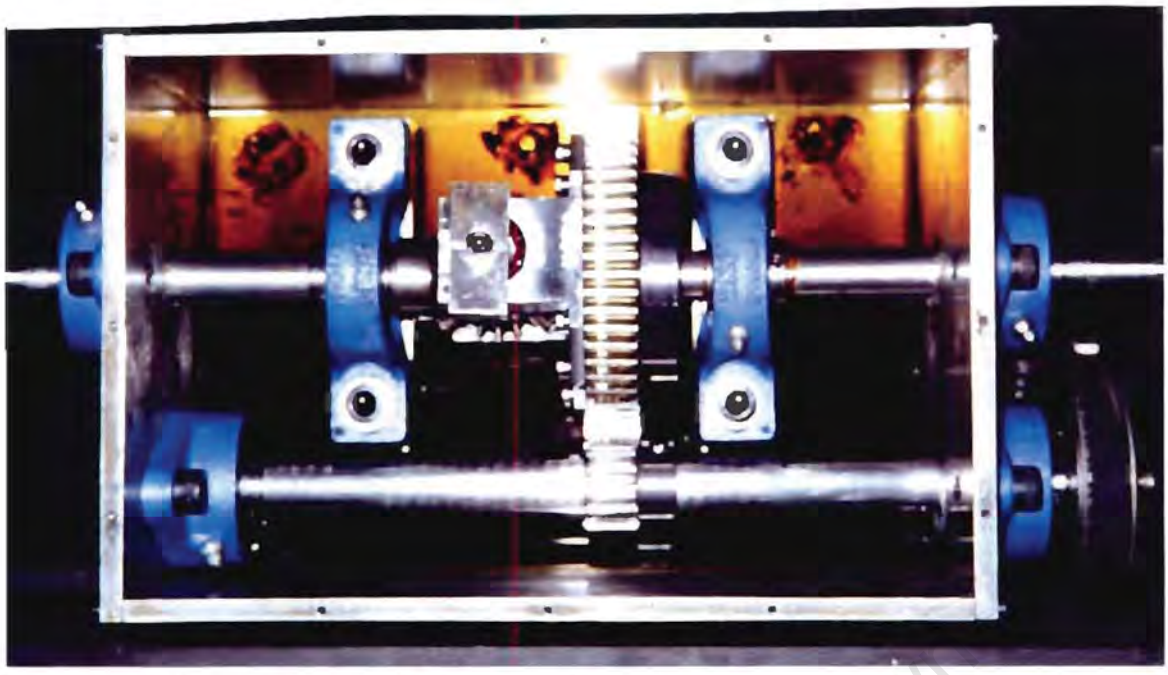

Figure 4.5 Picture of an assembled model differential gearset

Table 4.1 Solution specification of the model differential gearset

PARAMETER	SPECIFICATION
Total dry mass (kg)	34.5
Dimensions (mm)	308.9 * 195.0 * 183.0
Maximum input torque (Nm)	25.25
Maximum output torque (Nm)	99.40
Overall speed reduction ratio	1:4
Material : Casing Shafts Gears	 Mild steel Mild steel EN 8A (normalised)
Lubrication oil	BP gear oil
Mass of lubrication oil (kg)	1.5

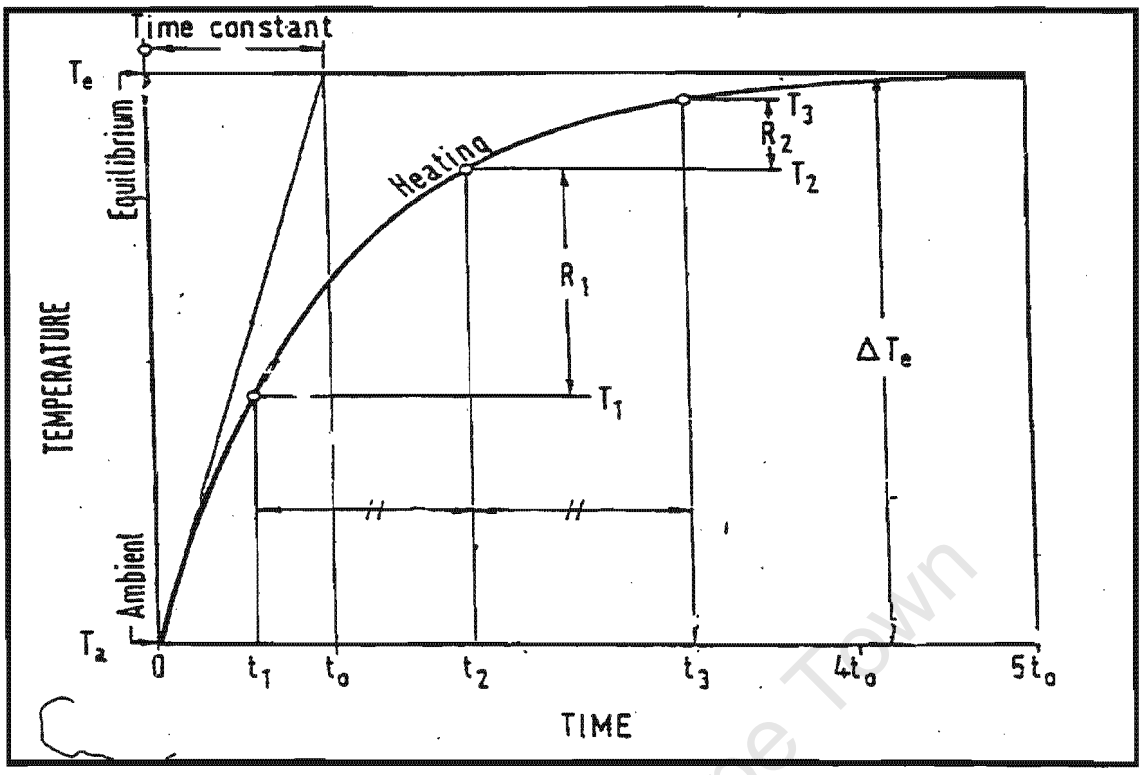

Figure 4.6 Theoretical heating curve of gearsets.

Setting

$$R_1 = T_2 - T_1 \tag{4.18}$$

$$R_2 = T_3 - T_2 \tag{4.19}$$

an approximation for T_e is found through Merritt's method as :

$$T_e = T_3 + \frac{R_2^2}{R_1 - R_2} \tag{4.20}$$

The thermal time constant, t_0, is defined as the time the gear-train would take to reach equilibrium temperature if all the heat continued to flow into the gear materials without any dissipation. This constant is now obtained from the equation,

$$e^{\frac{t}{t_0}} = \frac{\Delta T_e}{\Delta T_e - \Delta T} \tag{4.21}$$

or,

$$t_0 = \frac{t}{\ln(\frac{\Delta T}{\Delta T_e - \Delta T})} \tag{4.22}$$

where ΔT_e is defined as the difference between the equilibrium and ambient temperatures.

ΔT is the measured temperature rise in time t.

Now, defining and calculating a water equivalent factor, W_e,

$$W_e = \sum C_p \cdot m_g \tag{4.23}$$

where

C_p is the specific heat.

m_g is the mass of components.

The heat transfer factor, the product of C_H and A, is obtained by noting that

$$\frac{C_H \cdot A}{W_e} = \frac{1}{t_0} \tag{4.24}$$

where

C_H is the coefficient of heat dissipation.

A is the area of a gear-case.

Power losses at the equilibrium temperature are finally obtained from,

$$H_l = C_H \cdot A \cdot \Delta T_e \tag{4.25}$$

Two tests were carried out and the above relationships were utilised in attempting to quantify the differential's efficiency. For the first test a temperature rise of approximately 12 degrees Celsius was obtained in approximately 280 minutes. For the second test the input power was increased and a temperature rise of above 20 degrees Celsius was obtained in about 280 minutes. The recorded equilibrium temperature was 48.8 degrees Celsius whilst the one obtained using equation (4.23) was 50 degrees Celsius. An efficiency of 89.23 % was obtained after utilising the above relationships. Test 2 results are summarised in Figure C2, Appendix C. Thus, only two sets of data were analysed through the above analysis due to the time constraints.

CHAPTER 5. THE EXPERIMENTAL MODEL MILL

This chapter focuses on the experimental model mill design and concept. In order to relate the scale model and full-scale prototype engineering parameters, dimensional analysis and similitude are applied [18]. Section 5.1 presents the dimensional analysis and similitude method as applied to the tyre-mounted mill. Section 5.2 discusses the experimental model mill concept. A mathematical solution of this model is presented in section 5.3.

5.1 DIMENSIONAL ANALYSIS AND SIMILITUDE

The performance of many physical systems, e.g. that of a grinding mill, is determined by a large number of variables. It often happens that the variables involved are known while the relationship between them is not known. In these situations the application of dimensional analysis is highly appropriate as it indicates how to reduce the number of variables to be tested by grouping them into a set of dimensionless parameters, and allows the results obtained by means of experimentation with scaled models to be applied to full-scale prototypes.

In the present investigation dimensional analysis is applied in order to :

- Determine the appropriate model mill dimensions and rotational speeds.
- Determine the manner in which the variables have to be grouped into dimensionless groups such that the amount of experimentation may be minimised and the results may be presented in a way such that they may be directly applied to the full-scale prototype.

For the mill an unknown functional relationship between the tyre power loss, P_{lt}, and the other variables exists:

$$P_{lt} = P_{lt}(\tau, \rho_c, V, g, D, \omega_s, \mathrm{Pr}, Y_c) \tag{5.1}$$

where

τ is the torque applied to the wheels.

ρ_c is the charge density.

V is the volume of the charge mass.

g is the gravitational acceleration.

D is the shell diameter.

ω_s is the shell angular speed.

Pr is the tyre inflation pressure.

Y_c is the longitudinal offset of the centre of mass of the charge from that of the shell.

This expression contains nine variables. These various variables contain three basic dimensions, i.e. mass, length and time. According to Buckingham's Pi theorem [18] the nine variables may be reduced to six dimensionless groups. The application of this reduction technique to equation (5.1) results in the following simplified functional relationships :

$$\frac{P_{lt}}{\rho \cdot \omega_s^3 \cdot D^5} = F\left(\frac{\tau}{\rho \cdot \omega_s^2 \cdot D^5}, \frac{g}{D \cdot \omega_s^2}, \frac{V}{D^3}, \frac{Y_c}{D}, \frac{\mathrm{Pr}}{\rho \cdot D^2 \cdot \omega_s^2}\right) \tag{5.2}$$

The essence of this result is that if the functional relationship as expressed by equation (5.2) is determined experimentally by means of a scaled model, the power losses on the prototype mill may be predicted. Table 5.1 contains a summary of the comparison of model and prototype mill parameters which aim at achieving geometric, kinematic and dynamic similarities.

Table 5.1 Comparison of prototype and experimental model mill parameters

PARAMETER	PROTOTYPE	MODEL
Shell diameter, mm	1890	312.4
Tyre diameter, mm (drive and idle)	1232	203.2
Shell length, mm	3950	1140
Shell speed, rpm	22	54
Drive tyre speed, rpm	33.82	83.28

5.2 THE MODEL CONCEPT

The drive system of the model mill has been designed such that it resembles that of the prototype mill. The drive system comprises an electric motor, a wedge belt, a timing belt, a differential gearset and the tyres. These components are shown in Figure 5.1 as A, C, D, E and F, respectively. The electric motor and the differential gearset , A and E, are mounted in a back-to-back configuration on a mounting frame marked B in Figure 5.1. Power is transferred from A to E through the wedge and timing belts, C and D, respectively. The belt-pulley power transmission method also serves a role of stepping down the input speed to the differential gearset. A speed reduction of 1 : 2.92 is achieved through the use of these two belts. More pictures of the experimental model mill are presented in Appendix D.

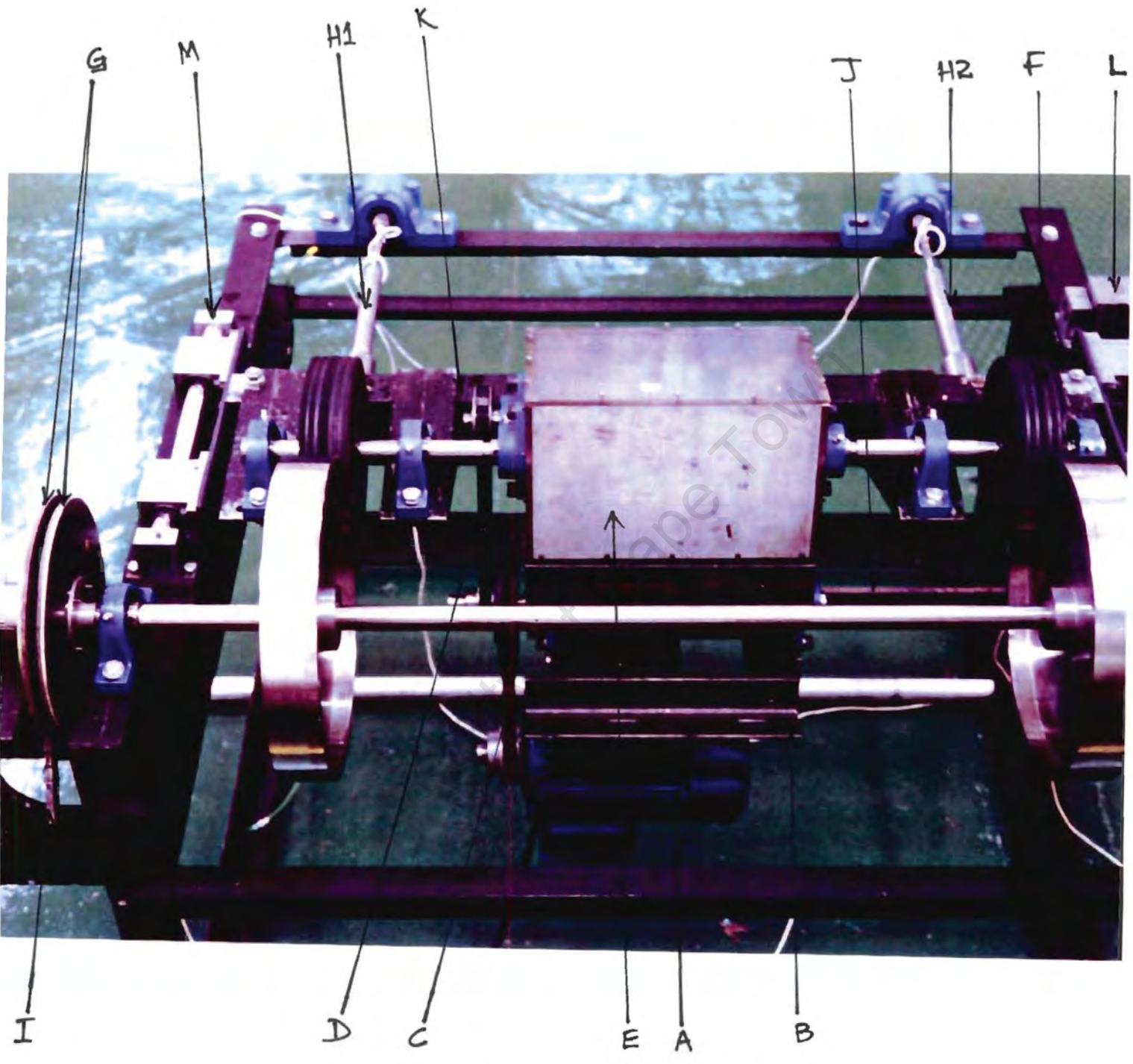

Figure 5.1 The experimental model mill.

A further speed reduction ratio of 1 : 4 is obtained inside the differential gearset. Thus, an overall speed reduction of about 11.67 is achieved between the motor output shaft and the differential gearset output shafts. This is adequate for rotating the tyres attached to the differential gearset output shafts and the shell at the required speeds. The mill shell is represented by two steel discs connected by a shaft.

5.2.1 SIMULATION OF THE CHARGE MASS

In the prototype mill, as the charge weight increases and progresses longitudinally inside the shell, the tyres on top of which the shell is mounted begin to deform. This feature is simulated in the model by pushing the tyres against the shell through the two push-rods, H1 and H2, via the frame marked K, see Figure 5.1. The model mill performance depends on whether these push-rods push the tyres equally or not, as they can be manoeuvred independently, and also on the mode of the differential gearset (open or locked). The resulting mill performance is outlined in section 5.3.

As the charge weight is simulated by the force exerted by push-rods, the measurement of the axial force acting on these rods gives the magnitude of the normal force acting on the tyres. As explained earlier, in this mill arrangement the tyre normal force represents the charge weight acting on the mill. The tyre normal forces acting on rods H1 and H2 are measured by strain gauges mounted on these rods.

Two linear bearing sub-assemblies, L and M in Figure 5.1, have been incorporated so as to allow for non-parallelism of the wheel drive shafts and the mill shell centreline. These linear bearing sub-assemblies are shown separately in Figures 5.2 and 5.3, respectively. The linear bearing sub-

assembly, L, allows for both longitudinal and lateral motions. This is due to the fact that when the two tyres are deflected differentially, frame K moves longitudinally as well as laterally. However, the lateral displacements experienced in this situation are not as marked as the longitudinal ones. Linear bearing sub-assembly M only allows for the longitudinal motion.

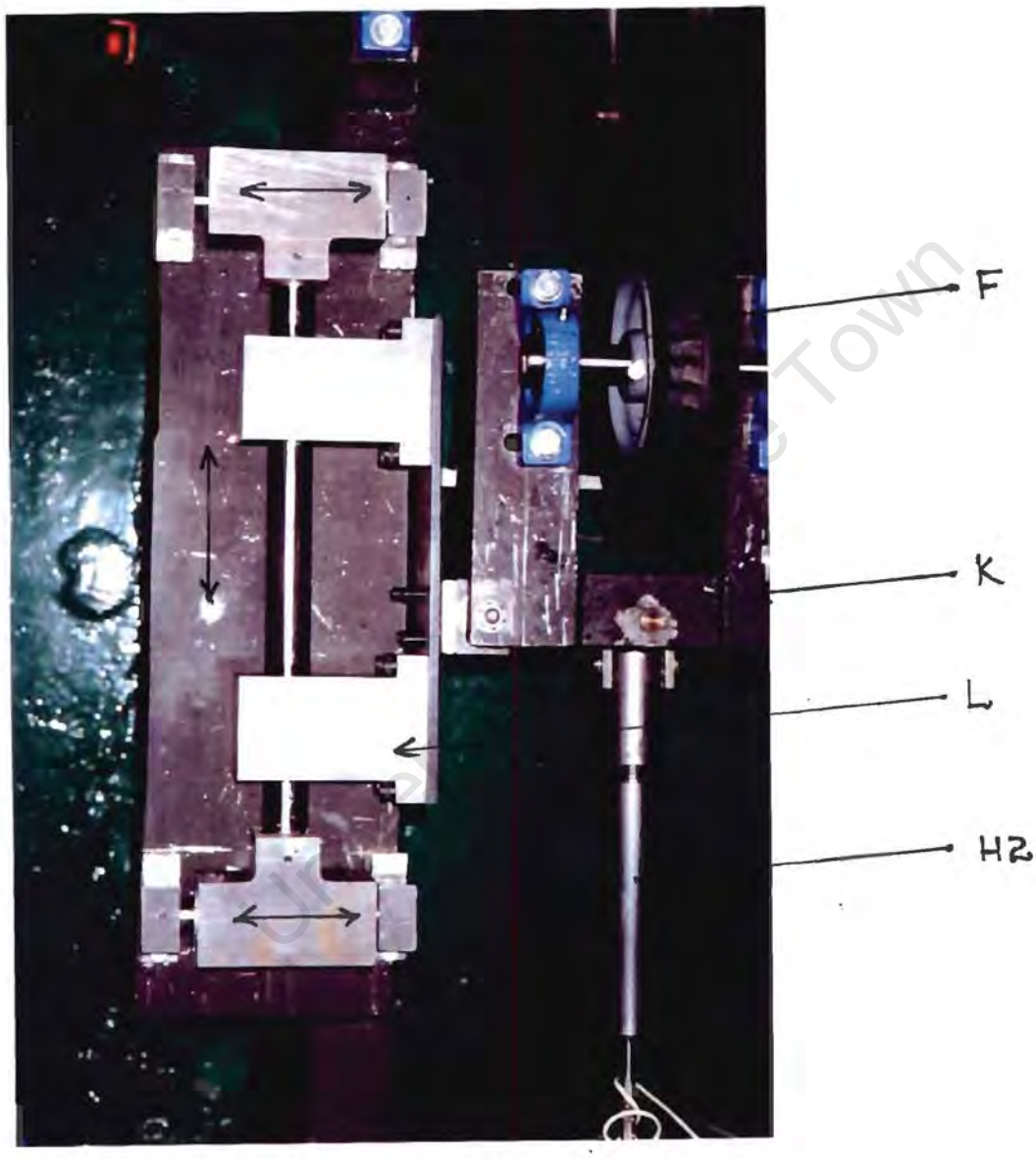

Figure 5.2 Linear bearing sub-assembly L.

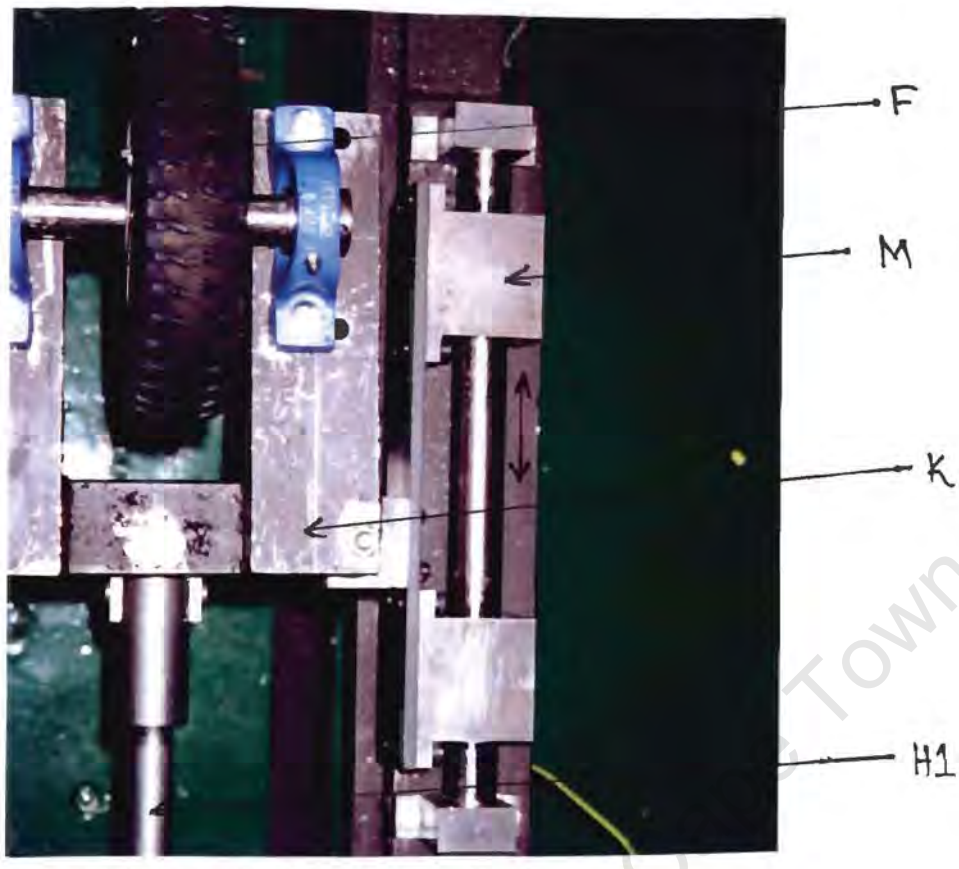

Figure 5.3 Linear bearing sub-assembly M.

5.2.2 POWER DISSIPATION ON THE MILL

For the disc brakes disengaged, marked G in Figure 5.1, the power losses occurring are minute as only the friction due to the bearings and gears, and the tyre rolling resistance have to be overcome. The disc brake sub-assembly, shown separately in Figure 5.4, has been incorporated so as to vary the power dissipation on the model mill as required. One brake disc is mounted on the shell shaft, whilst the other one is mounted on the side shaft with threads on the other end. A cantilever marked I is mounted on the latter disc to measure the torque imparted to the shell. When the disc brake mounted on the threaded side-shaft engages the one mounted on the shell shaft the overall

result is that the tyres are no longer rolling freely. Thus, more tractive force to keep the shell in motion is required from the tyres. The torque transferred by the tyres to the shell is measured by cantilever I and the torque input to the tyres is measured via cantilever J, see Figure 5.1, as is explained below.

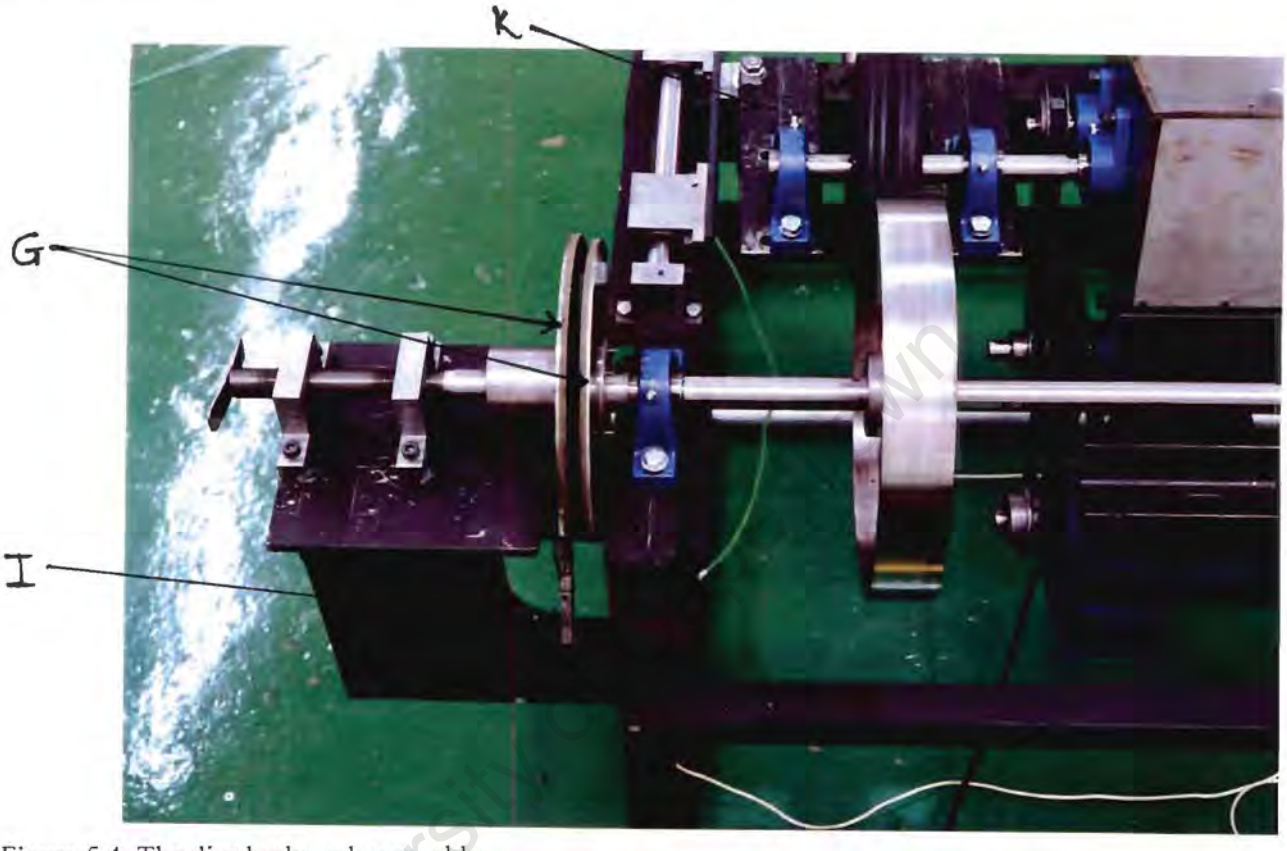

Figure 5.4 The disc brake sub-assembly.

The motor-differential gearset sub-assembly is such that it hangs on four bearings mounted on the differential gearset output shafts. These four bearings are fixed onto the frame marked K. This frame is, thus, used for mounting this sub-assembly and also to allow the application of the normal force to the shell by the tyres through rods H1 and H2. When the motor begins to run, any resistance occurring at the tyres will result in this sub-assembly swinging in the air since it hangs about the four bearings. A cantilever, component J, fixed to the model mill frame on one end, and touching component B on the other has been included in the design so as to stop this swinging of

the motor-differential sub-assembly. This cantilever will, in actual fact, enable one to measure the total differential gearset *output* torque. Strain gauges are mounted on this cantilever so as to quantify the magnitude of the force acting at its contact point with component B.

At this point the torque input to both the tyres and the shell are known. The corresponding tyre and shell speeds are measured by an angular speed measuring device, e.g. a tachometer. With all the above parameters being measured, the power input to the tyres and the shell can be evaluated. The difference between these two power parameters represents the amount of power dissipated by the tyres, and the power losses due to the gear and bearing friction.

5.3 THE MATHEMATICAL REPRESENTATION OF THE EXPERIMENTAL MODEL MILL

As in the case of the prototype mill, the model mill analysis can be performed by means of two different models. The first model, the planar model, simulates a case when charge mass is uniformly spread longitudinally inside the mill shell. The second model, the three dimensional (3D) model, simulates a case when the charge mass centre is off-set longitudinally from that of the mill shell.

5.3.1 THE PLANAR MODEL

This model is achieved by first operating the differential gearset as locked, and then loading the tyres equally during experimentation. The resulting model response is that both tyres will generate equal forces. The loaded tyre radius, r_d, is defined as,

$$r_d = r_{d0} - \frac{F_{Nd}}{K_{zd}} \tag{5.3}$$

where

r_{do} is the unloaded radius of a tyre.

F_{Nd} is the tyre normal force.

K_{zd} is the tyre stiffness [N/mm]. Note the difference between this quantity and the tyre compressibility given in chapter 4.

In order to obtain the amount of bearing, gear and tyre rolling resistances the model is operated with the disc brakes disengaged. This resembles a zero charge weight situation in the prototype mill. Carrying out a moment balance of the motor-differential gearset sub-assembly about the differential gearset output half-shaft centrelines results in :

$$2 \cdot F_{X0} \cdot r_d = K_m \cdot (\varepsilon_{m0} - \varepsilon_{m00}) \cdot h \tag{5.4}$$

where

F_{X0} is the tractive force for each tyre required to overcome the tyre rolling resistance, bearing and gear resistances.

K_m is the motor cantilever (J) stiffness [N/με].

ε_{m0} is the micro-strain measured from J whilst the motor is running with the disc brake is disengaged.

ε_{m00} is the micro-strain of J when the motor is not running.

h is the distance between centrelines of the differential half-shafts and J.

Rearranging equation (5.4) results in,

$$F_{X0} = \frac{K_m \cdot (\varepsilon_{m0} - \varepsilon_{m00}) \cdot h}{2 \cdot r_d} \tag{5.5}$$

When the disc brakes are engaged, the moment balance of the motor-differential gearset sub-assembly gives the following relationship for the overall tractive force, F_X, generated by each tyre,

$$F_X = \frac{K_m \cdot (\varepsilon_m - \varepsilon_{m00}) \cdot h}{2 \cdot r_d} \tag{5.6}$$

where ε_m is the strain of cantilever J when the disc brake is engaged.

The drive tractive force, F_{Xd}, of each tyre is defined as,

$$F_{Xd} = F_X - F_{X0} \tag{5.7}$$

or

$$F_{Xd} = \frac{K_m \cdot (\varepsilon_m - \varepsilon_{m0}) \cdot h}{2 \cdot r_d} \tag{5.8}$$

The brake torque, τ_b, is represented by,

$$\tau_b = K_b \cdot \Delta\varepsilon_b \cdot l_{tot} \tag{5.9}$$

where

K_b is the stiffness of the brake cantilever I.

l_{tot} is the total length of this cantilever.

$\Delta\varepsilon_b$ is the difference between strain readings of the brake cantilever taken when the disc brakes are engaged and when they are disengaged.

In carrying out a moment balance of the shell about its centreline the following relationships are obtained,

$$2 \cdot F_X \cdot r_s - \tau_b - 2 \cdot F_{Rd} \cdot r_s - 2 \cdot F_{Nd} \cdot t_d - \tau_\Delta = 0 \tag{5.10}$$

or

$$F_X = \frac{1}{r_s} \cdot [\frac{\tau_b}{2} + F_{Nd} \cdot t_d \cdot (1 + \frac{r_s}{r_d}) + \frac{\tau_\Delta}{2}] \tag{5.11}$$

where

$$F_{Rd} = F_{Nd} \cdot \frac{t_d}{r_d} \tag{5.12}$$

τ_Δ is the torque due to the bearing resistance.

Thus, F_{Xd} can also be evaluated using the following relationship,

$$F_{Xd} = \frac{1}{r_s} \cdot [\frac{\tau_b}{2} + F_{Nd} \cdot t_d \cdot (1 + \frac{r_s}{r_d}) + \frac{\tau_\Delta}{2}] - F_{X0} \tag{5.13}$$

The pneumatic trail of the tyres, t_d, is obtained during the no-load test. For the case of τ_b being zero, F_{X0} can be solved from equation (5.10) as :

$$F_{X0} \cdot r_s = F_{Nd} \cdot t_d \cdot (1 + \frac{r_s}{r_d}) + \frac{\tau_\Delta}{2} \tag{5.14}$$

Ignoring the bearing losses, τ_Δ, and calculating F_{X0} by means of equation (5.5) allows t_d to be determined from :

$$\Rightarrow t_d = \frac{F_{X0} \cdot r_s}{F_{Nd}} \cdot \frac{1}{1 + \frac{r_s}{r_d}} \tag{5.15}$$

The longitudinal slip, i, is defined as :

$$i = \frac{r_s \cdot \omega_s}{r_e \cdot \omega_d} - 1 \tag{5.16}$$

where r_s is the radius of the shell.

ω_s is the angular speed of the shell.

ω_d is the angular speed of the tyres.

r_e is the effective rolling radius of a tyre.

The effective rolling radius of a tyre is also obtained during the no-load situation. In this mode the tyre longitudinal slip is zero. Thus, the effective rolling radii of the tyres is obtained by imposing this condition in equation (5.16) and rearranging, as follows,

$$r_e = \frac{r_s \cdot \omega_s}{\omega_d} \tag{5.17}$$

When the disc brakes are engaged the existing tyre friction coefficient, μ_{Xd}, is defined as :

$$\mu_{Xd} = \frac{F_{Xd}}{F_{Nd}} \tag{5.18}$$

P_t and P_{ds} are defined as the total differential half-shaft power and the overall power transferred from the tyres to the shell, respectively. These quantities are obtained through the use of equations (5.19) and (5.20), respectively.

$$P_t = 2 \cdot F_X \cdot r_d \cdot \omega_d \tag{5.19}$$

$$P_{ds} = 2 \cdot \omega_s \cdot r_s \cdot (F_X - F_{X0}) \tag{5.20}$$

Note that $P_{ds} = 0$ if $F_X = F_{X0}$

The power lost between the differential gearset half-shafts and the shell, P_{lds}, is the difference of the power available at the half-shaft and the power available in the shell. Thus,

$$P_{lds} = P_t - P_{ds} \tag{5.21}$$

or

$$P_{lds} = 2 \cdot F_X \cdot (r_d \cdot \omega_d - r_s \cdot \omega_s) + 2 \cdot F_{X0} \cdot r_s \cdot \omega_s \tag{5.22}$$

$$\Rightarrow P_{lds} = -2 \cdot F_X \cdot r_d \cdot \omega_d \cdot (\frac{r_s \cdot \omega_s}{r_d \cdot \omega_d} - 1) + 2 \cdot F_{X0} \cdot r_s \cdot \omega_s \tag{5.23}$$

Define the drive longitudinal slip , i_d, as follows :

$$i_d = \frac{r_s \cdot \omega_s}{r_d \cdot \omega_d} - 1 \tag{5.24}$$

The drive longitudinal slip is related to the longitudinal slip as defined by equation (5.16) through the following relationship,

$$i_d = (i+1) \cdot \frac{r_e}{r_d} - 1 \tag{5.25}$$

Thus, P_{lds}, is given by,

$$P_{lds} = -2 \cdot F_X \cdot r_d \cdot \omega_d \cdot [(i+1) \cdot \frac{r_e}{r_d} - 1] + 2 \cdot F_{X0} \cdot r_s \cdot \omega_s \tag{5.26}$$

$$\Rightarrow P_{lds} = P_{ls} + P_R \tag{5.27}$$

where

$$P_{ls} = -2 \cdot F_X \cdot r_d \cdot \omega_d \cdot [(i+1) \cdot \frac{r_e}{r_d} - 1] \tag{5.28}$$

$$P_R = 2 \cdot F_{X0} \cdot r_s \cdot \omega_s \tag{5.29}$$

P_{ls} is defined as the power loss due to the tyre slippage.

P_R is the power loss due to the tyre rolling resistance plus bearing resistance. Note that the differential gearset power losses are excluded since the input torque to the tyres is measured at the differential gearset output.

5.3.2 THE 3D MODEL

The effect of a longitudinal off-set of the centre of mass of the charge from that of the shell is achieved by means of applying unequal normal forces to the tyres, and also operating the differential gearset as an open differential. In this mode the differential gearset ensures that the torque imparted to both half-shafts is equal. The parameters appearing in this model are described similarly to section 5.3.1, except for the subscripts *l* and *r* which denote the left- and right-hand sides of the model, respectively. The overall torques imparted to the tyres when the disc brake is disengaged, τ_{t0}, and engaged, τ_t , are given by the following relationships, respectively :

$$\tau_{t0} = K_m \cdot h \cdot (\varepsilon_{m0} - \varepsilon_{m00}) \tag{5.30}$$

and

$$\tau_t = K_m \cdot h \cdot (\varepsilon_m - \varepsilon_{m00}) \tag{5.31}$$

The torque imparted to each one of the two half-shafts is equal to half of the above values. Equations (5.32) through (5.35) present relationships for determining the left and the right hand tyre rolling resistance tractive forces, F_{Xl0} and F_{Xr0}, and the tractive forces when the disc brakes are engaged, F_{Xl} and F_{Xr}.

$$F_{Xl0} = \frac{K_m \cdot h \cdot (\varepsilon_{m0} - \varepsilon_{m00})}{2 \cdot r_{dl}} \tag{5.32}$$

$$F_{Xr0} = \frac{K_m \cdot h \cdot (\varepsilon_{m0} - \varepsilon_{m00})}{2 \cdot r_{dr}} \tag{5.33}$$

$$F_{Xl} = \frac{K_m \cdot h \cdot (\varepsilon_m - \varepsilon_{m0})}{2 \cdot r_{dl}} \tag{5.34}$$

$$F_{Xr} = \frac{K_m \cdot h \cdot (\varepsilon_m - \varepsilon_{m0})}{2 \cdot r_{dr}} \tag{5.35}$$

The following relationship is obtained from a torque balance of the shell with the disc brakes disengaged :

$$F_{Xl0} \cdot r_s - F_{Rdl} \cdot r_s - F_{Ndl} \cdot t_{dl} + F_{Xr0} \cdot r_s - F_{Rdr} \cdot r_s - F_{Ndr} \cdot t_{dr} - \tau_\Delta = 0 \quad (5.36)$$

The total power available at the two differential gearset half-shafts, P_t, is given by :

$$P_t = F_{Xl} \cdot r_{dl} \cdot \omega_{dl} + F_{Xr} \cdot r_{dr} \cdot \omega_{dr} \quad (5.37)$$

Ignoring the bearing losses, the power transferred from the tyres to the shell, P_{ds}, is defined as :

$$P_{ds} = r_s \cdot \omega_s \cdot [(F_{Xl} - F_{Xl0}) + (F_{Xr} - F_{Xr0})] \quad (5.38)$$

The total power lost by the tyres and bearings, P_{lds}, is derived similarly to the planar model, as shown below.

$$P_{lds} = P_t - P_{ds} \quad (5.39)$$

$$\Rightarrow P_{lds} = F_{Xl} \cdot (r_{dl} \cdot \omega_{dl} - r_s \cdot \omega_s) + F_{Xr} \cdot (r_{dr} \cdot \omega_{dr} - r_s \cdot \omega_s) + r_s \cdot \omega_s \cdot (F_{Xl0} + F_{Xr0}) \quad (5.40)$$

Longitudinal slip is defined in a similar form to the planar case (equation (5.16)), as follows,

$$i_{l,r} = \frac{r_s \cdot \omega_s}{r_{el,r} \cdot \omega_{dl,r}} - 1 \quad (5.41)$$

The resulting relationship for P_{lds} becomes :

$$P_{lds} = -F_{Xl} \cdot r_{dl} \cdot \omega_{dl}[(i_l + 1) \cdot \frac{r_{el}}{r_{dl}} - 1] - F_{Xr} \cdot r_{dr} \cdot \omega_{dr}[(i_r + 1) \cdot \frac{r_{er}}{r_{dr}} - 1] + r_s \cdot \omega_s \cdot (F_{Xl0} + F_{Xr0}) \tag{5.42}$$

$$\Rightarrow P_{lds} = P_{lsl} + P_{lsr} + P_{Rl} + P_{Rr} \tag{5.43}$$

where

$$P_{lsl} = -F_{Xl} \cdot r_{dl} \cdot \omega_{dl} \cdot [(i_l + 1) \cdot \frac{r_{el}}{r_{dl}} - 1] \tag{5.44}$$

$$P_{lsr} = -F_{Xr} \cdot r_{dr} \cdot \omega_{dr} \cdot [(i_r + 1) \cdot \frac{r_{er}}{r_{dr}} - 1] \tag{5.45}$$

$$P_{Rl} = r_s \cdot \omega_s \cdot F_{Xl0} \tag{5.46}$$

$$P_{Rr} = r_s \cdot \omega_s \cdot F_{Xr0} \tag{5.47}$$

Note that the final format of overall power losses occurring on the 3D system, equation (5.43), for the 3D case is similar to that of the planar model given by equation (5.27).

CHAPTER 6. CALIBRATION OF THE EXPERIMENTAL MODEL MILL

Calibration refers to a process whereby an engineer or an instrument user checks the response of an instrument with known input parameters. The importance of the calibration process before proceeding with experimentation cannot be overemphasised because it is calibration which firmly establishes the accuracy of any instrument [19]. This chapter discusses the calibration of the differential gearset output torque measuring cantilever, the brake cantilever, the push-rods and the tyres, respectively.

6.1 THE DIFFERENTIAL GEARSET OUTPUT TORQUE MEASURING CANTILEVER

This cantilever shall henceforth be referred to as the motor cantilever since it is positioned very close to the motor, see component J in Figure 5.1. It is used to measure the torque of the differential gearset output shafts. The maximum possible force expected to act on this cantilever during model mill testing was 190N. This force has been dictated by several mill parameters, namely, the maximum motor power, pulleys, gear sizes and the vertical distance of cantilever J from the differential gearset output shaft centrelines.

The motor cantilever was loaded from zero to 190.68N, and then back to zero. The two graphs presented in Figure 6.1 show the relationship between the load acting on the cantilever and the corresponding strain for the two loading cases. The two closely coinciding linear graphs show that the cantilever has very little hysteresis. The slopes obtained though linear regression are 0.09615 N/με and 0.096947 N/με for loading up and down, respectively. This results in an average value of .09655 N/με.

6.2 THE DISC BRAKE CANTILEVER

This is the device used to measure the torque acting on the shell. The disc brake cantilever is shown as item I in Figure 5.1. As outlined in section 5.2, this torque is the same as the tyre output torque. This cantilever was loaded from zero to 472.22 N, and then back to zero. Figure 6.2 shows two force versus micro-strain graphs, for the increasing and decreasing loading

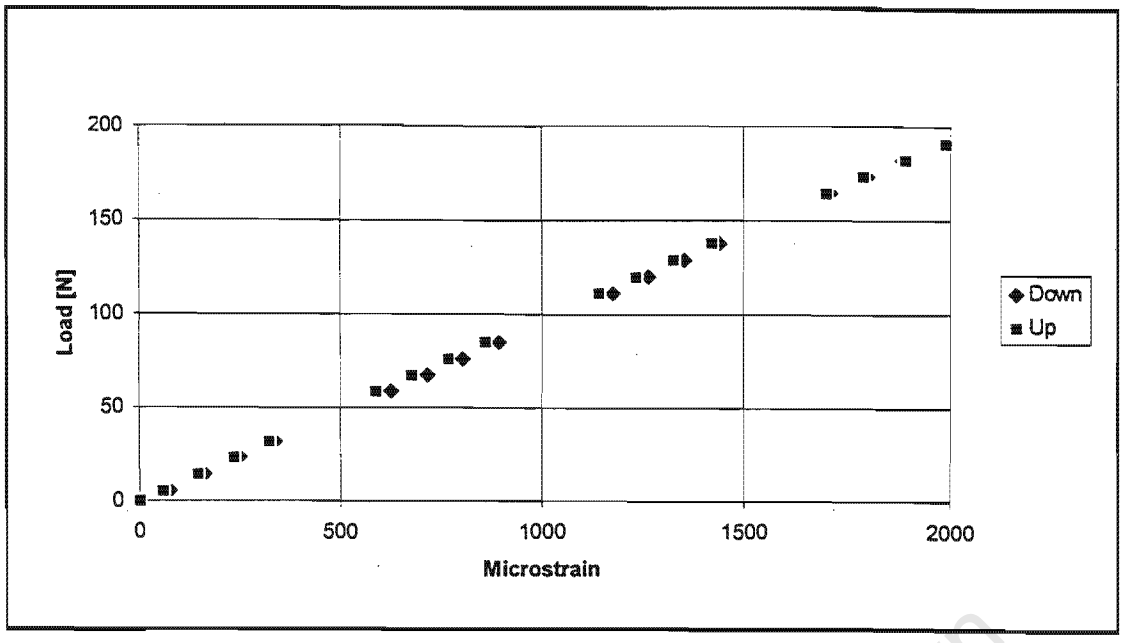

Figure 6.1. Load versus micro-strain for the motor cantilever.

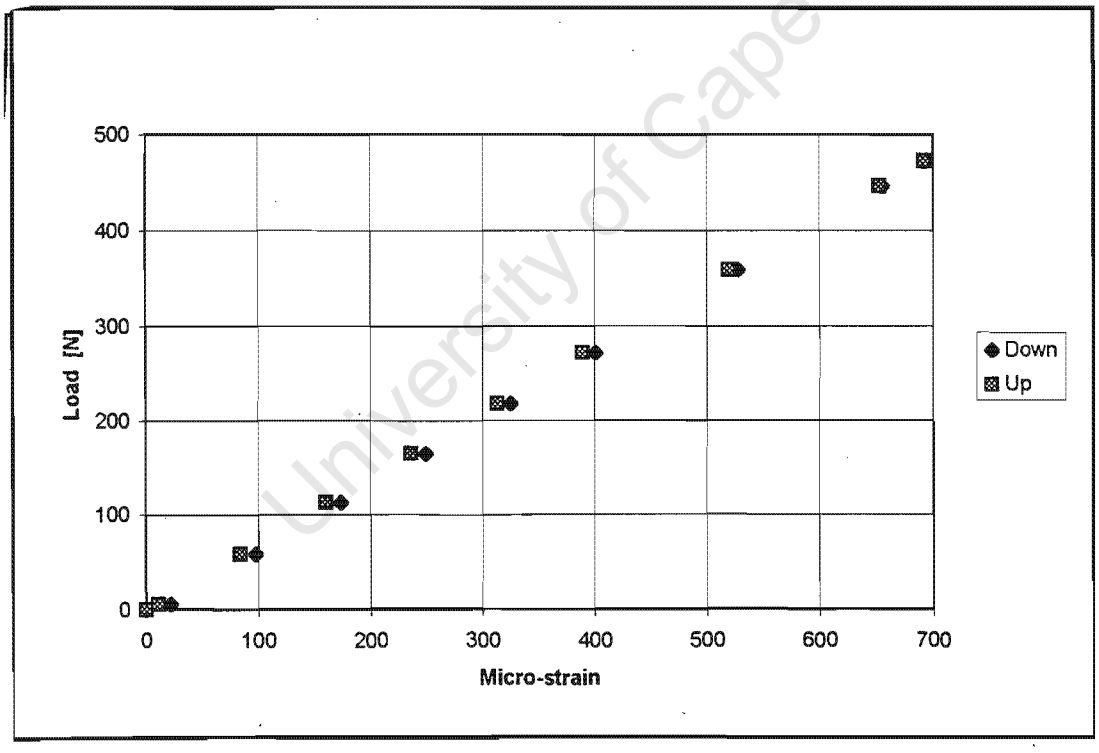

Figure 6.2 Force versus micro-strain for the brake cantilever.

applications. Slight Hysterisis also exists in this case. Slopes of 0.68312 and 0.69575 N/με were obtained through linear regression for both up and down loading cases, respectively. An average of these two values was obtained as 0.68944 N/με.

6.3 THE PUSH-RODS

The two push-rods, H1 and H2 in Figure 5.1, are used to apply the normal load to the tyres, thus simulating the charge weight. These two rods were loaded separately on an ESH testing machine in the Mechanical Engineering Strength Laboratory at the University of Cape Town. Both rods were loaded from zero to a force of approximately 600 N, and then back to zero. Figure 6.3 presents force versus micro-strain curves for rods H1 and H2, respectively. In this figure the curves for the loading up and down cases are coincident for each rod. Slopes of approximately

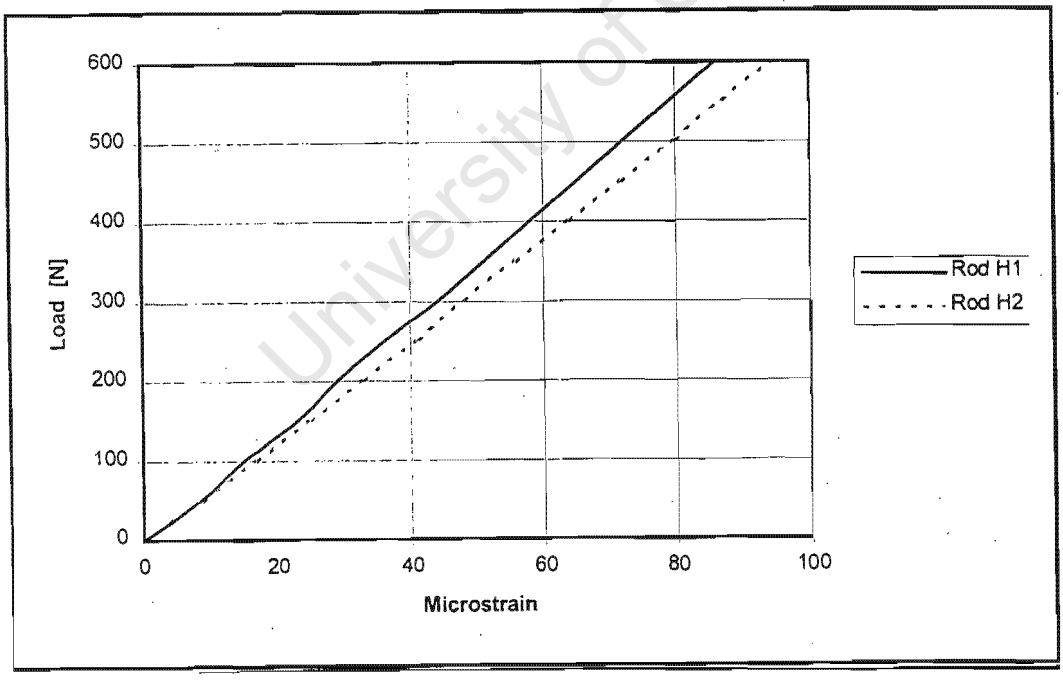

Figure 6.3 Force versus micro-strain for rods H1 and H2.

7.1667 N/με and 6.2500 N/με were obtained for H1 and H2, respectively. The reason that one cannot locate distinct experimental points in the curves of Figure 6.3 is due to the fact that these two curves were plotted by a pencil plotter which was directly connected to the ESH testing machine.

6.4 THE TYRES

Calibration of the tyres was performed so as to enable the prediction of the amount of tyre deflection for a known tyre normal force and inflation pressure. The tyre loaded radius of any pneumatic tyre depends on the tyre inflation pressure, the tyre normal force and the rubber material that the tyre is made of. For the same tyre type, only the first two parameters influence its loaded radius.

Three different types of tyre sets were calibrated and tested, i.e. two pneumatic tyre sets and one solid rubber tyre set. Table 6.1 presents the designation of these tyre types. As the tyres were calibrated in the model mill, the normal force acting on the tyres was measured through strain gauges mounted on rods H1 and H2, as outlined in the model concept section (section 5.2). The push-rods, H1 and H2, are threaded at the positions where they join component K. Knowledge of the thread pitch enables one to determine the tyre deflection by calculating the number of turns H1 and H2 have made.

When the tyre P1 was calibrated a major problem was experienced. It was noticed that H1 and H2 were subjected to a bending moment which affected the corresponding strain readings severely. Strain gauges in these rods were wired as a full-bridge so that any possible acting

Table 6.1 Designations of the tyre types used during experimentation of the model mill.

Tyre set number	Description	Designation
1	Type- pneumatic Size - 200mm * 50mm Maximum inflation pressure - 250 kPa Profile - similar to that of motor-bike tyres.	P1
2	Type - pneumatic Size - 203.2mm * 63.5 mm Maximum inflation pressure - 207 kPa Rating - 4 ply Profile - almost similar to that of ordinary road vehicle tyres.	P2
3	Type - solid rubber, Nylon centred Size - 200mm * 50 mm Profile - very flat.	S1

bending moment is cancelled, thus giving the required axial force. Contrary to this expectation, the axial force that was measured was severely affected by the existing bending moment to an extent that the obtained results could not be analysed. One set of the results obtained with the above bending moment effect is presented in Figure 6.4.

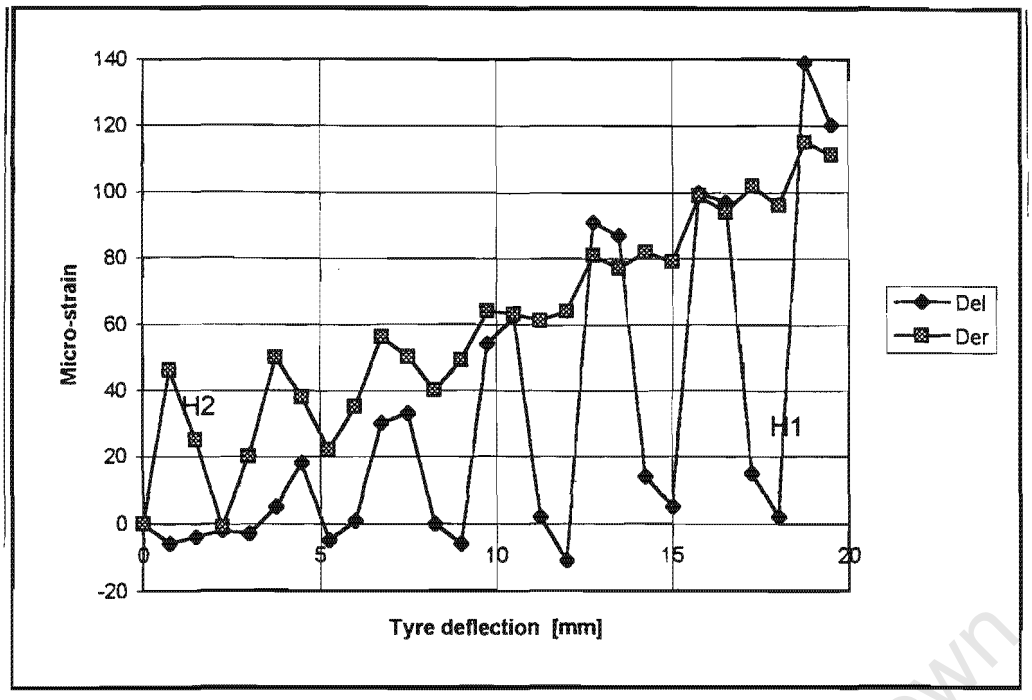

Figure 6.4 Micro-strain versus the tyre deflection for H1 and H2 subjected to a bending moment.

Since the bending moment acting on the rods could not be eliminated electronically, a means, be it mechanical or otherwise, was sought which would eradicate this bending moment. The result was that two hinges with two pivot axes were designed and incorporated in the mill design. One of these hinges is shown in Figure 6.5. It is connected to the component K and has a threaded nut onto which the thread at the end of the rods fit.

The pivot axes of these hinges are the vertical axis and the horizontal axis perpendicular to the axis of the rods. Thus, any moments about these axes are cancelled and only the required rods' axial forces are recorded. Once these hinges were utilised the resulting strain versus tyre deflection curves for the same conditions as those in Figure 6.4 are shown in Figure 6.6. As this figure shows, the hinges had done away with the bending moment problem on the push-rods to a very large degree. Though some scatter exists on one rod a mean value could be read off.

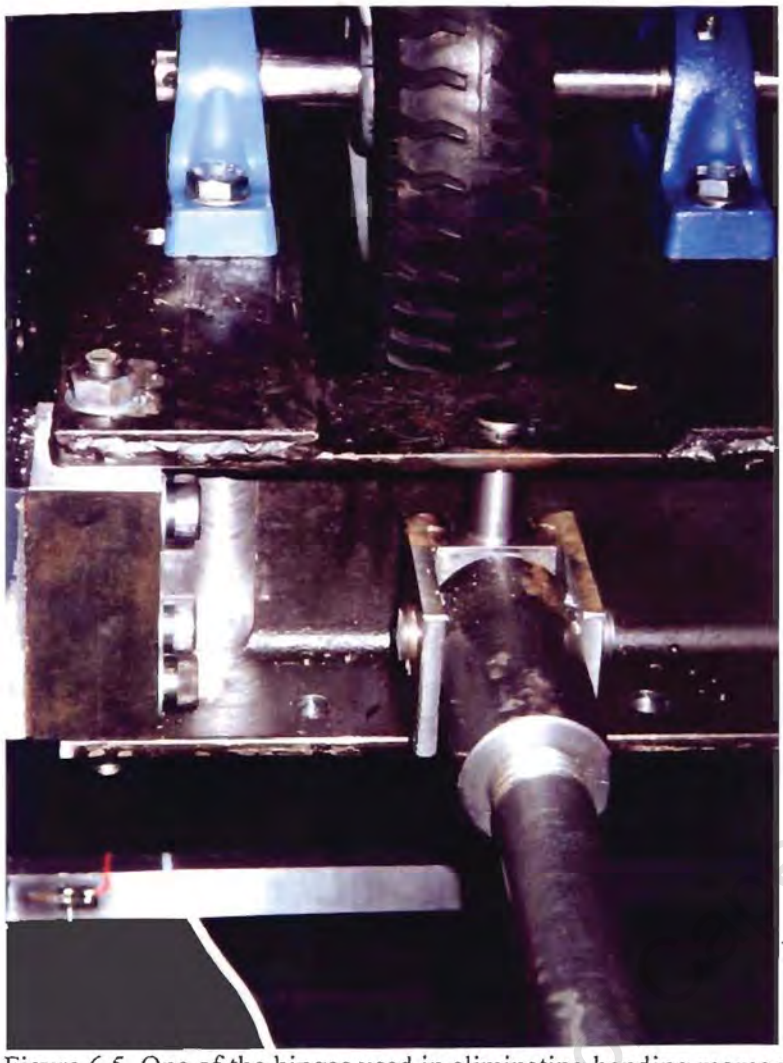

Figure 6.5 One of the hinges used in eliminating bending moments acting on H1 and H2.

The loaded radius of a tyre was defined in equation (5.3) as follows :

$$r_d = r_{d0} - \frac{F_{Nd}}{K_{zd}} \tag{6.1}$$

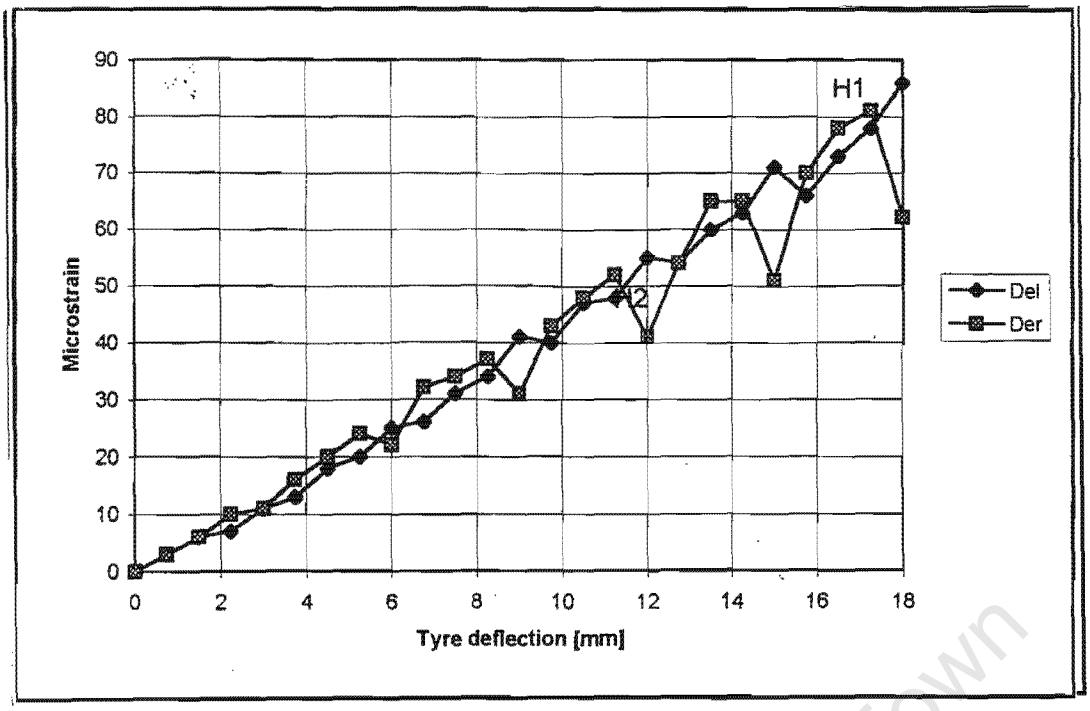

Figure 6.6 Micro-strain versus tyre deflection after incorporating the hinges in model mill.

Figure 6.7 presents the tyre loaded radius versus the tyre normal force for the tyre inflation pressures of 100, 140, 180, 220, 240 and 250 kPa for tyre P1. Only one tyre per set was tested for the stiffness, K_{zd}. Figure 6.7 shows that for every tyre inflation pressure there exists a unique tyre stiffness. Stiffnesses are obtained as the inverses of slopes of each graph. Figure 6.8 presents a graph of tyre stiffness values, derived from the above curves, versus the corresponding tyre inflation pressures.

Figure 6.8 was approximated by the following expression :

$$K_{zd} = 17.303 \cdot Ln(P) - 57.807 \qquad (6.2)$$

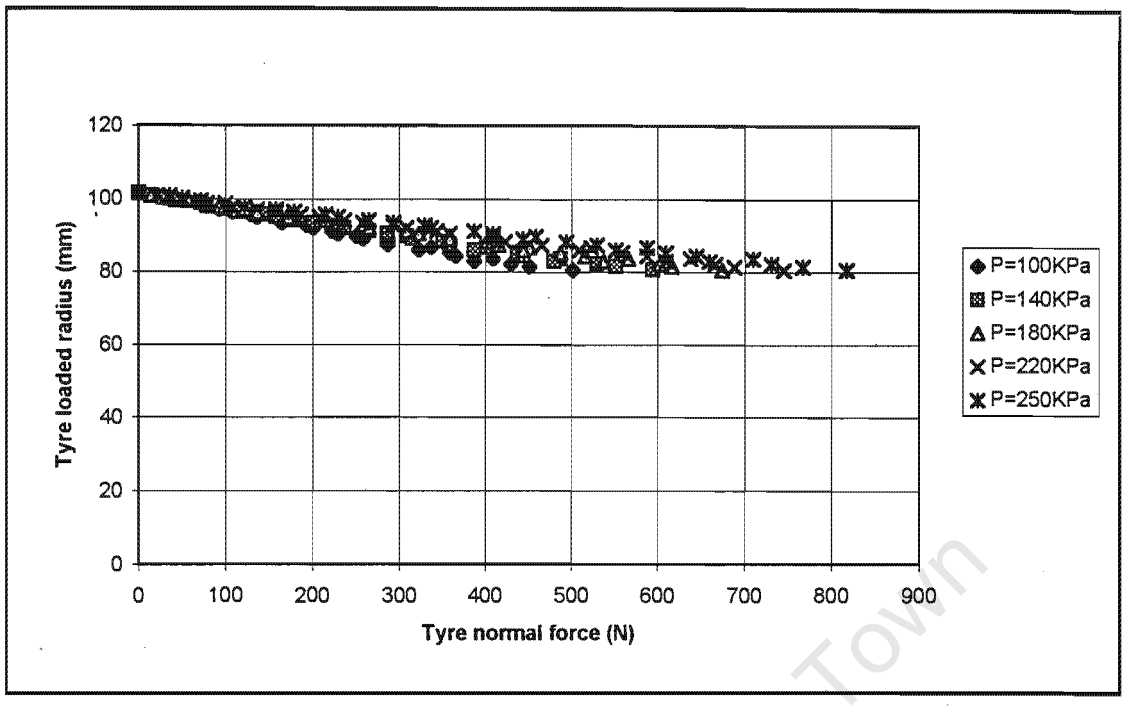

Figure 6.7 Tyre loaded radius versus normal force for tyre P1.

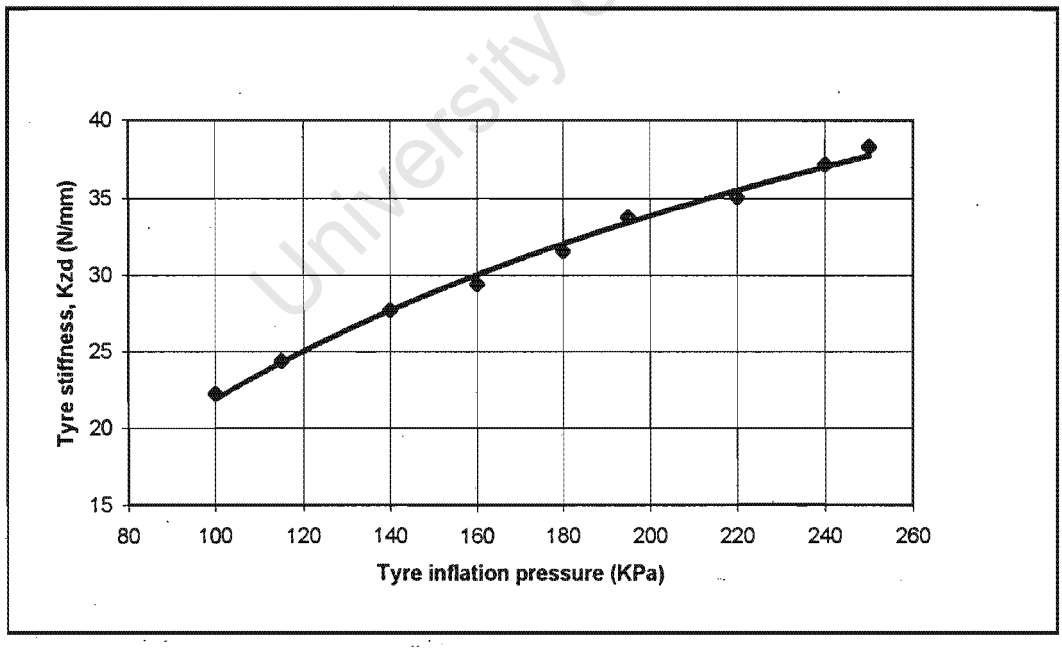

Figure 6.8 Tyre stiffness versus inflation pressure for tyre P1.

Figures 6.9 and 6.10 present graphs of tyre loaded radii versus normal force, and tyre stiffness versus inflation pressure, respectively, for tyre P2. An approximation of Figure 6.10 is given by equation (6.3).

$$K_{zd} = 15.302 \cdot Ln(P) - 42.22 \tag{6.3}$$

The third tyre type tested for its stiffness was the solid rubber tyre, S1. Figure 6.11 presents a graph of loaded tyre radius plotted against the normal force. From the inverse slope of this curve the stiffness was obtained as 74.3998 N/mm.

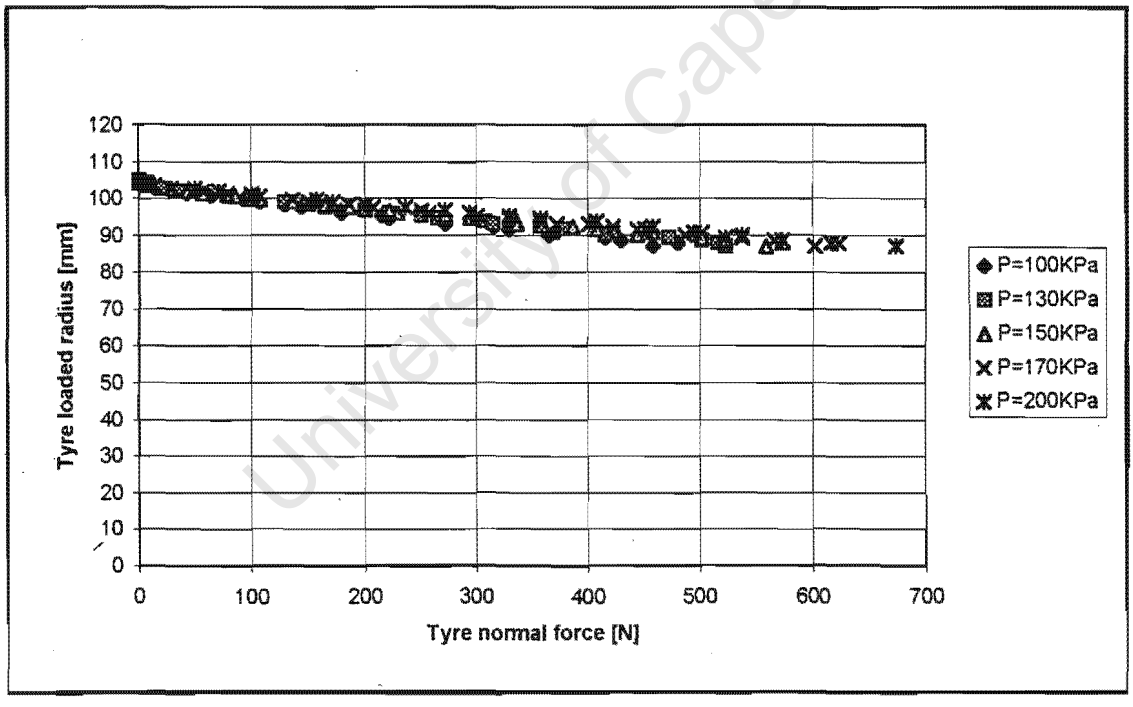

Figure 6.9 Tyre loaded radii versus normal force for tyre P2.

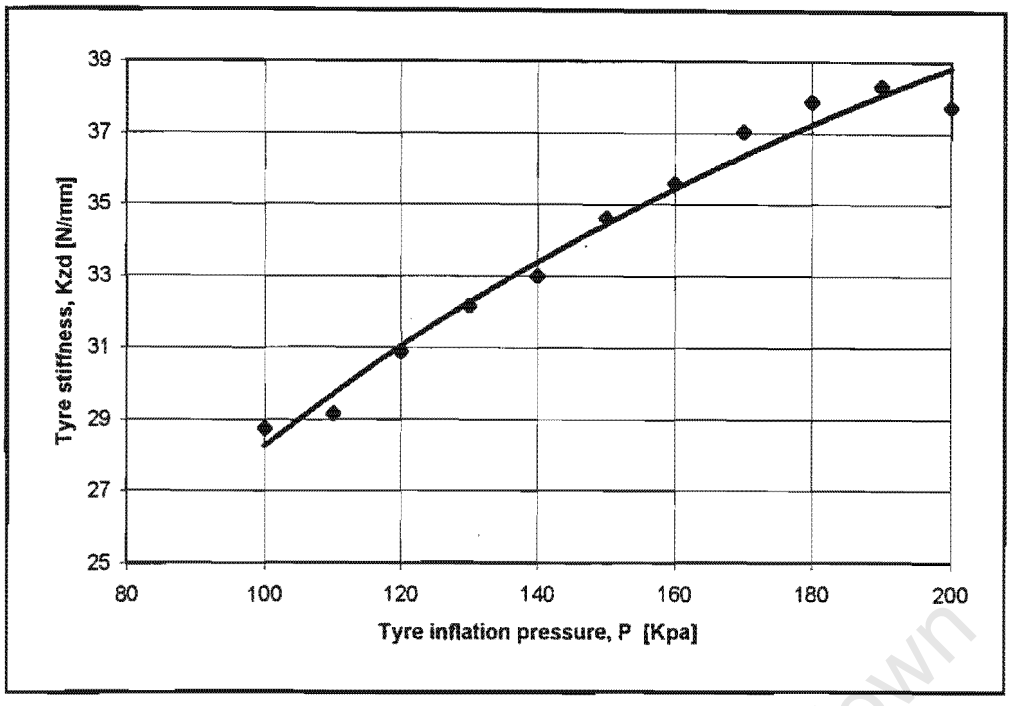

Figure 6.10 Tyre stiffness versus inflation pressure for tyre P2.

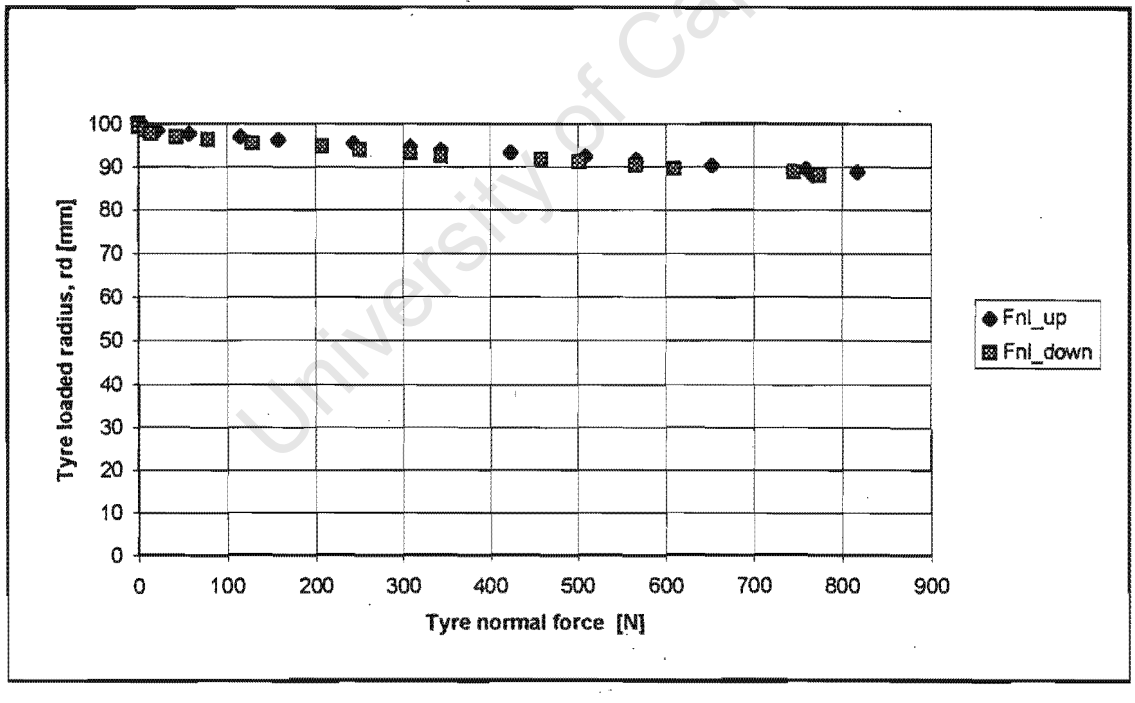

Figure 6.11 Tyre loaded radius versus normal force for tyre S1.

CHAPTER 7. EXPERIMENTATION WITH THE PLANAR MODEL

The aim of this project is to perform an empirical study on the model mill for both the planar and the 3D cases. Before a theoretical study can be carried out, the tyres have to be tested for the required empirical parameters. Results of the model mill performance obtained from the empirical study could, then, be compared with the theoretical analyses which are computer based.

As with any newly designed device there were several problems that needed to be sorted out, e.g. the bending moment problem on the push-rods discussed in section 6.4, after which real testing of the model mill resumed. The experimental procedure on the planar model is outlined in section 7.1. Section 7.2 discusses the testing of the model with the emphasis on determination of the tyre parameters needed for a theoretical study. The subsequent sub-sections deal with the experimentation and analysis of the planar model with the main objective of studying the drive-system performance of the mill.

7.1 THE EXPERIMENTAL PROCEDURE

The differential gearset of the model mill may be operated as either "open" or "locked". A differential gearset is referred to as an open differential when the planetary gears are allowed to rotate about their axes. However, for a locked differential gearset the planetary gears are firmly clamped and cannot rotate about their axes. The analysis in this chapter is based on operating the differential gearset in the locked mode.

During testing the tyres are first loaded to the required normal forces by cranking the push-rods H1 and H2 in or out (refer to Figure 5.1), as required. The disc brake is disengaged. Power is then supplied to the motor. Analysing the response of the motor cantilever gives the tyre tractive force, F_{X0}, required to overcome the rolling resistance and the bearing resistance.

After obtaining the tyre rolling resistance tractive effort the disc brake is engaged slightly so as to introduce some resistance to the shell, and subsequently to the tyres. Parameters such as the shell speed, the tyre speed, the motor cantilever strain and the brake cantilever strain are recorded. The disc brake is then engaged in steps, with the above parameters being measured for every new disc brake engagement position. The disc brake is engaged until the tyres cannot produce any more tractive force. The tyres usually produce a scratching noise at this point, and the motor is stopped. Data is analysed using relationships developed in section 5.3.1. Thus, the tyre tractive properties are investigated for a constant value of the tyre normal force. A new normal force is introduced to the tyres and the whole procedure outlined above is repeated over again. This is done until the number of the required test sets has been completed.

7.2 DETERMINATION OF THE TYRE PARAMETERS REQUIRED BY THE LVDS TYRE MODEL

Before a theoretical mill performance analysis can be performed, the tyre properties need to be obtained. An attractive feature of this model is that when operated in the planar mode, the required tyre parameters can be obtained. Actually, when the model mill was designed, the concept was formulated such that no other test rig would be required for testing tyres for the required parameters.

The tyre parameters to be tested for in this study are those required by the LVDS tyre model presented in chapter 3.4. Equations (3.3) through (3.10) were presented in that section and they relate the tyre friction coefficient to the longitudinal slip. In order to utilise these equations with success, the parameters appearing in equations (3.4) through (3.9) need to be obtained. Thus, if one can determine the tyre parameters P_0, P_1, P_2, R_0, R_1 and C'_η for a particular tyre, then, for any given F_{Nd} and F_{Xd} one can solve for i_d in equation (3.3).

It is clear from the tyre equations that several friction coefficient versus longitudinal slip graphs have to be generated in order to determine the required tyre parameters. The tyres P1 were tested for the parameters appearing in the above equations. As these tyres were made out of a soft-rubber material, only one set of results was generated. Figure 7.1 presents the friction coefficient versus longitudinal slip curve generated with this set of results. At the end of this test these tyres were severely worn out and could not be used anymore. Since the tyres P1 were severely worn out after this test, as shown in Figure 7.2, the required parameters could not be obtained for them.

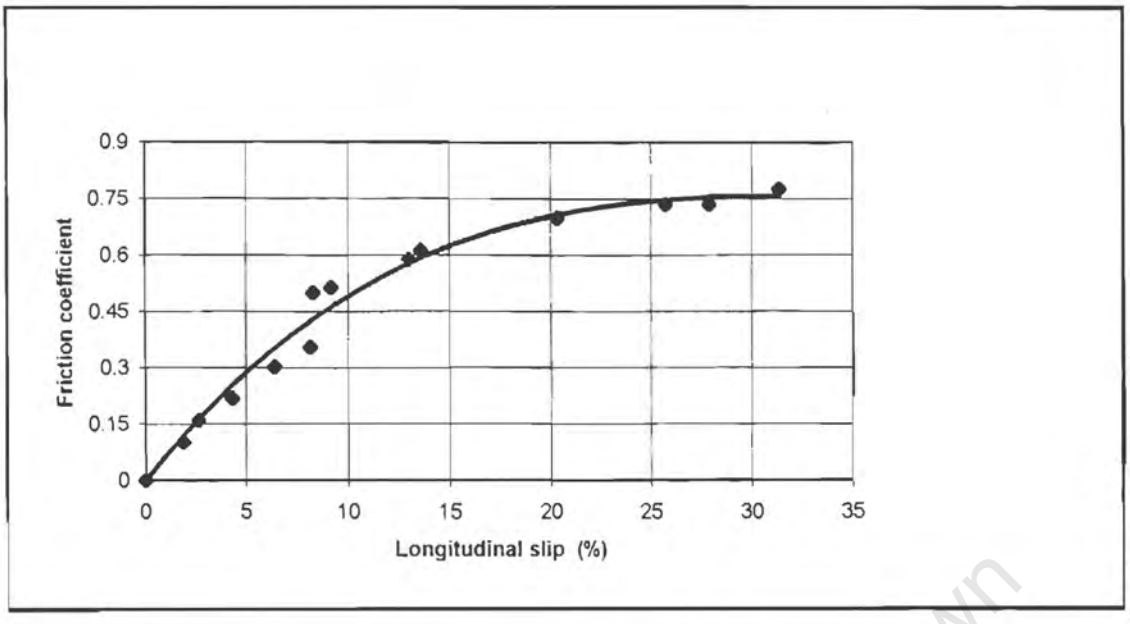

Figure 7.1 Tyre friction coefficient versus longitudinal slip for tyres P1.

Figure 7.2 Pneumatic tyre after generating the data used to develop Figure 7.1.

A second and a stronger set of pneumatic tyres was then tested, type P2. Figure 7.3 presents four graphs of friction coefficient versus longitudinal slip where each graph corresponds to a particular tyre normal force, F_{Nd}. The peak tyre friction coefficient, μ_P, and the corresponding longitudinal slip, i_{dp}, were recorded for all the curves that appear in Figure 7.3. Figures 7.4 and 7.5 present μ_P and i_{dp} versus F_{Nd} graphs, respectively.

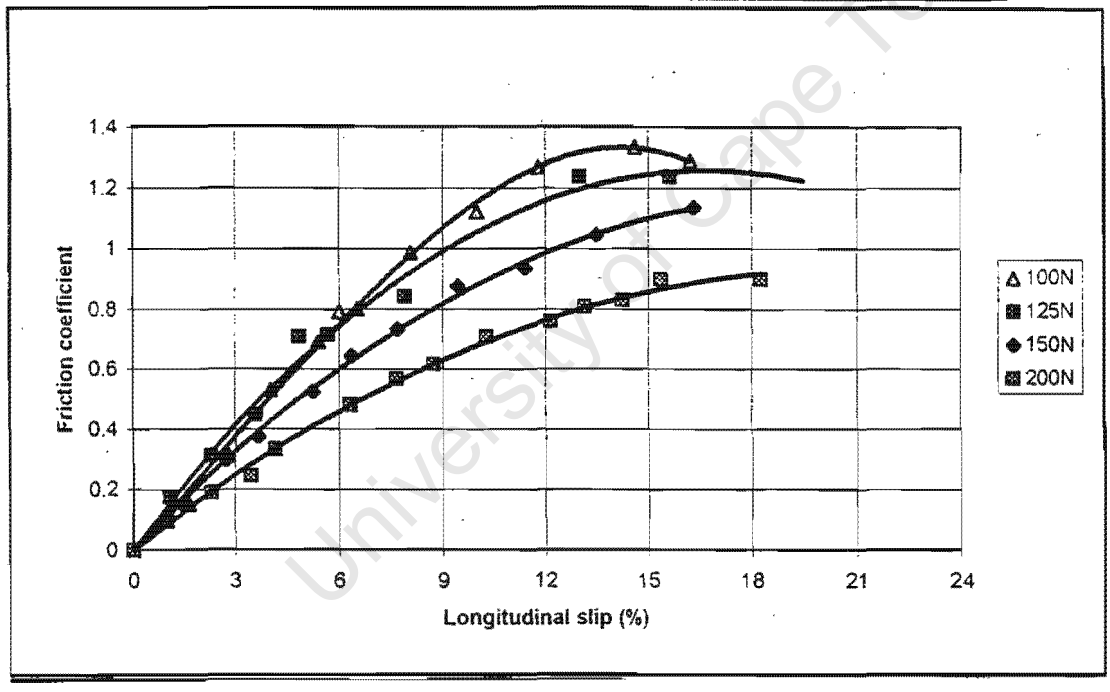

Figure 7.3 Tyre friction coefficient versus longitudinal slip for tyres P2.

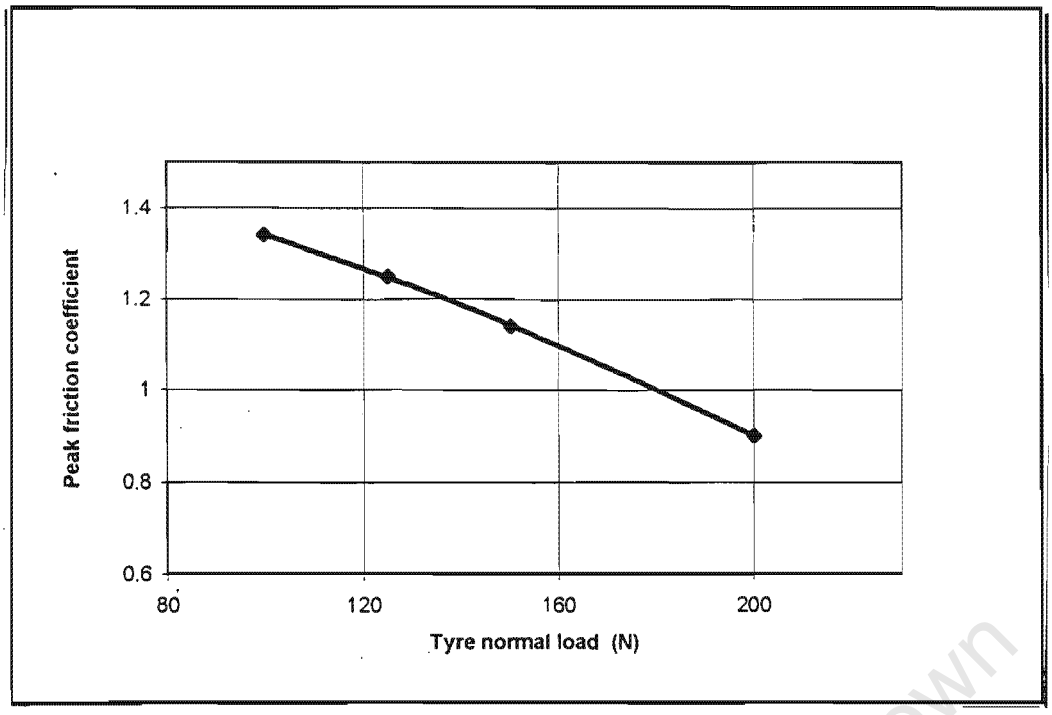

Figure 7.4 Peak friction coefficient versus tyre normal force.

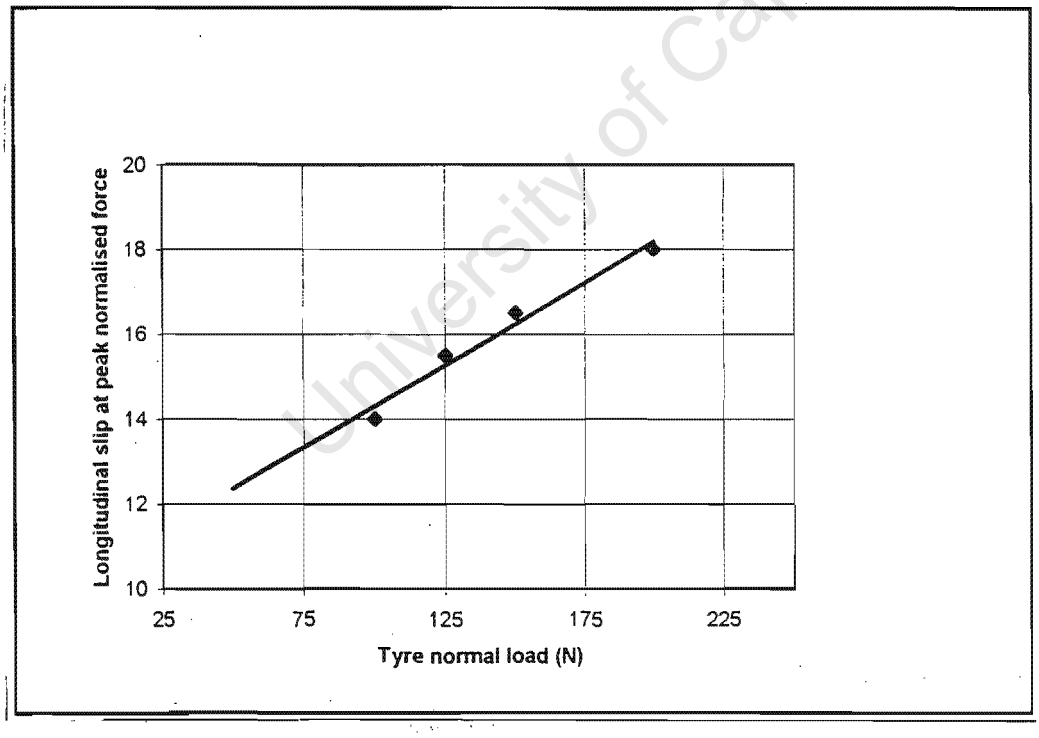

Figure 7.5 Longitudinal slip at peak friction coefficient versus tyre normal force.

The graphs of Figures 7.4 and 7.5 were fitted by the appropriate regression techniques, and the following values for the required tyre parameters were obtained :

$P_0 = 1.608$

$P_1 = 0.0018$ [1/N]

$P_2 = -9e(-6)$ [1/N^2]

$R_0 = 0.10414$

$R_1 = 0.000389$ [1/N]

The tyres S1 were tested through the same testing procedure as P2. The corresponding friction coefficient versus longitudinal slip curves are presented in Figure 7.6. Peak friction coefficients and the corresponding longitudinal slip values were extracted from Figure 7.6 and plotted against the tyre normal force, F_{Nd}, see Figures 7.7 and 7.8, respectively. The appropriate regression techniques were used in the respective figures and the following parameters were obtained for solid rubber tyres :

$P_0 = 0.827$

$P_1 = 0.0015$ [1/N]

$P_2 = -1e(-5)$ [1/N^2]

$R_0 = 8.6$

$R_1 = 0.028$ [1/N]

Knowing the above parameters for both P2 and S1, the theoretical studies requiring the tyre longitudinal slip from equation (3.3) can be performed.

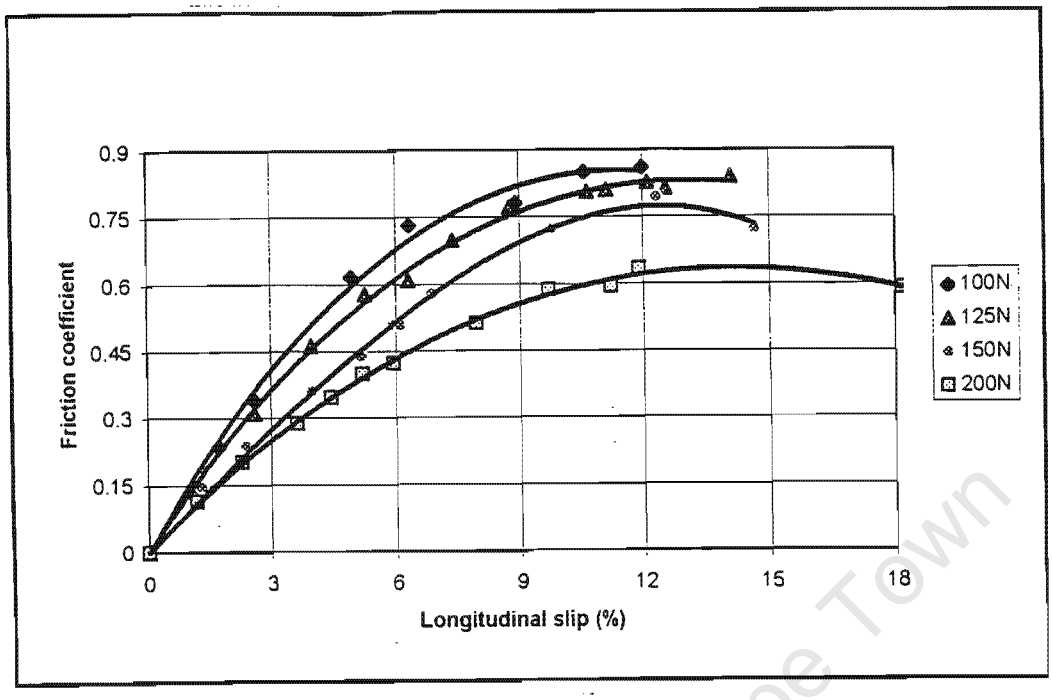

Figure 7.6 Friction coefficient versus longitudinal slip curves for tyre S1.

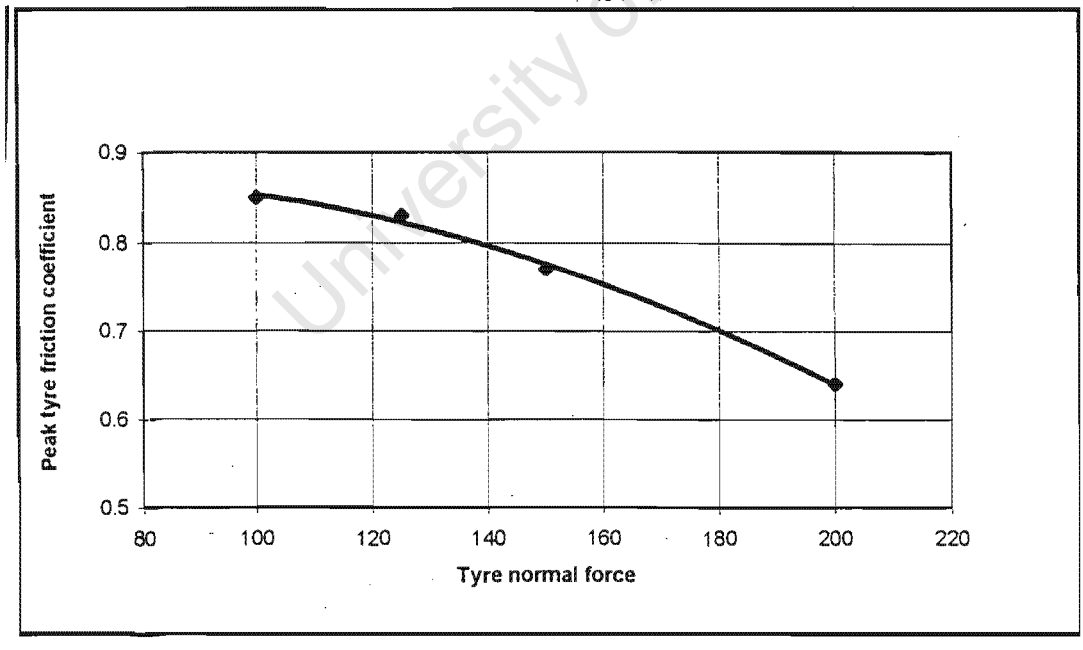

Figure 7.7 Peak friction coefficient versus the tyre normal force for tyre S1.

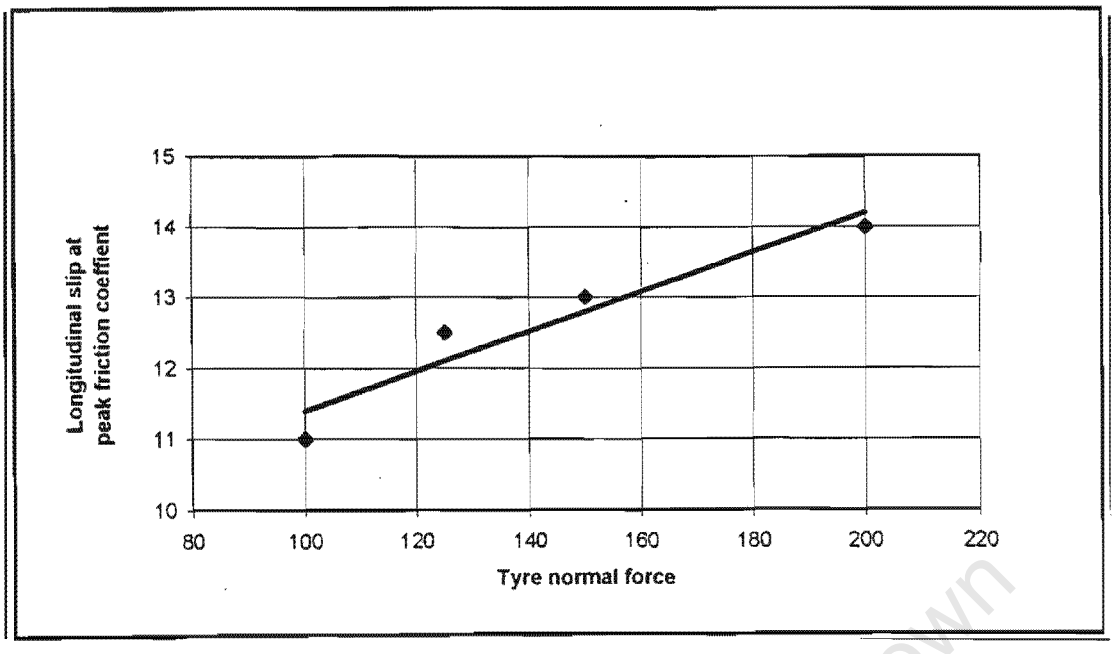

Figure 7.8 Longitudinal slip corresponding to the peak friction coefficient versus the tyre normal force.

7.3 THE PLANAR MODEL MILL PERFORMANCE

The model mill is operated in a similar manner as in section 7.2, i.e. the differential gearset is still operated as "locked" and the tyres are loaded equally for every test. Contrary to the previous section where the tyre parameters for a theoretical solution were sought, the model mill performance is under scrutiny in this section. The mill performance is characterised by the tyre tractive capabilities and power losses due to the tyres, the bearing and the rolling resistances. The attractive feature of this model is that when testing for tyre parameters, the planar model mill performance analysis can be performed by analysing the same data appropriately. Thus, the data used in section 7.2 is adopted in this section for further analysis, concentrating on the tyre traction and drive power losses.

7.3.1 TYRE TRACTIVE CAPABILITIES

Figure 7.9 presents Figures 7.3 and 7.6 plotted on the same set of axes. This has been done so that a comparative study of the two tyre types, P2 and S1, can be performed with ease. The curves corresponding to P2 are represented by thin trend-lines, whilst those corresponding to S1 are represented by thicker lines. This figure shows that for the same tyre normal force on both tyre types the pneumatic tyres develop a higher peak friction coefficient. Thus, pneumatic tyres in this study develop a higher peak tractive force than solid rubber tyres for a similar tyre normal force on both tyre types. The peak friction coefficient is also noticed to decrease with an increasing tyre normal force for both P2 and S1.

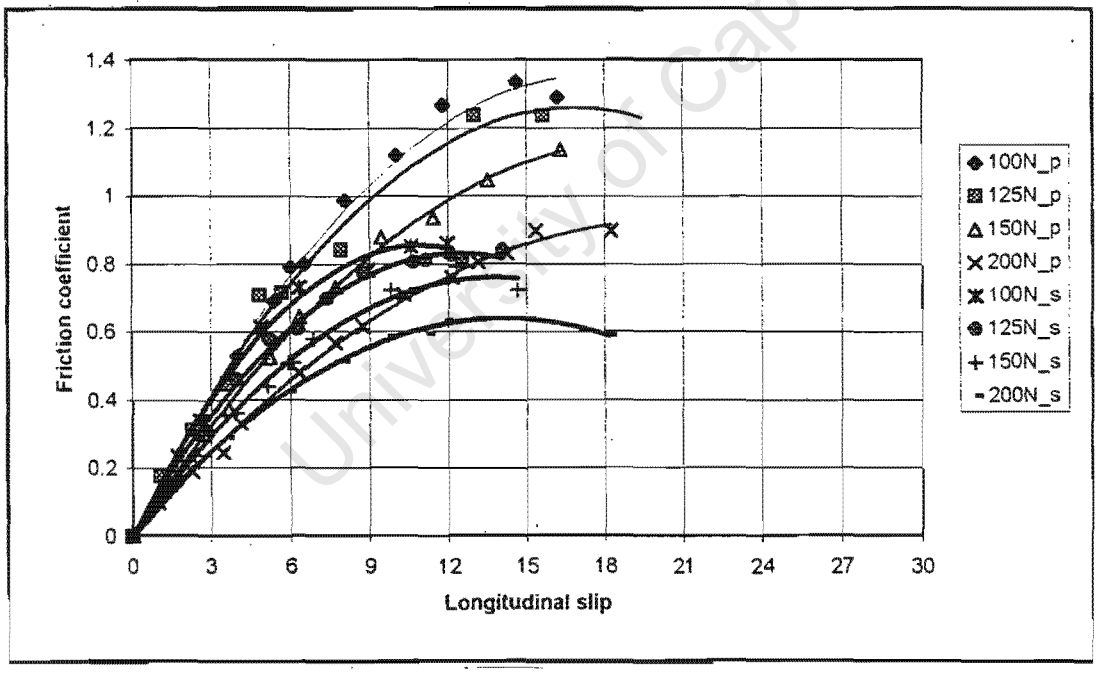

Figure 7.9 Tyre friction coefficient versus longitudinal slip for P2 and S1.

7.3.2 DRIVE POWER LOSSES ON THE MODEL MILL

The mill drive-system power losses occurring in the planar model, as outlined mathematically in section 5.3.1, were evaluated for both P2 and S1 and plotted against the input power to the differential gearset half-shafts. Figures 7.10 and 7.11 present these graphs for a tyre normal force of 100N for P2 and S2, respectively. The tyre slippage losses and the tyre rolling resistance plus support bearing losses were calculated by means of the first and second terms of equation (5.23), respectively.

The electric motor used to drive the model mill was a speed controller motor. This means that the electric motor controller kept the tyre speed constant. During all the tests conducted, the angular speed of the tyres dropped by about 2 to 5 rpm. Hence, as the brake torque was increased to absorb an increase of input power, the shell speed dropped. This implies that the magnitude of the drive longitudinal slip, equation (5.24), increased which automatically implies a higher drive traction force.

The power losses due to the bearing and tyre rolling resistances, P_R, decrease in a steady linear manner with an increasing longitudinal slip due to the dropping shell's angular speed, see equation (5.29). On the contrary, the power losses due to the tyre slippage, P_{ls}, increase non-linearly with an increasing tyre longitudinal slip. The overall power losses occurring on the mill increase in almost the same non-linear manner as the tyre slippage losses.

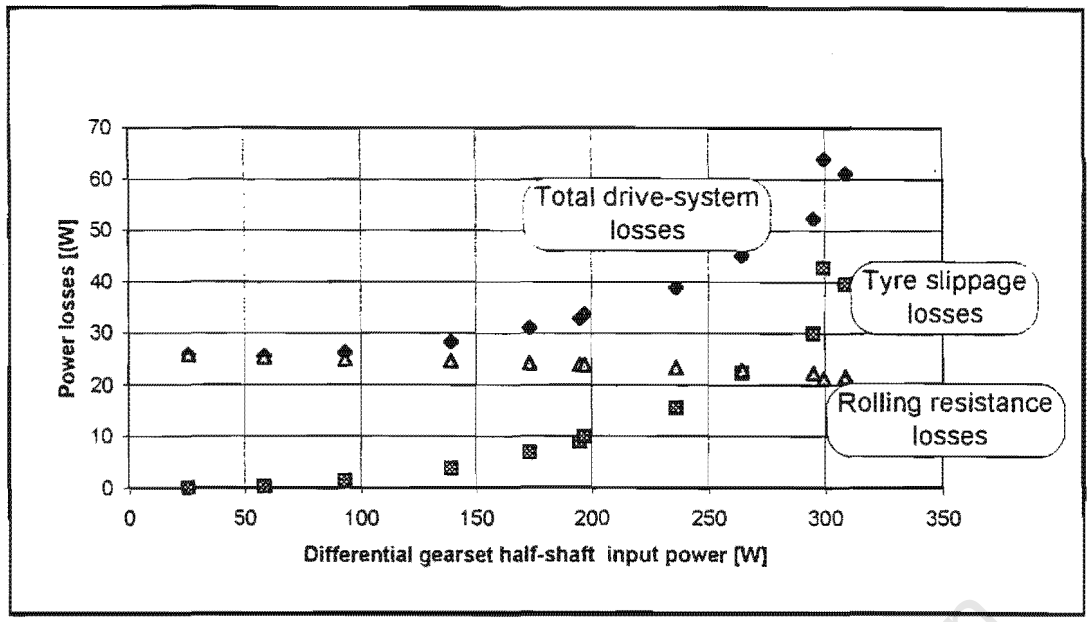

Figure 7.10 Model mill drive power losses for a normal force of 100N to P2.

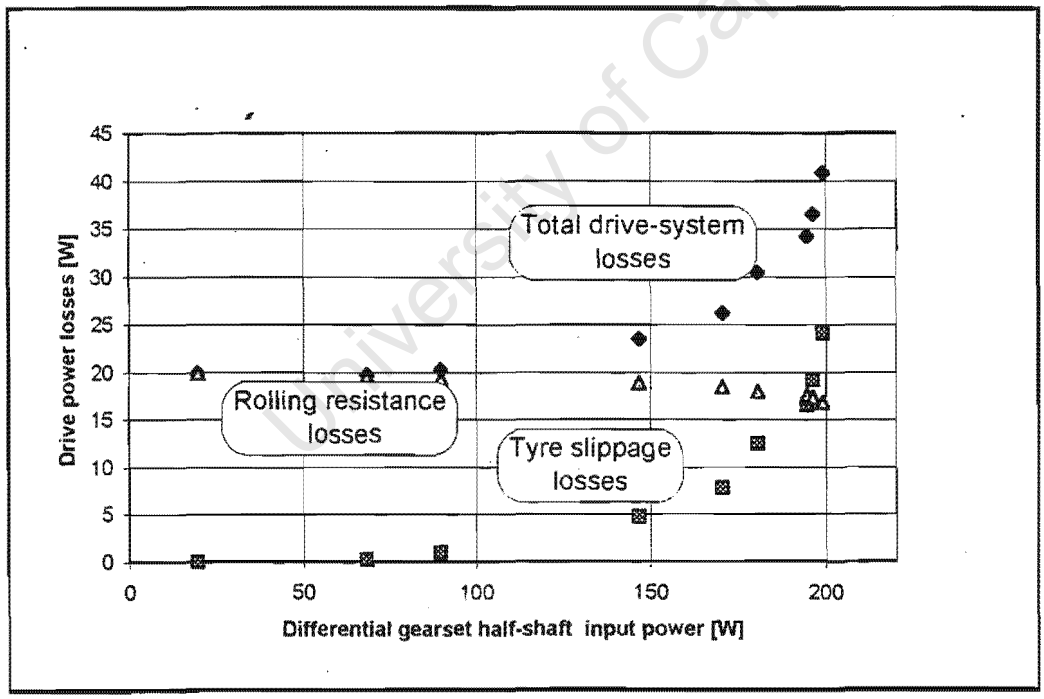

Figure 7.11 Model mill drive power losses for a normal force of 100N to S1.

The total drive power losses were also evaluated for the other tyre normal forces shown in Figure 7.9. The results of such analyses are presented in Figures E1 and E2 of Appendix E for P2 and S1, respectively. Curves in these figures show similar behaviours for the total drive-system power losses as in Figures 7.10 and 7.11. The maximum differential gearset half-shaft input power values, P_{dmax}, were recorded from curves in Figures E1 and E2 so as to compare the two tyre types. These values are plotted against the total shell normal force in Figure 7.12 for both tyre types.

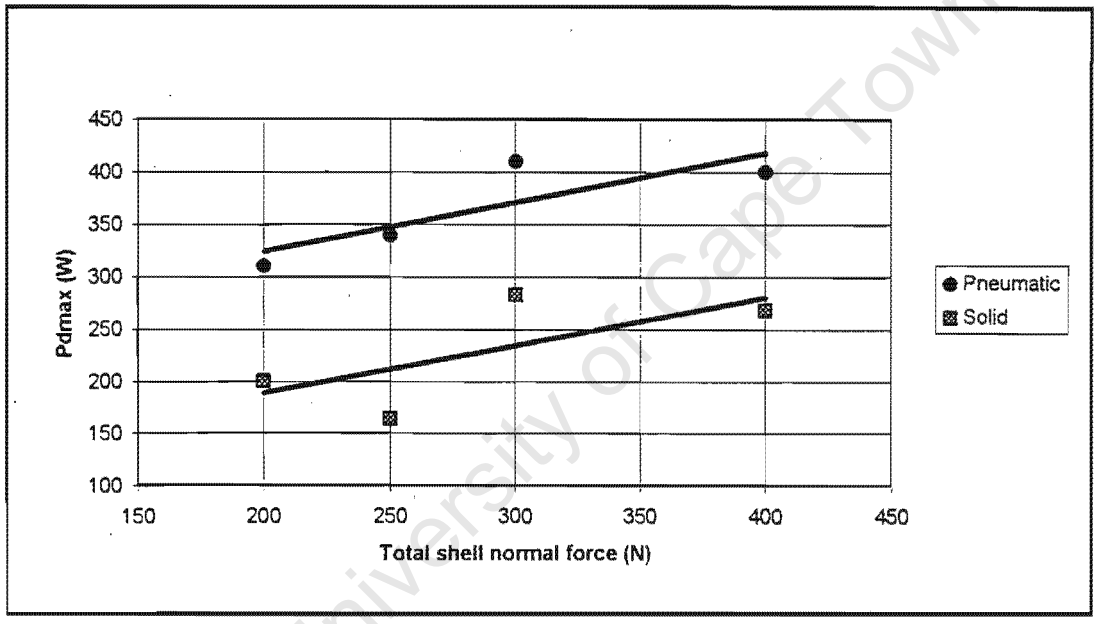

Figure 7.12 Maximum input power to the differential gearset half-shafts versus total shell normal force.

The two graphs in Figure 7.12 show that the maximum input power to the differential gearset half-shafts, P_{dmax}, increases in relation to the total shell normal force, F_{Ntot}, at an almost similar rate for the two tyre types. Note that the total shell normal force is twice the normal force acting

on each tyre. The maximum input power force acting on the shell is always higher for pneumatic tyres for all the values of F_{Ntot}. Thus, the pneumatic tyres in this study always transmit a higher amount of power to the shell than the solid rubber tyres.

The total power losses occurring on the model mill are of the same order of magnitude for both tyre types, but Figures E1 and E2 show that P_{lds}, at low values of input power, is slightly higher for the pneumatic tyres. Though the magnitude of the power losses occurring on the model mill are of great concern, another factor of major interest is the power transmission inefficiency of drive tyres (i.e. the ratio of total power losses and input power to the tyres). The mill drive power inefficiency is defined by :

$$Inefficiency(\%) = \frac{P_{lds}}{P_d} \cdot 100 \qquad (7.1)$$

The mill inefficiency was evaluated for the case of Figures 7.10 and 7.11 and plotted against longitudinal slip in Figure 7.13. Graphs of mill inefficiency versus the longitudinal slip for all the mill's loading cases are presented in Figures E3 and E4, Appendix E, for P2 and S1, respectively. Both tyre types exhibit similar trends regarding their inefficiencies, as shown in Figure 7.13. The 100 % mill inefficiency point corresponds to the case when the disc brake is disengaged with the purpose of determining tyres' effective rolling radii and power losses due to rolling and bearing resistances. Thus, all the differential gearset half-shaft input power to the model is utilised to overcome the rolling resistance.

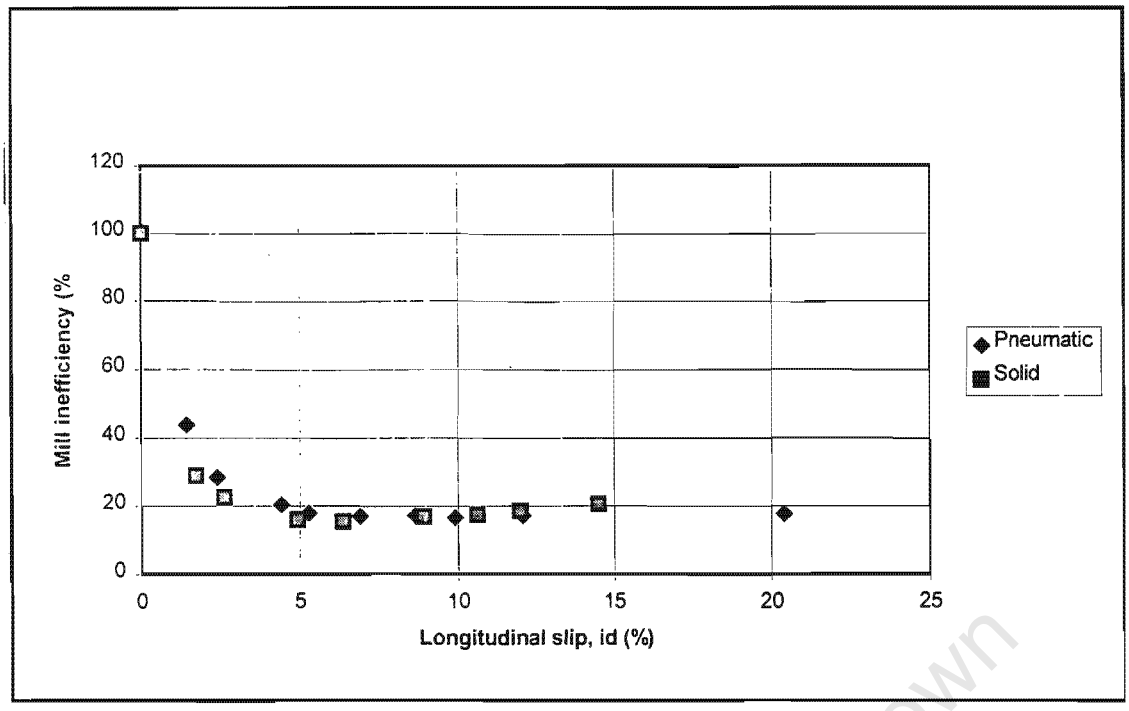

Figure 7.13 Mill inefficiency versus longitudinal slip for the tyres P2 and S1 (for F_{Nd} =100N).

The power loss percentage, or inefficiency, decreases from 100 % to just less than 20 % at a longitudinal slip of approximately 5 % for both tyres. Power losses in this range can be referred to as losses in the no-load situation in the prototype mill since resistance in the model mill is still minute. For longitudinal slip values of above 5 %, the model mill's drive power inefficiency increases almost in a linear fashion for both P2 and S1. Thus, the efficiency of the mill's drive system decreases as the charge mass of the mill increases.

7.4 DIMENSIONLESS TORQUE CAPABILITIES OF P2 AND S1

The experimental model mill has been designed by utilising dimensional analysis and similitude, refer to section 5.1. It was highlighted in that section that if the data from the experimental model is analysed in a dimensionless manner the inferences made would apply directly to the prototype

mill. Figure 7.14 presents a schematic diagram of the forces and moments acting on the shell. A torque balance about the shell's centreline results in equation (7.9) for a charge weight W and a charge centre of mass offset from the shell's longitudinal axis X_c.

$$\tau_s = W \cdot X_c \tag{7.2}$$

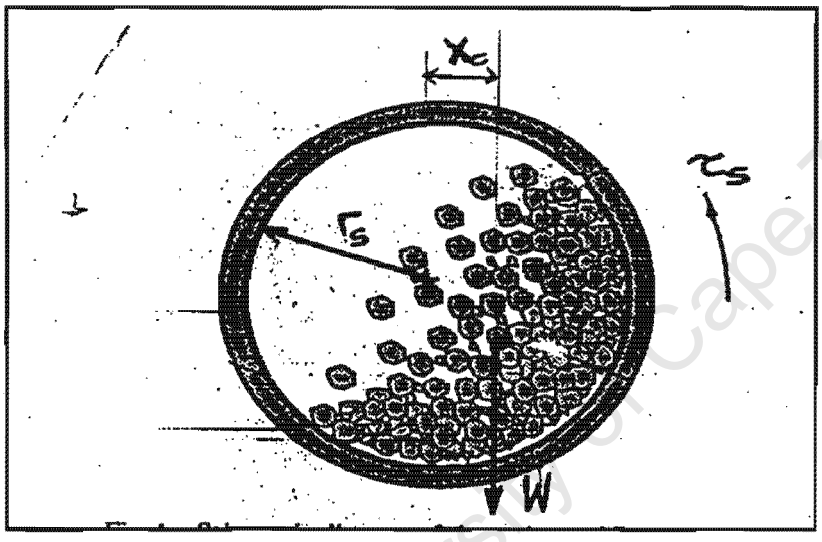

Figure 7.14 Forces and moments acting on a mill shell.

Rearranged, this equation results in :

$$\frac{\tau_s}{W \cdot r_s} = \frac{X_c}{r_s} \tag{7.3}$$

where

τ_s is the shell driving torque.

r_s is the shell radius.

In the case of the experimental model mill the weight of the charge is represented by the overall normal force acting on the shell, F_{Ntot} and the shell driving torque, τ_s, is similar to the brake torque, τ_b. Equation 7.11 is, thus, expressed as follows :

$$\frac{\tau_b}{F_{Ntot} \cdot r_s} = \frac{X_c}{r_s} \qquad (7.4)$$

The dimensionless quantity on the left-hand side of the above relationship can be easily evaluated for the experimental model mill at the maximum shell or brake torque. The significance of this dimensionless value is that it represents the torque capability of the tyres driving the shell. Thus, a zero value for this quantity means no grinding is effected as the centres of gravity for both the shell and the charge are coincident. A value of 1, then, corresponds to a case where the charge weight's centre of gravity lies on the circumference of the shell.

For a tyre that has been carefully selected to run a particular mill effectively and efficiently the above dimensionless quantity should be greater than zero and less than 1. The quantity X_c is not constant when an ore-grinding mill is operated. However, if a value higher than or slightly less than 1 is obtained this means that the tyres driving the shell are capable of driving an even bigger shell efficiently.

The load rating coefficient of a tyre, γ_N, is defined as :

$$\gamma_N = \frac{F_N}{F_{Nrated}} \tag{7.5}$$

where

F_N is the tyre normal force [N].

F_{Nrated} is the rated load carrying capability of a tyre[N].

Figure 7.15 presents the graphs of the dimensionless torque capability for tyres P2 and S1 plotted against the load rating coefficient. This figure shows that both tyres P2 and S1 exhibit a descending behaviour of the torque capability as the tyre load rating coefficient increases, even though some scatter in the data points for tyre S1 exists. The sensitivity of the torque carrying capacity to an increase in the tyre load is higher in the case of the pneumatic tyres than in solid rubber tyres.

Taking the liberty to extrapolate the linear curve fits to the data of Figure 7.15, suggests that at a load rating coefficient of approximately 0.41 both tyres could have the same torque carrying capability. Extrapolating the data even further, beyond the load rating coefficient of 0.41, S1 might have a higher torque carrying capability than P2. This study suggests that the solid rubber tyres might have better torque capabilities than pneumatic tyres at higher tyre normal forces.

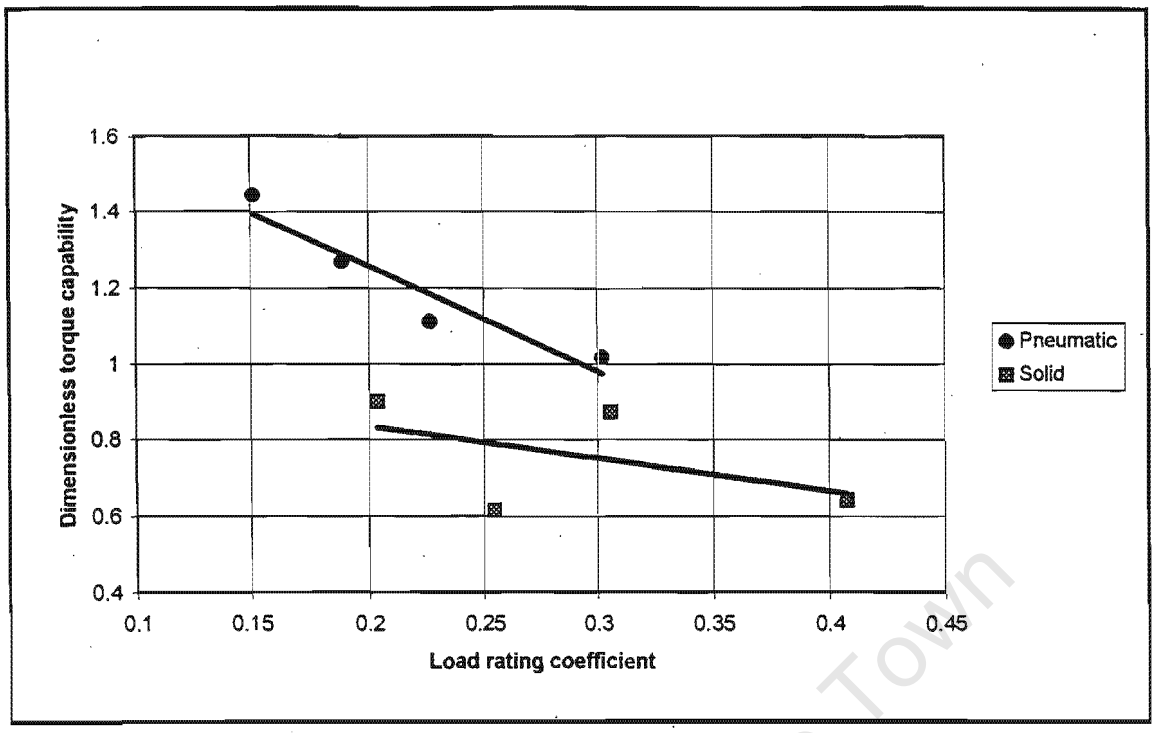

Figure 7.15 Dimensionless torque capabilities of P2 and S1.

CHAPTER 8. EXPERIMENTATION AND ANALYSIS OF THE 3-DIMENSIONAL (3D) MODEL

Due to the limited time available and enormous effort that had already been made through research, design, construction, calibration and testing stages it was later decided, in conjunction with the supervisor, that conducting an extensive 3D model analysis and a computer based theoretical study would far exceed the intended scope of the project. This chapter, therefore, contains limited experimental results performed on the 3D model. It was decided to carry out limited experimental work for the 3D model in cognisance of the fact that Mintek, the sponsors of the project, had expressed a particular interest in the non-planar application of the mill.

8.1 THE EXPERIMENTAL PROCEDURE

The differential gearset is operated as an open differential. This has an overall effect of imparting the same torque to both half-shafts. The 3D model represents a case when the centre of mass of the charge is offset longitudinally from the shell's centre of mass by a distance Y_c, see Figure 4.3. As outlined in section 5.2, this offset is simulated by applying unequal left- and right-hand tyre forces. The left- and right-hand tyre normal forces, F_{Ndl} and F_{Ndr}, are represented by the following relationships, respectively :

$$F_{Ndl} = F_1 + \Delta F \tag{8.1}$$

$$F_{Ndr} = F_1 - \Delta F \tag{8.2}$$

where

F_1 is the mean tyre normal force.

ΔF is the normal force offset from F_1 for both tyres.

The testing of the 3D model is such that once introduced, the values of F_1 and ΔF are held constant and tyre longitudinal slip is varied through the disc-brake sub-assembly, as was done in the planar model. Longitudinal slip is increased until the peak tractive force to the shell is generated. The overall differential gearset half-shaft torque is measured by the motor cantilever, shown as J in Figure 5.1. A physical difference between this model and the planar model is the different left- and right-hand tyre speeds.

In performing a thorough 3D model analysis F_1 should be held constant for several values of ΔF. This would, then, indicate how the mill responds to the differences in the individual tyre normal forces for the same total normal force acting on the shell, F_{Ntot}, where :

$$F_{Ntot} = F_{Ndl} + F_{Ndr} \tag{8.3}$$

or

$$F_{Ntot} = 2 \cdot F_1 \tag{8.4}$$

Once the mill performance for a particular F_{Ntot} has been established, F_1 is changed. As was done earlier on, ΔF is varied so as to get the mill's response for a new F_{Ntot}. This procedure has to be repeated for several values of F_1 and for both the pneumatic and solid rubber tyres. Varying F_1 will give the response of the mill to changes in the overall shell normal force, F_{Ntot}. A mathematical solution for the 3D model was presented in section 5.3.2.

It was outlined earlier in the introduction to this chapter that a thorough 3D model study will not be performed due to the stipulated constraints. During experimentation only two different values of F_1 and ΔF were used. Both the pneumatic, P2, and solid rubber, S1, tyres were tested under these conditions. Table 8.1 summarises the testing conditions for both tyre types.

Table 8.1 Testing conditions of both tyre types under 3D conditions.

F_1 [N]	F_{Ntot} [N]	ΔF [N]	F_{Ndl} [N]	F_{Ndr} [N]
200	400	25	225	175
200	400	50	250	150
150	300	25	175	125
150	300	50	200	100

8.2 EXPERIMENTATION AND ANALYSIS OF DATA

Relationships developed in section 5.3.2 which outline a mathematical procedure for the 3D model are utilised. Figures 8.1 and 8.2 present graphs of the mill inefficiency plotted against the overall input power to the differential gearset half-shafts for tyres S1 and P2, respectively, for all the loading conditions stipulated in Table 8.1. In these two graphs the quantity DF in the legends represents ΔF and F1 represents F_1. As in the planar model, an increasing differential half-shaft input power implies an increasing charge mass inside the mill shell.

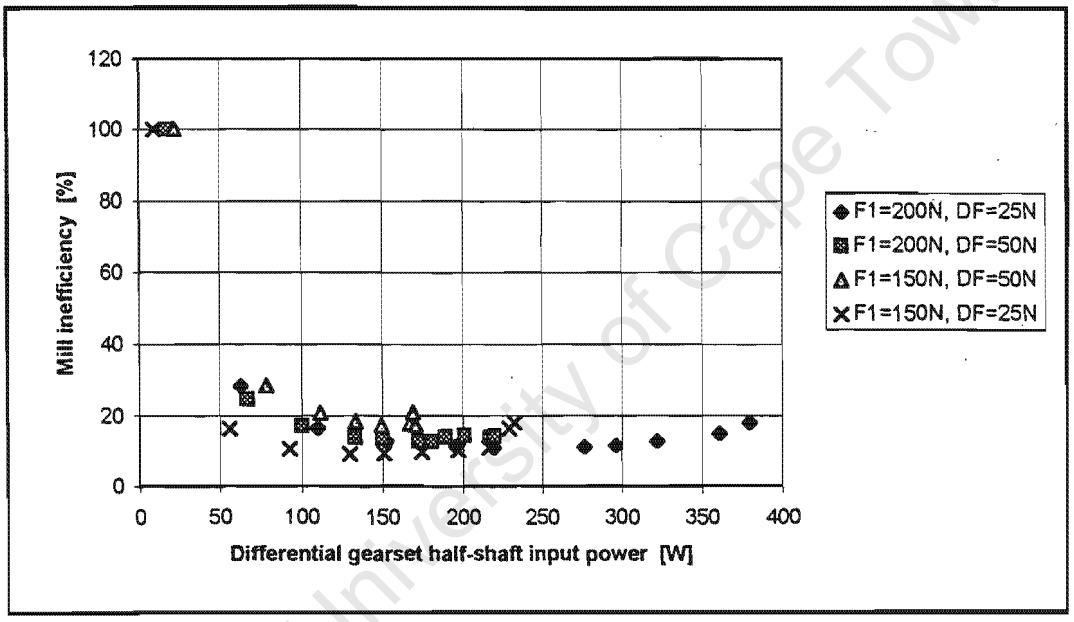

Figure 8.1 Mill inefficiency versus differential input half-shaft power for tyre S1.

Figure 8.1 shows that for the two cases when F_1= 200N the mill becomes more inefficient for a higher value of ΔF. This increase in inefficiency is noticeable at a value of approximately 200W for the differential gearset input power. The same trend is followed for the case of F_1 = 150N. A marked difference in the mill inefficiency due to the change in ΔF is shown in this case. The

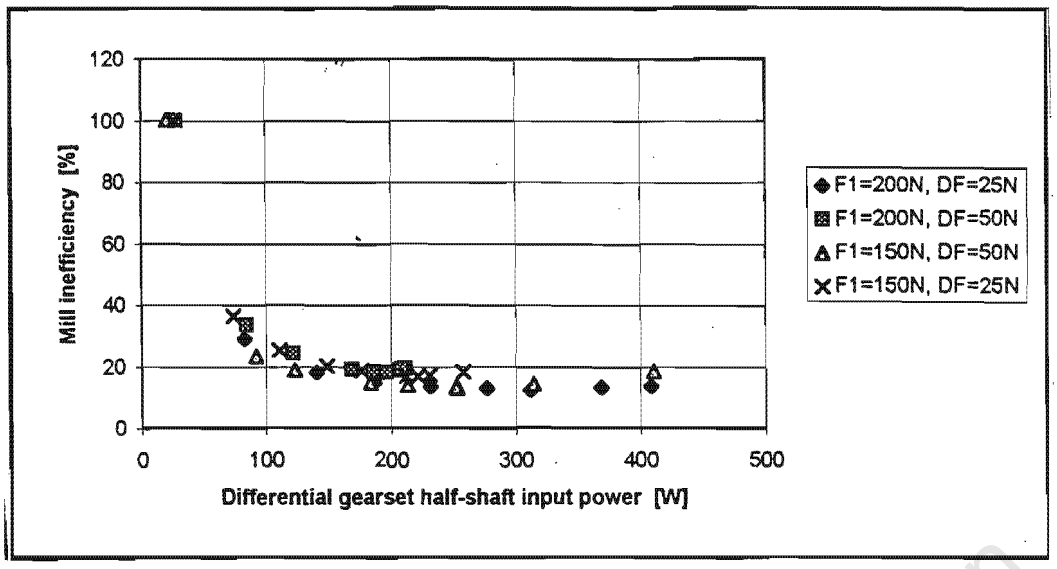

Figure 8.2 Mill inefficiency versus differential half-shaft input power for tyre P2.

comparison of Figures 8.1 and 8.2 indicates that the solid rubber tyres are more sensitive to ΔF than the pneumatic ones.

From Figure 8.1 it follows that for ΔF=50N the percentage losses occurring are higher in the case of a lower value F_l. For ΔF=25N the percentage losses are higher for the case of a higher value of F_l below P_d = 200W. Above this point percentage losses for F_l = 150N are higher than those of F_l = 200N, implying that for an increased shell resistance the mill inefficiency increases relatively with a decreasing value of F_l.

For pneumatic tyres, Figure 8.2, the percentage power losses are slightly higher for the bigger value of ΔF when F_l=200N. For F_l=150N percentage losses are higher for the lower value of ΔF. Thus, no particular trend was noticed in this study about the effect of ΔF in the case of pneumatic tyres. For ΔF=50N the percentage losses are higher for F_l=200N. However, for ΔF=25N percentage

losses are higher for F_l=150N. The influence of F_l in the case of pneumatic tyres also does not follow a particular trend for the above two loading cases.

From the above discussion it follows that firm conclusions about the mill performance under the 3D conditions cannot be made based on the comparison of the two data sets. Thus, more tests are needed. However, the above analyses show that the mill inefficiency is more sensitive to non-planar operation with small mill charges for a solid wheel than a pneumatic wheel drive system.

CHAPTER 9. CALIBRATION OF THE PROTOTYPE MILL

This chapter outlines a recommended procedure for obtaining the mill drive power and the drive power losses. This procedure assumes that some parameters, which will be highlighted during the discussions in the subsequent sub-sections, are measurable. Sections 9.1, 9.2, 9.3 and 9.4 outline the procedures for obtaining the charge mass, the overall tyre tractive force, the total rolling resistance and the power requirements of the mill.

9.1 DETERMINATION OF THE CHARGE MASS

The mill driver and idler axles are mounted on top of four load-cells. The two load-cells on each axle are positioned on either side of the differential gearsets. These load-cells are, thus, designated similarly to the tyres they are positioned next to, e.g. the vertical force on the load cell near the left-hand drive tyre is designated F_{Vdl}. The total load-cell readings for an empty stationary mill is given by the following equation:

$$F_{V0} = [F_{Vdl} + F_{Vdr} + F_{Vil} + F_{Vir}]_0 \tag{9.1}$$

For a filled mill, stationary or rotating, the total load cell reading is given by equation (9.2).

$$F_V = F_{Vdl} + F_{Vdr} + F_{Vil} + F_{Vir} \tag{9.2}$$

where

$F_{Vdl,r}$ is the left or right hand load cell reading for the driver axle.

$F_{Vil,r}$ is the left or right hand load cell reading for the idler axle.

For a filled rotating mill the value of F_V comprises the weights of the empty mill and the charge mass. Careful consideration of the actual construction of the prototype mill, as well as proper definition of the control volume reveal that the pinion force will not be transferred to the load cells. The charge mass, m_c is then obtained by utilising the following equation :

$$F_V = F_{V0} + m_c \cdot g \tag{9.3}$$

or, after rearranging,

$$m_c = \frac{F_V - F_{V0}}{g} \tag{9.4}$$

where g is the gravitational acceleration.

9.2 DETERMINATION OF THE OVERALL TYRE TRACTIVE FORCE

It is possible to measure the input torque to the differential gearset on the driver axle, τ_d, through the strain gauges mounted on the input shaft. For one to be able to determine the drive differential half-shaft torques the differential speed ratio, N_f, and efficiency, η, are required. The former can easily be obtained, e.g. from the engineering drawings, whilst the latter is unknown and would need separate tests, as outlined in section 4.3, to be carried out. However, if these two variables are known, the sum of the torques of the two half-shafts, τ_{dl} and τ_{dr}, is represented by the following equation,

$$\tau_{dl} + \tau_{dr} = \eta \cdot N_f \cdot \tau_d \tag{9.5}$$

with

$N_f > 1$

$$\tau_{dl} = F_{Xl} \cdot r_{dl} \tag{9.6}$$

$$\tau_{dr} = F_{Xr} \cdot r_{dr} \tag{9.7}$$

$r_{dl,r}$ being the measured left or right hand tyre loaded radii.

But, since the drive differential gearset is operated as an open differential, the input torque to each half-shaft is given by :

$$\tau_{dl} = \tau_{dr} = \frac{\eta \cdot N_f \cdot \tau_d}{2} \tag{9.8}$$

$$\Rightarrow F_{Xl} = \frac{\eta \cdot N_f \cdot \tau_d}{2 \cdot r_{dl}} \tag{9.9}$$

$$\Rightarrow F_{Xr} = \frac{\eta \cdot N_f \cdot \tau_d}{2 \cdot r_{dr}} \tag{9.10}$$

Define the overall tyre tractive force, F_X, as follows :

$$F_X = F_{Xl} + F_{Xr} \tag{9.11}$$

$$\Rightarrow F_X = \frac{\eta \cdot N_f \cdot \tau_d}{2} \cdot \left(\frac{1}{r_{dl}} + \frac{1}{r_{dr}}\right) \tag{9.12}$$

Another alternative would be to measure the half-shaft torques, τ_{dl} and τ_{dr}, on the appropriate shafts directly. This would mean cutting some sections on the axle which encloses the drive differential output half-shafts and mounting strain gauges in the same way as was done in the drive differential input shaft. These slots would also have to enable the measurement of the angular speeds on these shafts. If this could be done there would be no need of obtaining the differential gearset efficiency and speed ratio as the torque is measured at the differential's output, thus bypassing the differential inefficiency.

9.3 DETERMINATION OF THE TYRE ROLLING RESISTANCE

Rolling resistance was highlighted in chapter 3.3 as one of the important mechanisms by which tyres dissipate power. In analysing the tyre power losses in chapters 7 and 8, the rolling resistance power losses, contrary to tyre slippage losses, showed a very slow change with a changing relative speed between the shell and the tyres (e.g. see Figures 7.10 and 7.11).

Figure 4.1 showed the forces acting on a mill shell for the planar model. For an empty shell it is assumed that all tyres on an axle are loaded equally. With this assumption the following relationships apply :

$$t_d = t_{dl} = t_{dr} \tag{9.13}$$

$$F_{X0} = F_{Xl0} + F_{Xr0} \tag{9.14}$$

$$\frac{F_{Rd0}}{2} = F_{Rdl0} = F_{Rdr0} \tag{9.15}$$

$$\frac{F_{Ri0}}{2} = F_{Ril0} = F_{Rir0} \tag{9.16}$$

$$F_{Ndl0} = F_{Ndr0} = \frac{F_{Rd0}}{2} \cdot \frac{r_d}{t_d} \tag{9.17}$$

$$F_{Nil0} = F_{Nir0} = \frac{F_{Ri0}}{2} \cdot \frac{r_i}{t_i} \tag{9.18}$$

In order to obtain the overall rolling resistance, F_R, a torque balance of an empty rotating shell must be done as follows :

$$[(F_{Xl0} - F_{Rdl0}) + (F_{Xr0} - F_{Rdr0}) - F_{Ril0} - F_{Rir0}] \cdot r_s - F_{Ndl0} \cdot t_{dl} - F_{Ndr0} \cdot t_{dr} - F_{Nil0} \cdot t_{il} - F_{Nir0} \cdot t_{ir} = 0 \tag{9.19}$$

where

r_s is the shell radius.

$F_{Rdl,r0}$ is the left or right hand driver tyre rolling resistance.

$F_{Ril,r0}$ is the left or right hand idler tyre rolling resistance.

$F_{Xl,r0}$ is the tractive force of an empty mill due to the left or right hand tyres.

$F_{Ndl,r0}$ is the left- or right-hand normal force of the driver tyre sub-assembly.

$F_{Nil,r0}$ is the left- or right-hand normal force of the idler tyre sub-assembly.

$t_{dl,r}$ is the pneumatic trail of the left- or right-hand driver tyres.

$t_{il,r}$ is the pneumatic trail of the left- or right-hand idler tyres.

After introducing the conditions in equations (9.13)-(9.18) the above relationship becomes,

$$F_{X0} \cdot r_s = F_{Rd0} \cdot (r_s + r_d) + F_{Ri0} \cdot (r_s + r_i) \tag{9.20}$$

or

$$F_{X0} = F_{Rd0} \cdot (1 + \frac{r_d}{r_s}) + F_{Ri0} \cdot (1 + \frac{r_i}{r_s}) \tag{9.21}$$

The conditions stipulated in equations (9.15) through (9.20) may be different when the mill is loaded and rotating. This will then result in different values for the loaded radii of the driver and idler tyre sets. However, excessive tyre deflections are not desirable as this would lead to an increased tyre operating temperature, and ultimately wear the tyre rapidly. Thus, although all these tyre sets may be subjected to different normal forces an assumption is made that the tyre loaded radii which appear in equation (9.22) are approximately equal. This results in the following relationship :

$$F_{X0} = \alpha \cdot (F_{Rd0} + F_{Ri0}) \tag{9.22}$$

or

$$F_{R0} = \frac{F_{X0}}{\alpha} \tag{9.23}$$

where

$$\alpha = 1 + \frac{r_{av}}{r_s} \tag{9.24}$$

r_{av} is the average of all the tyre loaded radii.

F_{R0} is the sum of F_{Rd0} and F_{Ri0}.

The rolling resistance coefficient, f_r, defined in section 3.3, is given in this case by the following equation :

$$f_r = \frac{F_{R0}}{m_s \cdot g} \tag{9.25}$$

where

m_s is the mass of the empty shell and whel assembly.

g is the gravitational acceleration.

For a filled mill, the sum of all existing rolling resistances, F_R, is given by :

$$F_R = f_r \cdot (m_c + m_s) \cdot g \tag{9.26}$$

where

m_c is the charge mass.

In summary, the procedure of obtaining the rolling resistance is as follows :

- For an empty mill, the tyre tractive force is obtained by means of equation (9.12).
- The rolling resistance coefficient for an empty mill is obtained by equation (9.25).
- For a filled mill, the rolling resistance is obtained by means of equation (9.26).

Note that the value of f_r obtained through equation (9.26) is for the case when all the tyres are loaded equally. The rolling resistance coefficient may vary when the charge centre of mass is offset longitudinally from the shell's centre of mass by a distance Y_c.

9.4 POWER REQUIREMENTS OF THE MILL

To obtain the power imparted to a loaded, rotating mill one needs to first evaluate the *overall* tyre tractive force, F_X, through equation (9.12) in section 9.2. The *overall* rolling resistance, F_R, obtained through the use of equation (9.27), must also be evaluated. The following equation gives a relationship for the power imparted by the tyres to the shell (see Figure 4.1),

$$P_{ds} = (F_X - F_R) \cdot r_s \cdot \omega_s - F_N \cdot t_{av} \cdot \omega_s \tag{9.27}$$

where

ω_s is the angular speed of the shell.

t_{av} is the average pneumatic trail for all the all eight tyres.

But

$$F_N = F_R \cdot \frac{r_{av}}{t_{av}} \tag{9.28}$$

$$\therefore P_{ds} = [F_X - F_R \cdot (1 + \frac{r_{av}}{r_s})] \cdot r_s \cdot \omega_s \tag{9.29}$$

The power available in the differential input shaft , P_d, and on the two half-shafts, P_{dl} and P_{dr}, are given by equations (9.30), (9.31) and (9.32), respectively.

$$P_d = \tau_d \cdot \omega_d \tag{9.30}$$

$$P_{dl} = \tau_{dl} \cdot \omega_{dl} \tag{9.31}$$

$$P_{dr} = \tau_{dr} \cdot \omega_{dr} \tag{9.32}$$

where ω_d is the measured angular speed of the input shaft to the differential gearset.

$\omega_{dl,r}$ is the measured angular speed of the left- or right-hand differential output half-shafts.

With the help of equations (9.8), (9.12) and (9.29) the power transferred from the tyres to the shell may be re-written as :

$$P_{ds} = [\frac{\eta \cdot N_f \cdot \tau_d}{r'_{av}} - f_R \cdot (m_c + m_s) \cdot g \cdot (1 + \frac{r_{av}}{r_s})] \cdot r_s \cdot \omega_s \qquad (9.33)$$

The total power lost in the system, P_{lds}, may be evaluated by the following relationship :

$$P_{lds} = P_d - P_{ds} \qquad (9.34)$$

Contrary to the experimental model mill case, the total power losses on the system are due to both the tyres and the *differential* gearset inefficiency in this case. However, the differential gearset inefficiency may be bypassed by measuring the torque on the differential gearset output half-shafts directly, as highlighted in section 9.2.

CHAPTER 10. CONCLUSIONS

A laboratory apparatus which allows the investigation of the performance of rubber wheels as a traction mechanism for mill shells was successfully developed. This apparatus allows the effects of a variety of parameters to be studied, e.g. those due to the mill charge size, its centre of mass position and the wheel type. The following inferences, based on the measurements which were conducted on the laboratory apparatus, are made :

- ***THE TYRE PARAMETERS FOR THE THEORETICAL MODEL MILL ANALYSIS***

The pneumatic tyres, P2, and solid rubber tyres, S1, were tested for the empirical parameters P_0, P_1,P_2, R_0 and R_1 needed by the LVDS tyre model. This tyre model enables the prediction of the tyre longitudinal slip ratio for a known tyre-shell friction coefficient. Thus, a computer based mathematical model mill response can be performed for both tyre types.

- ***LOSSES ON THE TYRE DRIVE SYSTEMS***

Power losses of the mill drive system depend on the charge mass. Expressed as a percentage of the input power, the %-losses may vary from 100% (for zero charge mass) to a minimum of about 10% (see Figures E3 and E4). This minimum occurs at a tyre longitudinal slip of about 5%. Hence, for a given shell size and mass, the optimum drive tyre size would be such that the tyres operate at about 5% longitudinal slip.

- ***PNEUMATIC TYRES VERSUS SOLID RUBBER TYRES***

From the results obtained in this study as regards the pneumatic and solid rubber tyres, it was observed that :

1. Pneumatic tyres can generate a higher peak friction coefficient than solid rubber tyres under similar loading conditions.
2. Solid rubber tyres have lower rolling resistance losses than pneumatic tyres, see Figures 7.10 and 7.11.
3. For a specific pneumatic and solid rubber tyre size, and for mill charges which are substantially less than the pro-rata rated tyre loads, a pneumatic tyre can transmit a higher mill torque than a solid rubber tyre.
4. Pneumatic tyres show a more sensitive decrease in the torque capability with an increasing mill charge than the solid rubber tyres. Thus, there might exist a point where the torque capabilities of the both tyre types is the same, after-which the solid rubber tyres may have a better torque capability, see Figure 7.15.

- ***THE INFLUENCE OF Y_c***

The charge centre of mass longitudinal offset from the shell's centre of mass, Y_c, has been simulated by applying unequal tyre normal forces through the push-rods H1 and H2, and by using an open differential gearset. The effect of the difference in both the individual tyre normal forces and the overall shell normal force has brought about changes in the mill's response, as regards percentage power losses. The comparison of Figures 8.1 and 8.2 suggests that, for

smaller mill charges the performance of the solid rubber tyres is more sensitive to the off-centre charge mass position, Y_c, than that of the pneumatic tyres.

- ***PROTOTYPE MILL CALIBRATION***

Relationships to be used in determining the prototype mill power requirements are given. These relationships can be utilised successfully as most of the required empirical parameters are measurable. However, in evaluating the torque in the drive differential half-shafts, either the differential efficiency and speed ratio are required or the axles enclosing the drive wheel half-shafts have to be cut at the appropriate positions so as to enable wheel drive torque measurement through the strain gauges directly.

CHAPTER 11. RECOMMENDATIONS

More 3D tests should be carried out on the model mill so as to firmly establish the trends followed by the mill inefficiency for the various charge mass sizes and off-centre positions of the charge mass-centre. A theoretical model mill analysis utilising the LVDS tyre model should be carried out for both the planar and 3D models. The output of these theoretical studies should be compared with the empirical results.

The prototype mill power losses should be obtained empirically by using the outlined calibration procedure. A numerical calculation should be performed and compared with the empirical results. The tyre parameters required by the LVDS tyre model for the prototype mill should be obtained from the tyre manufacturers, Michelin. It is only after the theoretical results compare with the empirical results to the required degree of accuracy that the theoretical solution can be utilised alone in predicting the mill drive power losses. An operational instrumentation and software system should be developed which will allow the power draw performance of the mill to be monitored on site in a user-friendly manner.

REFERENCES

[1] M. N. Brodie, John Chapman

"Selection of motors, drive-trains and electrical circuitry for comminution circuits", pages 646 to 666.

[2] H. C. C. Kartman

"Development of grinding mills and future trends", The South African Mechanical Engineer, South Africa, April 1972, pages 135 to 139.

[3] S. Morrell

"Prediction of grinding mill power", The Institution of Mining and Metallurgy, United Kingdom, 1992, pages C25 to C31.

[4] Thomas D. Gillespie

"Tires", Fundamentals of Vehicle Dynamics, United States of America, 1992, pages 335 to 375.

[5] Colin Campbell

"Tyres and wheels", Design of racing sports cars, London, 1973, pages 26 to 40.

[6] Norman L. Weiss

"Tumbling mill characteristics, Ball mills, Rod mills, Autogenous mill", SME Mineral Processing Handbook (Volume 1), New York, 1985, pages 3C-3 to 3C-102.

[7] S. Morrell

"Power draw of wet tumbling mills and its relationship to charge dynamics", The Institution of Mining and Metallurgy, United Kingdom, 1996, pages C43 to C62.

[8] J. R. Ellis

"The pneumatic tyre", Vehicle Handling Dynamics, London, 1994, pages 1 to 37.

[9] J. Venter

"Tyre Maintenance", The Car (Volume 41 No. 8), South Africa, September 1997, pages 165 to 170.

[10] R. T. F. Plaut

"Factors governing the choice of tyres for mechanical handling equipment", Tyres for Mechanical Handling Equipment, London, 21 May 1974, pages 1 to 8.

[11] J. Venter

"Buying tyres" - Part II, The Car (Volume 41 No. 9), South Africa, October 1997, pages 183 to 188.

[12] Hans B. Pacejka, Egbert Bakker, Lans Nyborg

"Tyre modelling for use in vehicle dynamics studies", SAE Technical paper (Series 870421), Michigan, February 1987, pages 1 to 15.

[13] A. Andrzej, G. Nalecz and Associates

"LVDS Tire model", Vehicle Dynamics international (Series 13091), Place, 1990, pages 6.10 to 9.19.

[14] C. Redelinghuys

"A dynamic model for the analysis of a tyre-mounted grinding mill", University of Cape Town Mechanical Engineering report, January 1995, pages 1 to 30.

[15] U. J. Detering

"Design of an ore mill model to determine tyre losses", University of Cape Town Mechanical Engineering Final Year Project, November 1995, pages 1 to 52.

[16] D. K. Gilbert

"Design, analysis and testing of a model differential gearset", University of Cape Town Mechanical Engineering Final Year Project, November 1995, pages 1 to 67.

[17] H. E. Merritt

"Lubrication and cooling", Gear Engineering, Great Britain, 1971, pages 334 to 344.

[18] J. F. Douglas, J. M. Gasiorek, J. A. Swaffield

"Dimensional analysis and similarity", Fluid mechanics (Second Edition), New York, 1991, pages 689 to 726.

[19] J. P. Holman, W. J. Gajda Jr.

"Calibration", Experimental Methods for Engineers, Singapore, 1989, pages 7 to 8.

BIBLIOGRAPHY

J.E. Shigley

Mechanical Engineering Design, 4th Edition, Singapore, 1986.

V.R. Hamilton, R.V. Setterfield

The Elements of Advanced Machine Design, Durban, 1991.

B. J. Anslow, E. L. Marrilow

Agricultural and Allied Industrial Tractors, Proceedings of The Institution of Mechanical Engineers, Vol 184, Part 3Q, 1969.

C. Campbell

The Sports Car, London, 1978.

I. Miller, J. E. Freund, R. A. Johnson

The Probability and Statistics for Engineers, Fourth Edition, New Jersey, 1990.

APPENDIX A - A THEORETICAL SOLUTION FOR THE PLANAR MODEL [14].

• TORQUE BALANCE OF THE SHELL

Refer to Figure 4.1,

$$(F_X - (F_{Rd} + F_{Ri})) \cdot r_s - F_{Nd} \cdot t_d - F_{Ni} \cdot t_i - m_c \cdot g \cdot X_c = 0 \qquad \text{(A1)}$$

F_{Rd} and F_{Ri} were defined as follows,

$$F_{Rd} = \frac{F_{Nd} \cdot t_d}{r_d} \qquad \text{(A2)}$$

and

$$F_{Ri} = \frac{F_{Ni} \cdot t_i}{r_i} \qquad \text{(A3)}$$

$$\Rightarrow F_X = \frac{m_c \cdot g \cdot X_c}{r_s} + F_{Nd} \cdot t_d \cdot (\frac{1}{r_s} + \frac{1}{r_d}) + F_{Ni} \cdot t_i \cdot (\frac{1}{r_s} + \frac{1}{r_i}) \qquad \text{(A4)}$$

• VERTICAL FORCE BALANCE

$$(m_c + m_s) \cdot g - (F_X - F_{Rd}) \cdot \sin\phi_d - F_{Nd} \cos\phi_d - F_{Ri} \cdot \sin\phi_i - F_{Ni} \cdot \cos\phi_i = 0 \qquad \text{(A5)}$$

Substituting equations (A2), (A3) and (A4) in equation (A5) results in,

$$A \cdot F_{Nd} + B \cdot F_{N_i} = E \tag{A6}$$

where

$$A = \cos\phi_d + \frac{t_d \cdot \sin\phi_d}{r_s} \tag{A7}$$

$$B = t_i \cdot (\frac{1}{r_i} + \frac{1}{r_s}) \cdot \sin\phi_d + \frac{t_i}{r_i} \cdot \sin\phi_i + \cos\phi_i \tag{A8}$$

$$E = (m_c + m_s) \cdot g - \frac{m_c \cdot g \cdot X_c \cdot \sin\phi_d}{r_s} \tag{A9}$$

- **HORIZONTAL FORCE BALANCE**

$$(F_X - F_{Rd}) \cdot \cos\phi_d - F_{Nd} \cdot \sin\phi_d + F_{N_i} \cdot \sin\phi_i - F_{Ri} \cdot \cos\phi_i = 0 \tag{A10}$$

Substituting again equations (A2), (A3) and (A4) into equation (A10) gives the following :

$$C \cdot F_{Nd} + D \cdot F_{Ni} = F \tag{A11}$$

where

$$C = \frac{t_d \cdot \cos\phi_d}{r_s} - \sin\phi_d \tag{A12}$$

$$D = t_i \cdot (\frac{1}{r_i} + \frac{1}{r_s}) \cdot \cos\phi_d - \frac{t_i \cdot \cos\phi_i}{r_i} + \sin\phi_i \tag{A13}$$

$$F = -\frac{m_c \cdot g \cdot X_c \cdot \cos\phi_d}{r_s} \tag{A14}$$

Model tyre radii as follows :

$$r_d = r_{d0} - F_{Nd} \cdot k_{zd} \tag{A15}$$

$$r_i = r_{i0} - F_{N_i} \cdot k_{zi} \tag{A16}$$

Then solve equations (A6) and (11) simultaneously in an iterative manner.

• TYRE FRICTIONAL CHARACTERISTICS

By solving equations (A6) and (A11) together with (A15) and A(16) the tyre tractive force, F_X, and normal forces, F_{Nd} and F_{Ni}, are known. Friction coefficient, μ_X, for drive tyres is defined as follows :

$$\mu_X = \frac{F_X}{F_{Nd}} \tag{A17}$$

The solution procedure entails determination of F_X and F_{nd}, where-after μ_X is known. The longitudinal slip in equation (3.3) is to be solved numerically.

• ROLLING RESISTANCE

The rolling resistance coefficient is defined by the following ratio,

$$f_r = \frac{F_R}{F_{Nd}} \tag{A18}$$

Use

$$f_r = 0.0041 + 0.000041 \cdot \omega_s \cdot r_s \tag{A19}$$

From equations (A2) and (A3) it follows that normal force offset distances are given by :

$$t_d = f_r \cdot r_d \tag{A20}$$

$$t_i = f_r \cdot r_i \tag{A21}$$

- **ENERGY BALANCE**

Power supplied to the differential gearset drive shaft, P_d :

$$P_d = P_t + P_f \tag{A22}$$

where

P_t is the total half-shaft power.

$$P_t = P_d \cdot \eta \tag{A23}$$

and P_f is the power loss due to the differential gearset inefficiency.

$$P_f = (1 - \eta) \cdot P_d \tag{A24}$$

Power transferred from the drive tyres to the shell, P_{ds} , see Figure 4.1:

$$P_{ds} = [(F_X - F_{Rd}) - F_{Nd} \cdot \frac{t_d}{r_s}] \cdot r_s \cdot \omega_s \tag{A25}$$

Hence, using equation (A2) :

$$P_{ds} = \omega_s \cdot [F_X \cdot r_s - F_{Nd} \cdot t_d \cdot (1 + \frac{r_s}{r_d})] \tag{A26}$$

Note that the total half-shaft power is also defined as follows,

$$P_t = F_X \cdot r_d \cdot \omega_d \tag{A27}$$

Power lost between the shell and the idle tyres, P_{lsi} :

$$P_{lsi} = (F_{Ri} + F_{Ni} \cdot \frac{t_i}{r_s}) \cdot r_s \cdot \omega_s \tag{A28}$$

Thus, total power lost, P_{lds} :

$$P_{lds} = P_t + P_f - P_{ds} - P_{lsi} \tag{A29}$$

$$\therefore P_{lds} = F_X \cdot r_d \cdot \omega_d + (1 - \eta) \cdot P_d - F_X \cdot r_s \cdot \omega_s + F_{Nd} \cdot t_d \cdot (1 + \frac{r_s}{r_d}) \cdot \omega_s + F_{Ni} \cdot t_i \cdot (1 + \frac{r_s}{r_i}) \cdot \omega_s \tag{A30}$$

Define the tyre longitudinal slip, i_d, as follows :

$$i_d = \frac{r_s \cdot \omega_s}{r_d \cdot \omega_d} - 1 \tag{A31}$$

After rearranging equation (A30) the following result is obtained :

$$P_{lds} = -P_t \cdot i_d \cdot \eta + F_{Nd} \cdot t_d \cdot (1 + \frac{r_s}{r_d}) \cdot \omega_s + F_{Ni} \cdot t_i \cdot (1 + \frac{r_s}{r_i}) \cdot \omega_s + (1 - \eta) \cdot P_d \quad \text{(A32)}$$

Thus,

$$P_{lds} = P_{ls} + P_{Rd} + P_{Ri} + P_f \quad \text{(A33)}$$

where

$$P_{ls} = -P_t \cdot i_d \quad \text{(A34)}$$

$$P_f = P_d \cdot (1 - \eta) \quad \text{(A35)}$$

$$P_{Rd} = F_{Nd} \cdot \omega_s \cdot t_d \cdot (1 + \frac{r_s}{r_d}) \quad \text{(A36)}$$

$$P_{Ri} = F_{Ni} \cdot \omega_s \cdot t_i \cdot (1 + \frac{r_s}{r_i}) \quad \text{(A37)}$$

Note that :

P_{ls} are power losses due to the tyre slippage.

P_f are the differential power losses.

P_{Rd} and P_{Ri} are the rolling resistance power losses due to the driver and idler tyres, respectively.

Figure A1 presents a graph of shell-tyre forces plotted against charge mass. Figure A2 represents the relationship between rotational speeds of tyres and shell, and the charge mass.

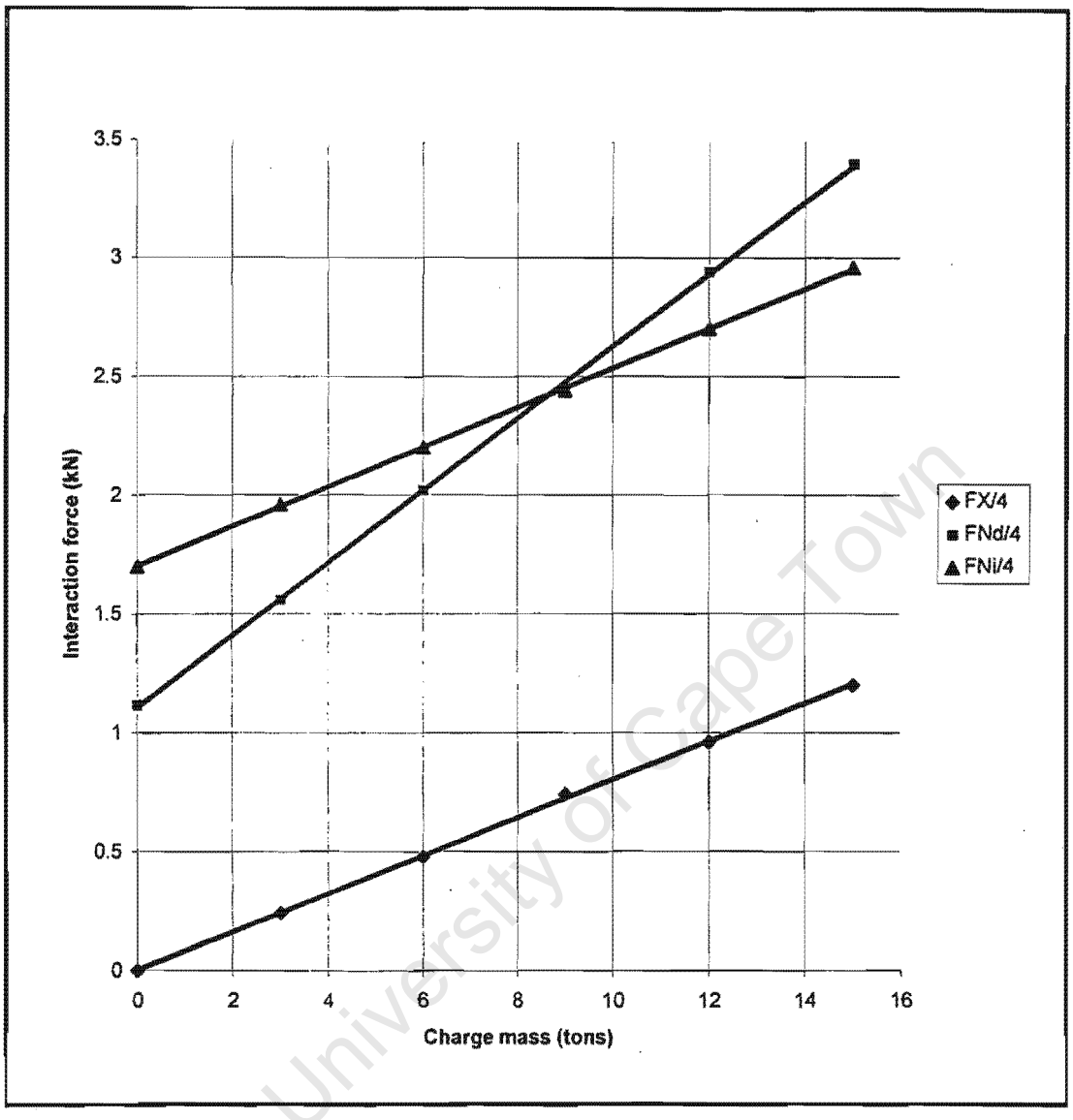

Figure A1. Shell-tyre interaction forces versus charge mass for the parametric study of the planar model.

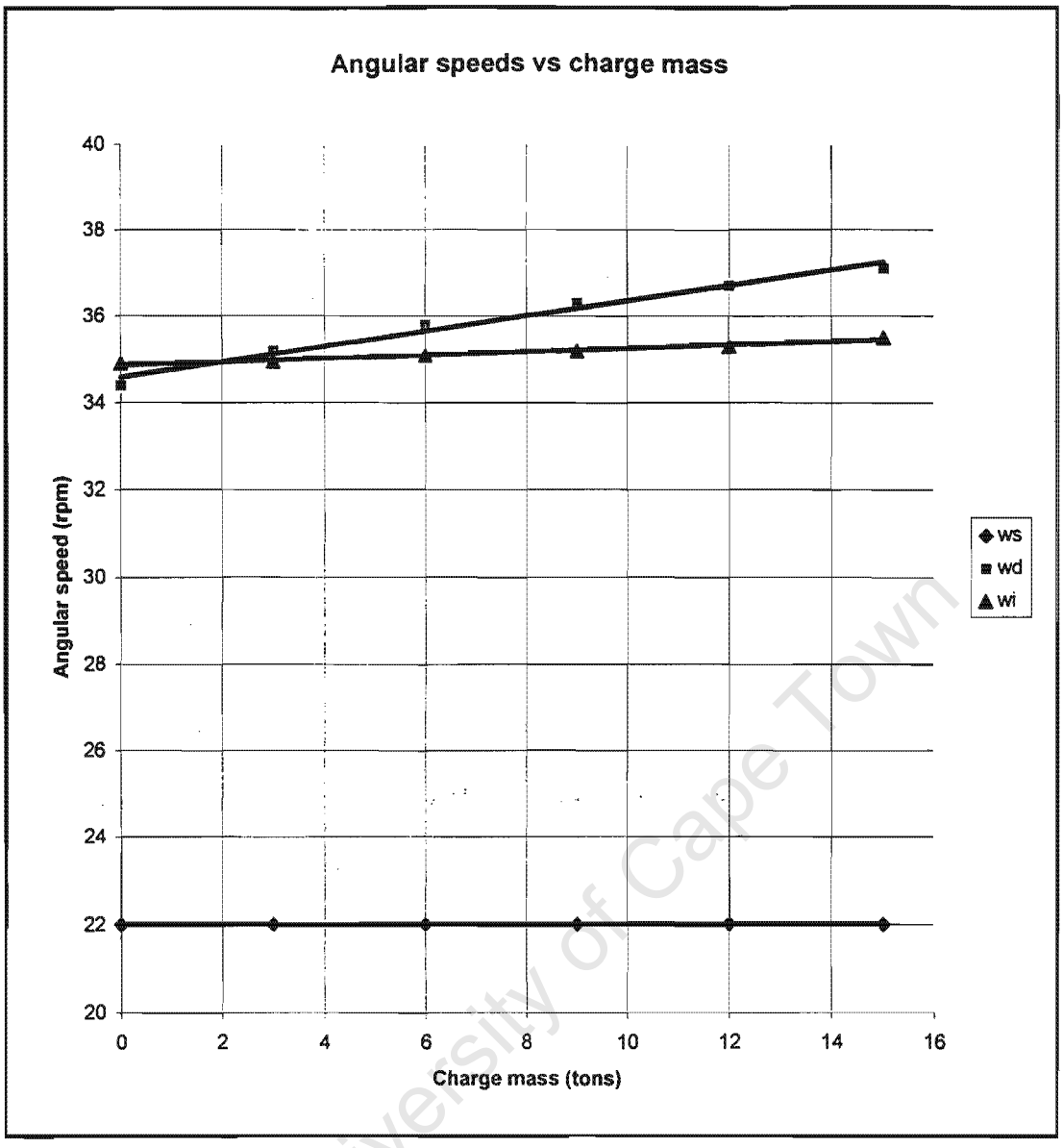

Figure A2. Rotational speeds of tyres and shell versus charge mass for the parametric study of the planar model.

APPENDIX B - A THEORETICAL SOLUTION FOR THE 3D MODEL [14]

In Appendix A the balance of the shell was considered by viewing it from the side and enforcing three conditions, i.e. the balance of the vertical forces, horizontal forces and torque. In the 3D study it is assumed that the left and right hand summed force components F_X, F_{Nd}, F_{Rd}, F_{Ni} *and* F_{Ri} closely correspond to their planar counterparts. Two additional balance conditions need to be satisfied. These are the pitching and yawing moment balances. These conditions demand a difference in the left and right hand tyre supporting force components.

• THE INFLUENCE OF THE DIFFERENTIAL GEARSET

The type of the differential gearset used has got a great influence on the mill operation. An open differential ensures an equal torque on both half-shafts, whilst a locked one ensures equal speeds on the half-shafts. These conditions are represented by the following equations :

$$\tau_{dl} = \tau_{dr} \leftarrow \text{Open differential} \qquad \text{(B1)}$$

or

$$r_{dl} \cdot F_{Xl} = r_{dr} \cdot F_{Xr} \qquad \text{(B2)}$$

$$\omega_{dl} = \omega_{dr} \leftarrow \text{Locked differential} \qquad \text{(B3)}$$

• DISTURBANCE OF LOADS DUE TO Y_c

Suppose the planar solution produces solutions for F_{Nd} and F_{Ni}, it is assumed that the corresponding solutions will be :

$$F_{Ndl,r} = \frac{F_{Nd}}{2} \pm \Delta F_{Nd} \tag{B4}$$

$$F_{Nil,r} = \frac{F_{Ni}}{2} \pm \Delta F_{Ni} \tag{B5}$$

where ΔF_{Nd} and ΔF_{Ni} are unknowns to be solved for.

Tyre radii are modelled as follows :

$$r_{dl,r} = r_{d0} - 2 \cdot F_{Ndl,r} \cdot k_{zd} \tag{B6}$$

$$r_{il,r} = r_{i0} - 2 \cdot F_{Nil,r} \cdot k_{zi} \tag{B7}$$

where k_{zd} and k_{zi} are the compressibilities of the four tyres on the driver and idler axles, respectively.

• PITCHING MOMENT BALANCE

Viewing the set-up from the rear, see Figures 4.1 and 4.3, the balance of moments acting on the shell gives,

$$
\begin{aligned}
&(F_{Ndl}\cdot\cos\phi_{dl}+(F_{Xl}-F_{Rdl})\cdot\sin\phi_{dl})\cdot\frac{T_d}{2}+\\
&(F_{Nil}\cdot\cos\phi_{il}+F_{Ril}\cdot\sin\phi_{il})\cdot\frac{T_i}{2}-\\
&(F_{Ndr}\cdot\cos\phi_{dr}+(F_{Xr}-F_{Rdr})\cdot\sin\phi_{dr})\cdot\frac{T_d}{2}-\\
&(F_{Nir}\cdot\cos\phi_{ir}+F_{Rir}\cdot\sin\phi_{ir})\cdot\frac{T_i}{2}=m_c\cdot g\cdot Y_c
\end{aligned}
\tag{B8}
$$

Substitute equations (A2) and (A3) from Appendix A together with equations (B 4) and (B5) into equation (B8) and rearrange to get :

$$Q\cdot\Delta F_{Nd}+R\cdot\Delta F_{Ni}=V \tag{B9}$$

where

$$Q=(\cos\phi_{dl}+\cos\phi_{dr}-f_r\cdot(\sin\phi_{dl}+\sin\phi_{dr}))\cdot\frac{T_d}{2} \tag{B10}$$

$$R=(\cos\phi_{il}+\cos\phi_{ir}+f_r\cdot(\sin\phi_{il}+\sin\phi_{ir}))\cdot\frac{T_i}{2} \tag{B11}$$

and

$$
\begin{aligned}
V\ =\ & m_c\cdot g\cdot Y_c+(F_{Xr}\cdot\sin\phi_{dr}-F_{Xl}\cdot\sin\phi_{dl})\cdot\frac{T_d}{2}-\\
& F_{Nd}\cdot T_d\cdot(\cos\phi_{dl}-\cos\phi_{dr}-f_r\cdot(\sin\phi_{dl}-\sin\phi_{dr}))\cdot\frac{1}{4}-\\
& F_{Ni}\cdot T_i\cdot(\cos\phi_{il}-\cos\phi_{ir}-f_r\cdot(\sin\phi_{il}-\sin\phi_{ir}))\cdot\frac{1}{4}
\end{aligned}
\tag{B12}
$$

- **YAWING MOMENT BALANCE**

Viewing the shell from the top, the balance of the yawing moments gives :

$$\begin{aligned}&((F_{Xl}-F_{Rdl})\cdot\cos\phi_{dl}-F_{Ndl}\cdot\sin\phi_{dl})\frac{T_d}{2}+\\&(F_{Nil}\cdot\sin\phi_{il}-F_{Ril}\cos\phi_{il})\cdot\frac{T_i}{2}-\\&((F_{Xr}-F_{Rdr})\cdot\cos\phi_{dr}-F_{Ndr}\cdot\sin\phi_{dr})\frac{T_d}{2}-\\&(F_{Nir}\cdot\sin\phi_{ir}-F_{Rir}\cos\phi_{ir})\cdot\frac{T_i}{2}=0\end{aligned} \tag{B13}$$

Again substitute equations (A2) and (A3) from Appendix A together with equations (B4) and (B5) into equation (B13) and rearrange to get :

$$S\cdot\Delta F_{Nd}+U\cdot\Delta F_{Ni}=W \tag{B14}$$

where

$$S=-(\sin\phi_{dl}+\sin\phi_{dr}+f_r\cdot(\cos\phi_{dl}+\cos\phi_{dr}))\cdot\frac{T_d}{2} \tag{B15}$$

$$U=(\sin\phi_{il}+\sin\phi_{ir}-f_r\cdot(\cos\phi_{il}+\cos\phi_{ir}))\cdot\frac{T_i}{2} \tag{B16}$$

and

$$\begin{aligned}W=&\frac{(F_{Xr}\cdot\cos\phi_{dr}-F_{Xl}\cdot\cos\phi_{dl})\cdot T_d}{2}-\\&\frac{F_{Nd}\cdot T_d\cdot(\sin\phi_{dr}-\sin\phi_{dl}+f_r\cdot(\cos\phi_{dr}-\cos\phi_{dl}))}{4}-\\&\frac{F_{Ni}\cdot T_i\cdot(\sin\phi_{ir}-\sin\phi_{il}-f_r\cdot(\cos\phi_{ir}-\cos\phi_{il}))}{4}\end{aligned} \tag{B17}$$

- **SOLUTION OF THE UNKNOWNS**

Equations (B9) and (B14) are two simultaneous equations in unknowns ΔF_{Nd} and ΔF_{Ni} which cannot be solved in a straight forward manner due to the dependence of the angles ϕ on the compressibility of the tyres, and due to the traction forces $F_{Xl,r}$ yet being unknown. The solution of these equations is through an iterative approach.

- **POWER DRAWN**

The drive shaft power, P_d :

$$P_d = (F_{Xl} \cdot r_{dl} + F_{Xr} \cdot r_{dr}) \cdot \omega_{da} + P_f \tag{B18}$$

where

$$\omega_{da} = \frac{\omega_{ds}}{N_f} \tag{B19}$$

$N_f > 1$

ω_{ds} is the angular speed of the drive shaft.

or

$$P_d = P_{tl} + P_{tr} + P_f \tag{B20}$$

where

$$P_{tl} = F_{Xl} \cdot r_{dl} \cdot \omega_{da} \tag{B21}$$

$$P_{tr} = F_{Xr} \cdot r_{dr} \cdot \omega_{da} \tag{B22}$$

and

$$P_f = (1-\eta)\cdot P_d \tag{B23}$$

The power transferred from the drive tyres to the shell, P_{ds}, is defined similarly to the planar model as follows:

$$\begin{aligned} P_{ds} = {} & F_{Xl}\cdot r_s\cdot\omega_s + F_{Xr}\cdot r_s\cdot\omega_s - F_{Ndl}\cdot t_{dl}\cdot(1+\frac{r_s}{r_{dl}}) - \\ & F_{Ndr}\cdot t_{dr}\cdot(1+\frac{r_s}{r_{dr}}) - F_{Nil}\cdot t_{il}\cdot(1+\frac{r_s}{r_{il}}) - F_{Nir}\cdot t_{ir}\cdot(1+\frac{r_s}{r_{ir}}) \end{aligned} \tag{B24}$$

The total power losses occurring on the whole system, P_{lds}, are obtained from :

$$P_{lds} = P_d - P_{ds} \tag{B25}$$

$$\begin{aligned} \Rightarrow P_{lds} = {} & F_{Xl}\cdot r_{dl}\cdot\omega_{da}\cdot(1-\frac{r_s\cdot\omega_s}{r_{dl}\cdot\omega_{da}}) + F_{Xr}\cdot r_{dr}\cdot\omega_{dr}\cdot(1-\frac{r_s\cdot\omega_s}{r_{dr}\cdot\omega_{da}}) + \\ & F_{Ndl}\cdot t_{dl}\cdot\omega_s\cdot(1+\frac{r_s}{r_{dl}}) + F_{Ndr}\cdot t_{dr}\cdot\omega_s\cdot(1+\frac{r_s}{r_{dr}}) + F_{Nil}\cdot t_{il}\cdot\omega_s\cdot(1+\frac{r_s}{r_{il}}) + \\ & F_{Nir}\cdot t_{ir}\cdot\omega_s\cdot(1+\frac{r_s}{r_{ir}}) \end{aligned} \tag{B26}$$

The longitudinal slip is defined as follows :

$$i_{dal,r} = \frac{r_s\cdot\omega_s}{r_{dl,r}\cdot\omega_{da}} - 1 \tag{B27}$$

$$P_{lds} = -P_{tl}\cdot i_{dal} - P_{tr}\cdot i_{dar} + P_d\cdot(1-\eta) + P_{Rdl} + P_{Rdr} + P_{Ril} + P_{Rir} \tag{B28}$$

or

$$P_{lds} = P_{lsl} + P_{lsr} + P_f + P_{Rd} + P_{Ri} \tag{B29}$$

where

$$P_{lsl} = -P_{tl} \cdot i_{dal} \tag{B30}$$

$$P_{lsr} = -P_{tr} \cdot i_{dar} \tag{B31}$$

$$P_f = (1-\eta) \cdot P_d \tag{B32}$$

$$P_{Rdl} = F_{Ndl} \cdot t_{dl} \cdot \omega_s \cdot (1+\frac{r_s}{r_{dl}}) \tag{B33}$$

$$P_{Rdr} = F_{Ndr} \cdot t_{dr} \cdot \omega_s \cdot (1+\frac{r_s}{r_{dr}}) \tag{B34}$$

$$P_{Ril} = F_{Nil} \cdot t_{il} \cdot \omega_s \cdot (1+\frac{r_s}{r_{il}}) \tag{B35}$$

$$P_{Rir} = F_{Nir} \cdot t_{ir} \cdot \omega_s \cdot (1+\frac{r_s}{r_{ir}}) \tag{B36}$$

APPENDIX C - FIGURES FROM THE PREVIOUS STUDIES CARRIED OUT ON THE TYRE-MOUNTED MILL

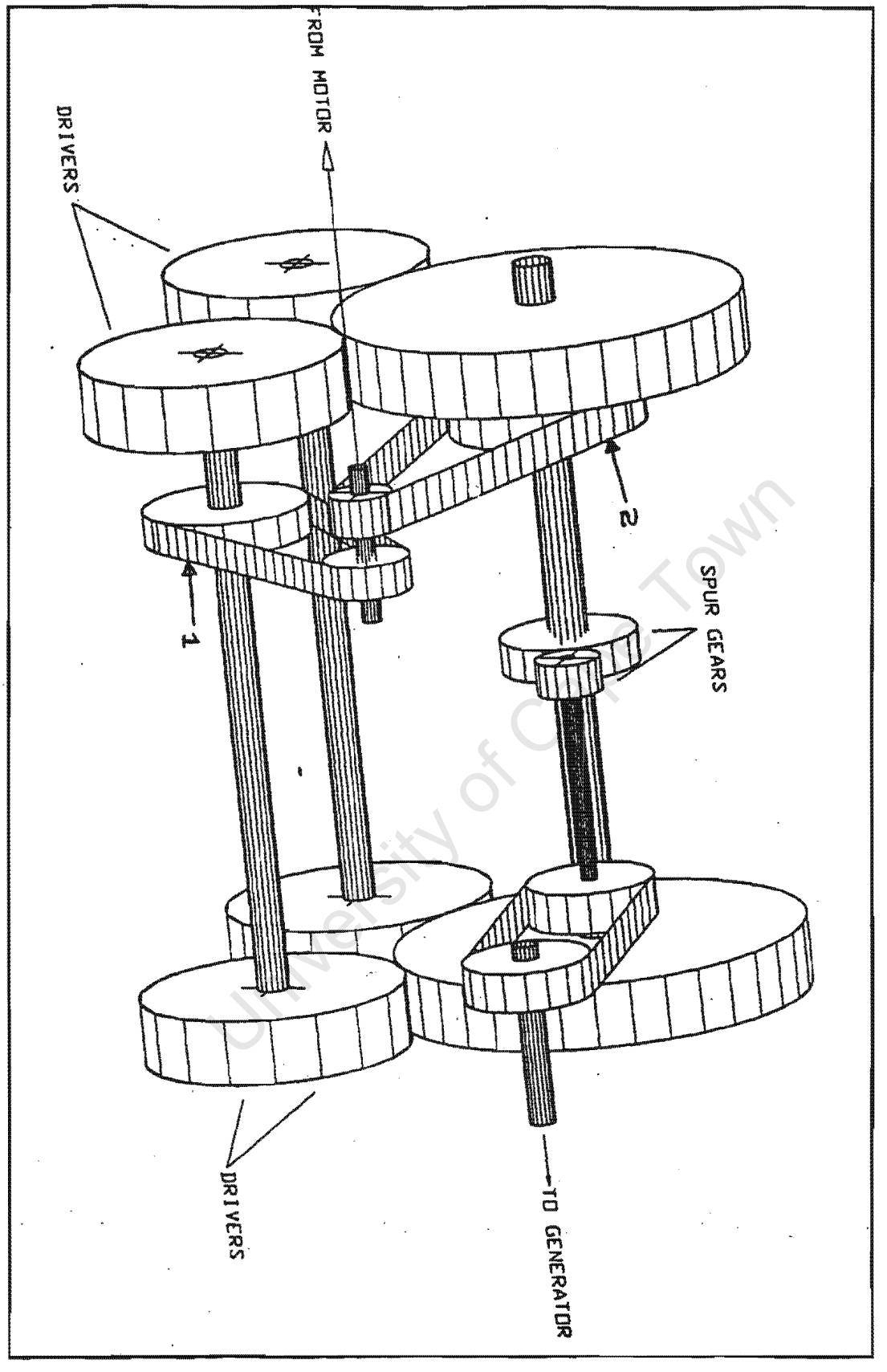

Figure C1. Schematic diagram of a model mill designed in 1995.

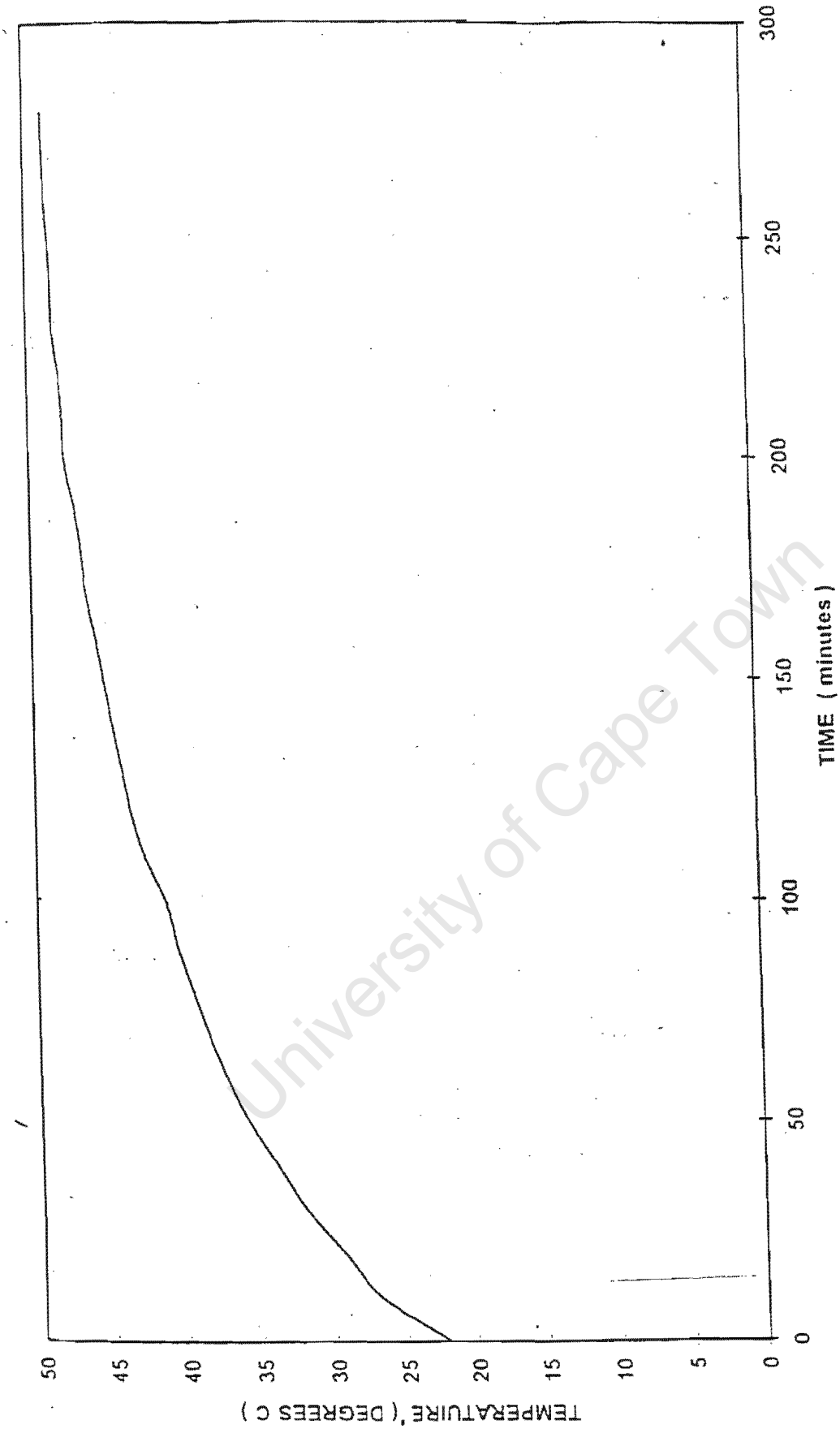

Figure C2. Experimental results for test 2 on the model differential gearset.

APPENDIX D - MORE PICTURES OF THE EXPERIMENTAL MODEL MILL.

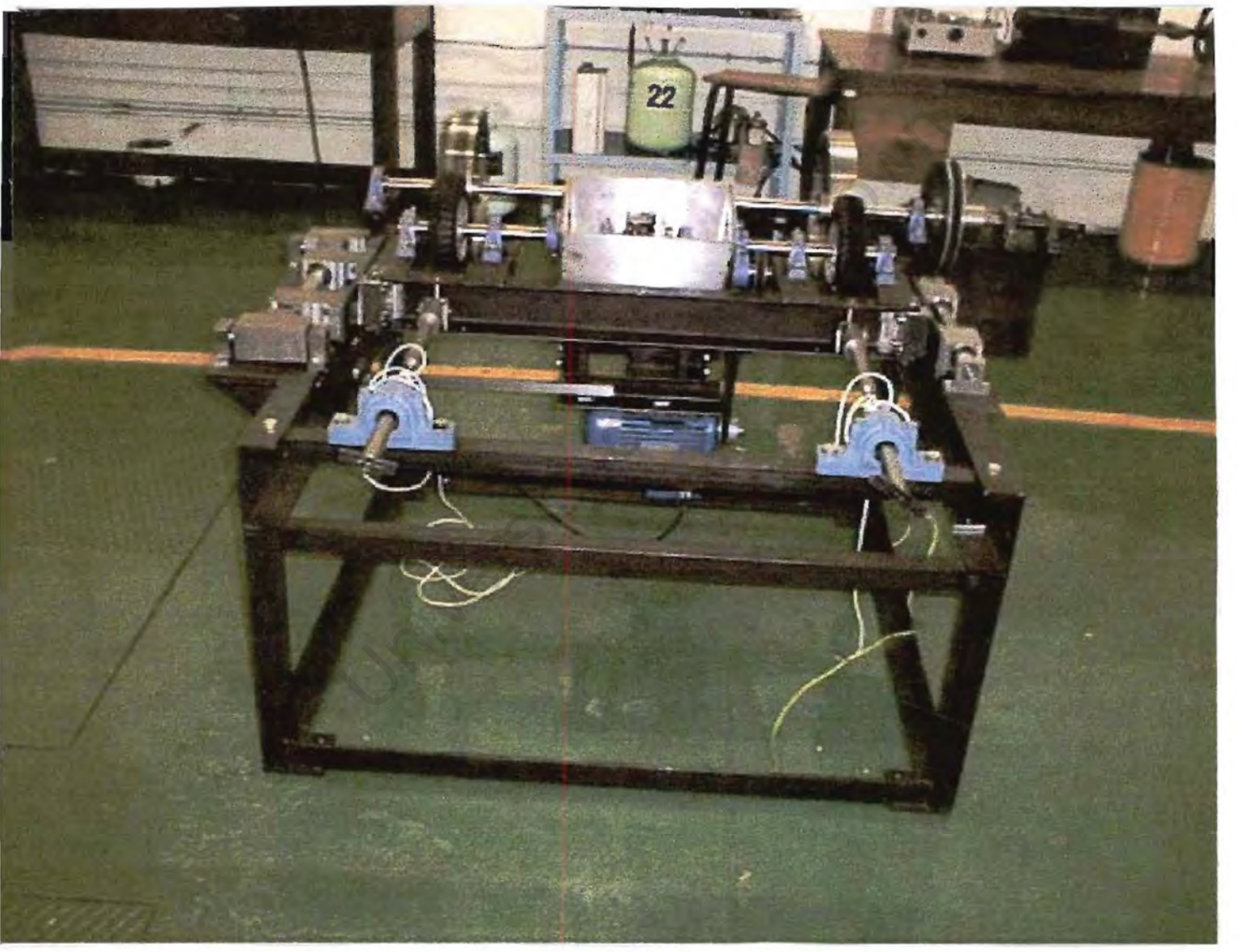

Figure D1. Front view of the experimental model mill.

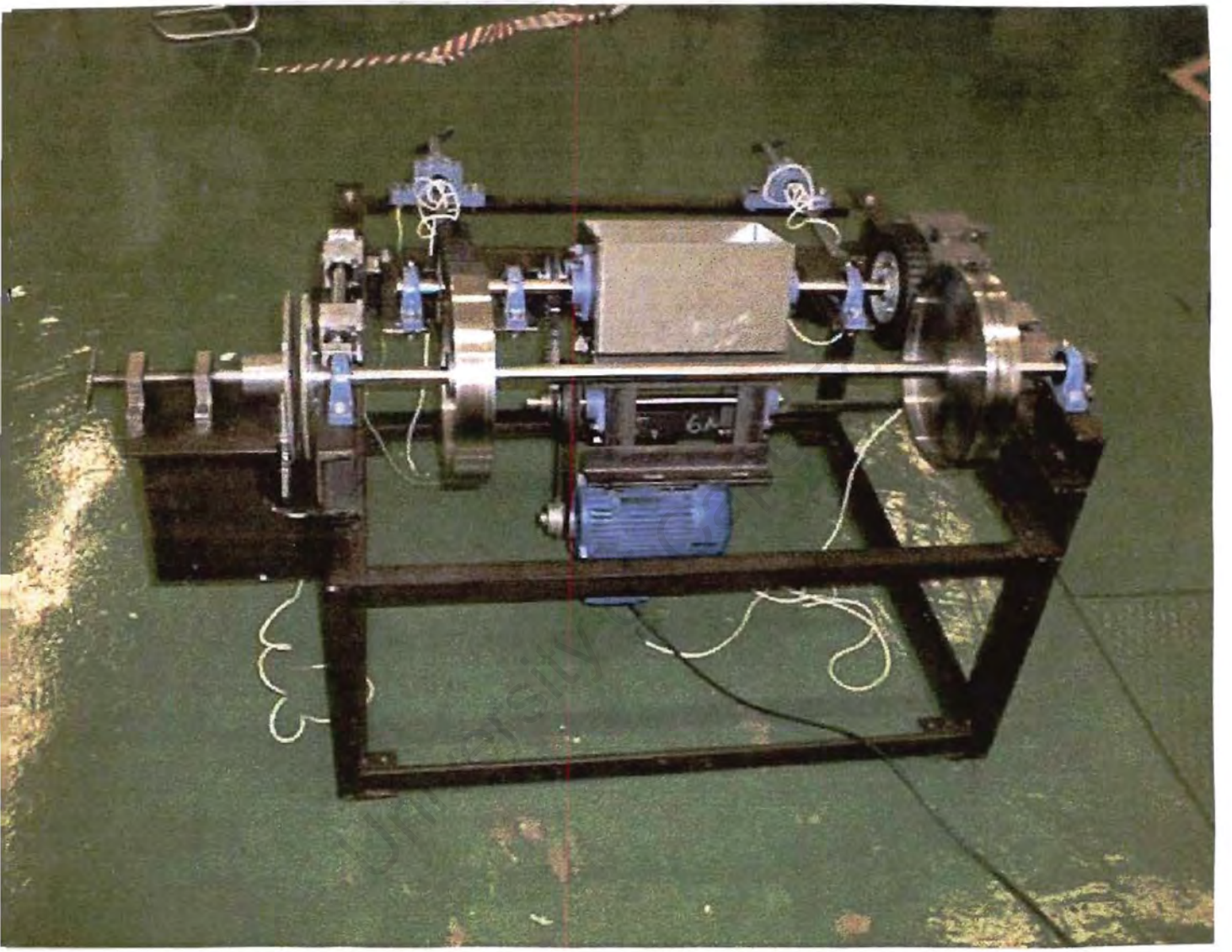

Figure D2. Back view of the experimental model mill.

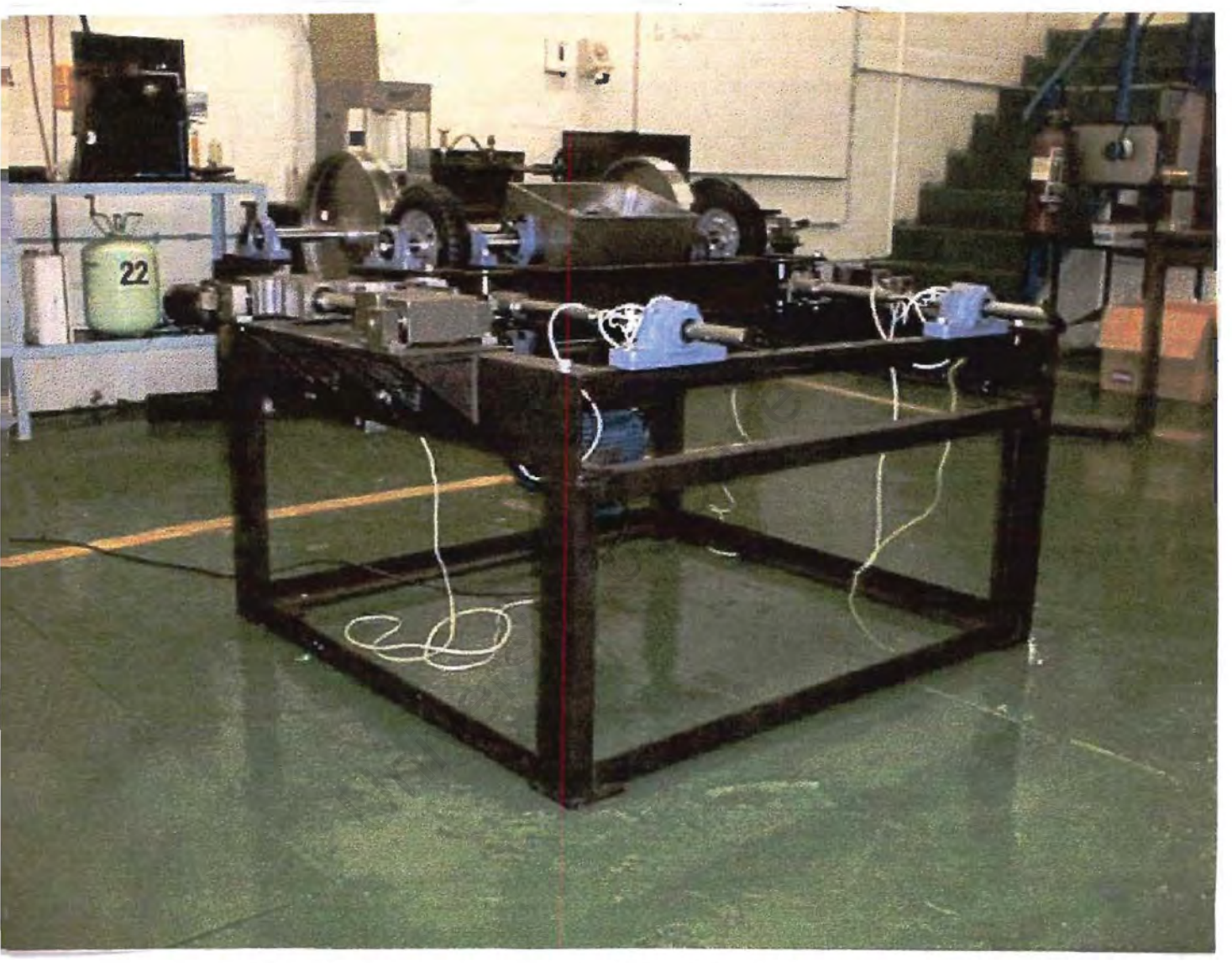

Figure D3. Front oblique view of the experimental model mill.

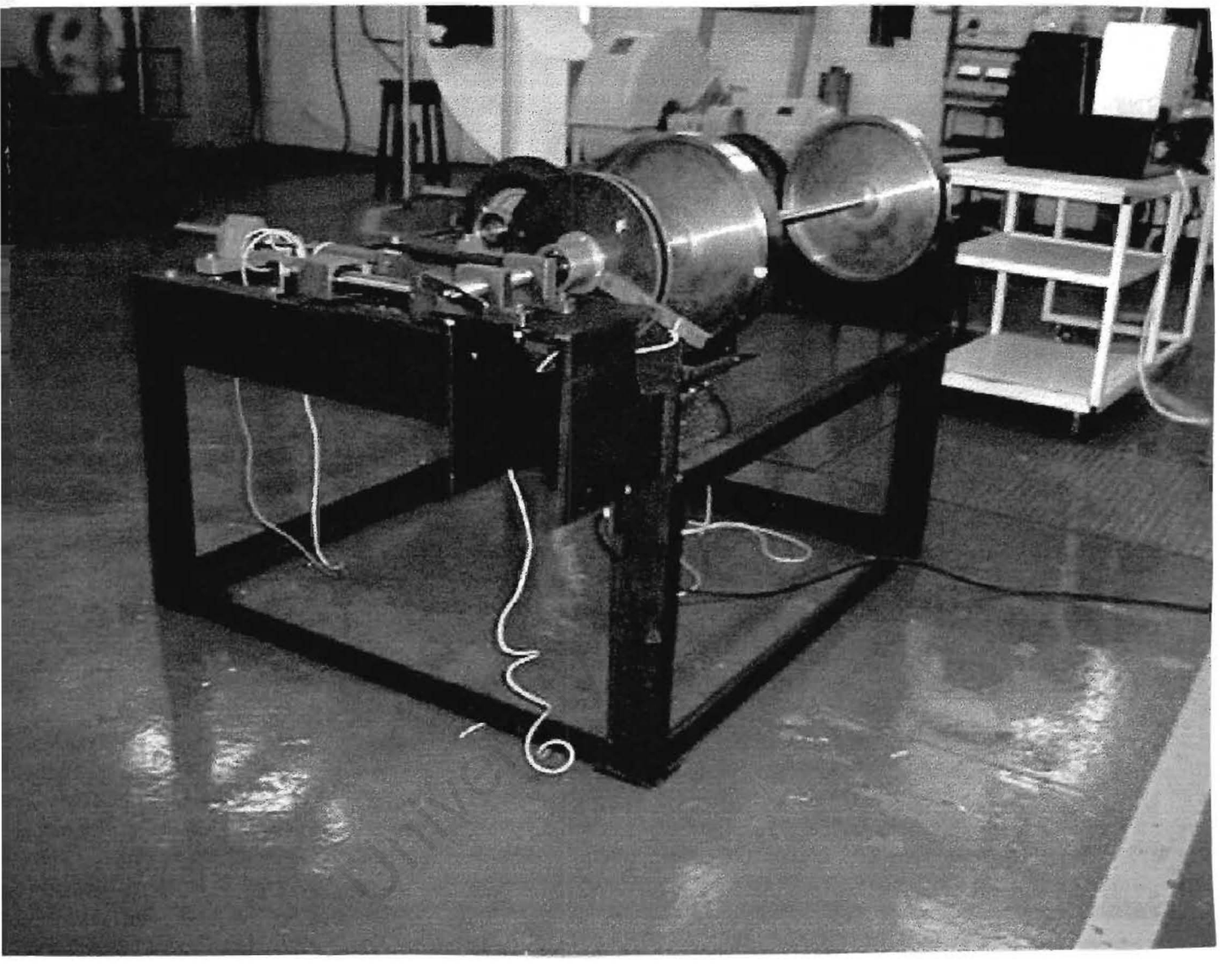

Figure D4. Back oblique view of the experimental model mill.

APPENDIX E - EXPERIMENTAL PLANAR MODEL MILL RESULTS

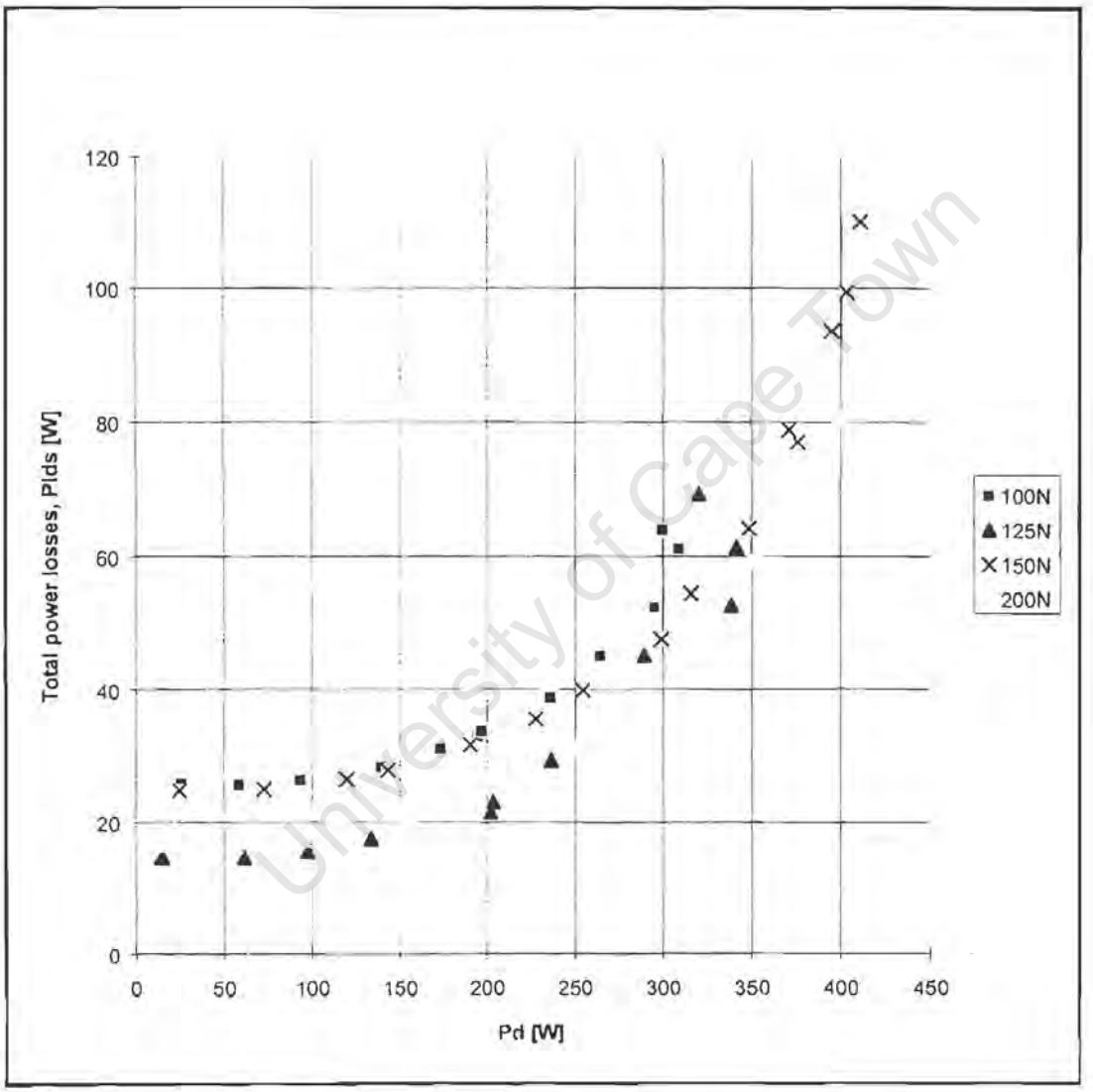

Figure E1. Total power losses versus motor input power for P2.

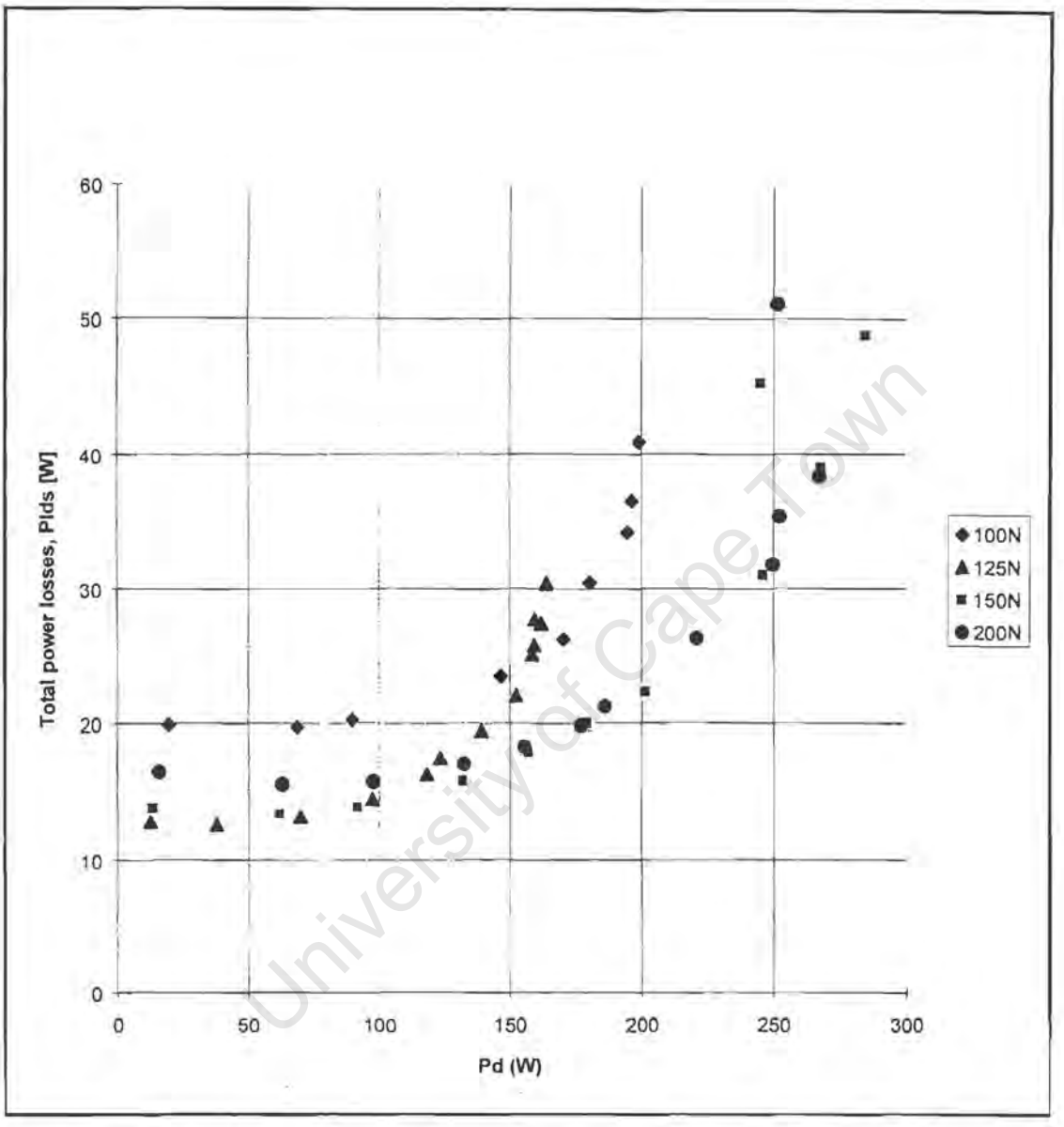

Figure E2. Total power losses versus motor input power for S1.

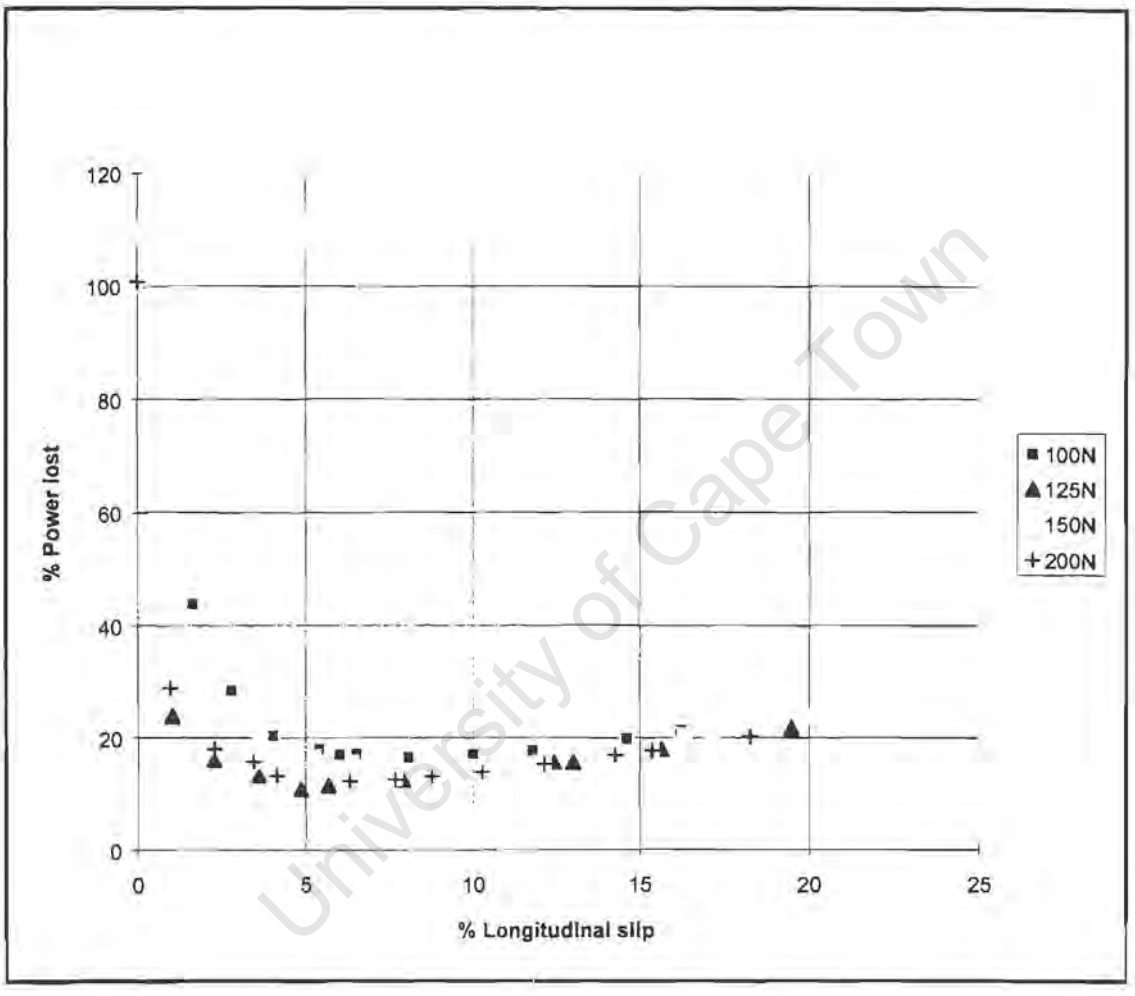

Figure E3. Mill in-efficiency versus longitudinal slip for P2.

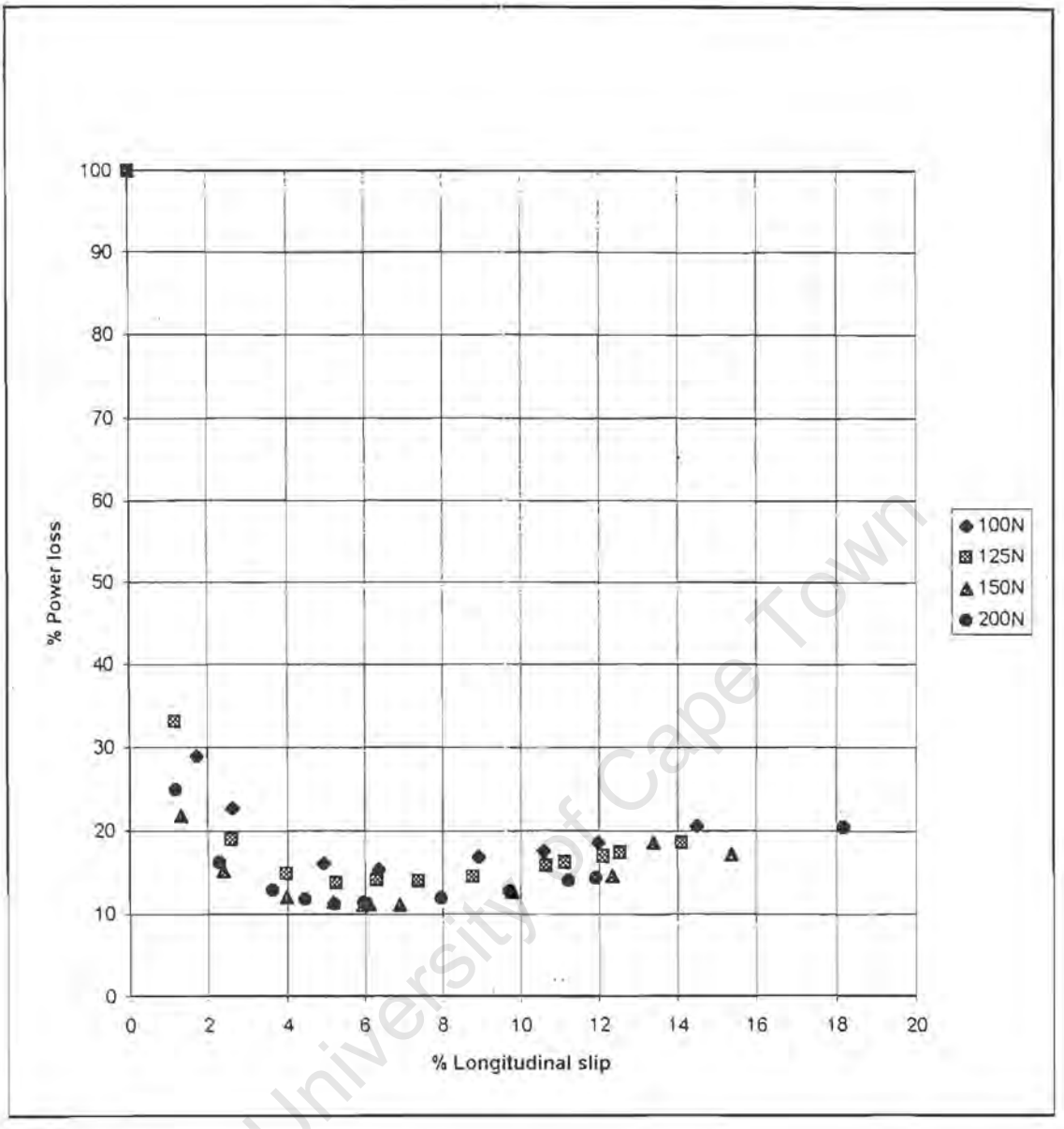

Figure E4. Mill in-efficiency versus longitudinal slip for S1.